Gap Phenomena in Graphite and its MC_6 Intercalation Compounds

Nicholas Edward Shuttleworth

A Thesis presented for the degree of

Doctor of Philosophy

I, Nicholas Edward Shuttleworth, confirm that the work presented in this thesis is my own. Wherever information has been derived from other sources this has been indicated in the text.

Abstract

The physical and electronic structure of graphite lend it a huge amount of functional flexibility. Through charge doping of its layers by intercalation or dimensional constriction diverse electronic phenomena can be observed. This thesis constitutes the study of two aspects of the excitations of graphite in two extremes: electron-phonon coupling in the strongly doped bulk and electronic transport in the semi-metallic sub-micron regime. Measurements of the heat capacity of the graphite intercalation compounds CaC_6, SrC_6 and BaC_6 have been performed between $300\,K$ and $390\,mK$. The onset anomoly of a charge density wave state recently detected in CaC_6 at $78\,K$ has not been observed signifying a transition temperature above $300\,K$. The superconducting phase of CaC_6 has been characterised as BCS-like with intermediate coupling and mild gap anisotropy, while the inaccuracy of predictions of the superconducting heat capacity anomoly has been suggested as due to Fermi surface competition with the charge density wave state. The electron-phonon coupling strength has been found to be in agreement with predictions for CaC_6 and SrC_6, while for BaC_6 it is measured as half the predicited value, explaining the failure of previous experiments to observe superconductivity at the predicted $T_C \sim 230\,mK$. Micron-sized graphitic devices created by focused ion beam micro-machining have been found to exhibit ballistic transport behaviour up to $\sim 250\,K$. Below $40\,K$ a Coulomb-like pseudogap has been observed in agreement with previous devices, suggested as due to electron-electron interactions within the device. Below $10\,K$ further complex conductance features have been observed with unknown cause.

Acknowledgements

A thesis is a labour of love. Sometimes. Other times it's a silent terror praying on the unprepared. The support of colleagues and friends makes the former times a joy and the latter times shorter.

This particular thesis would not have been possible without the advice, expertise, help and humour of a great number of people:

My supervisor Mark Ellerby deserves the prime position in this list for having the faith to take me on as a PhD student and for teaching, supporting, encouraging, enthusing, persuading, cajoling and shoving me over the years. Thanks are also due to Neal Skipper for his level-headed guidance and awful jokes.

Next come those who helped in the prep and measuring of the samples: Andrew Walters for his kish graphite obtaining skills, Suguo Huo in the LCN cleanroom and Chris Howard, master of all he intercalates; Sajid Saleem, Wuxia Li, Kevin Lee and Takashi Matsuura for their FIB tuition and skills; Sian Fogden at Imperial and Martin Lees and his guys at Warwick.

Those that helped with the write-up: Adam and Chris Rahnejat's flat, Caroline Friend's spare bed, Kate Armstrong's spare flat and Al McKelvie's sofa; my parents, who have been unconditionally supportive and impressively patient throughout my lodging and who can now look forward to a damned good read (and a little peace and quiet).

Last but in no way least: the occupants of the Flob for some crosswording genius, adventurous karaoke, skilled googling and pretty niche humour - James Chivall, Chris Rahnejat and Ross Springell - and the occupants of F10a for its rarefied intellectual atmosphere - Emily Milner, Jacqueline Edge and Jon Payne.

Contents

1 Introduction **23**

1.1 Graphitic Systems 23

1.2 Aims, objectives and motivation 24

1.3 Form of the Dissertation 25

2 Materials **27**

2.1 Graphite 27

2.1.1 Structural Properties 27

2.1.2 Vibrational Properties 32

2.1.3 Electronic Properties 35

2.2 MC_6 Graphite Intercalation Compounds 38

2.2.1 Structural Properties 38

2.2.2 Vibrational Properties 39

2.2.3 Electronic Properties 43

3 Superconductivity and Charge Density Waves in MC_6 Graphite Intercalation Compounds **45**

3.1 Abstract 45

3.2 Theory and Phenomena 47

3.2.1 Heat Capacity 47

3.2.2 Superconductivity 48
3.2.3 Charge Density Waves 53
3.2.4 Competition between Superconductivity and CDWs 60
3.3 Introduction and Experimental Motivation 62
3.3.1 Superconductivity in GICs - The Study of CaC_6 62
3.3.2 Prediction of Superconductivity in BaC_6 66
3.3.3 Evidence of a Charge Density Wave in CaC_6 69
3.4 Experimental Details 71
3.4.1 Sample Creation by Intercalation 71
3.4.2 Heat Capacity Measurement Setup 74
3.5 Results 76
3.5.1 CaC_6 - Heat Capacity Measurements 76
3.5.2 SrC_6 - Heat Capacity Measurements 79
3.5.3 BaC_6 - Heat Capacity Measurements 79
3.6 Discussion 80
3.6.1 Low Temperature Heat Capacity of MC_6 GICs 80
3.6.2 Very Low Temperature Effects in SrC_6 and BaC_6 86
3.6.3 Charge Density Wave Detection in CaC_6 90
3.6.4 The Nature of Superconductivity in CaC_6 94
3.7 Summary 100

4 Ballistic Transport and Pseudogap State in FIB-Milled Kish Graphite Micro-Structures 101

4.1 Abstract 101
4.2 Theory and Phenomena 102
4.2.1 Drude Model of Electrical Conduction 102
4.2.2 Ballistic Transport 104
4.2.3 Coulomb Interactions 105

4.3 Introduction and Experimental Motivation . . . 107
4.3.1 Electrical Resistance in Graphites . . . 107
4.3.2 Micron-Sized Stack Devices . . . 114
4.4 Experimental Details . . . 119
4.4.1 Graphite Precursor . . . 119
4.4.2 Macroscopic Preparation . . . 120
4.4.3 Focused Ion Beam Milling . . . 123
4.4.4 Device Details . . . 128
4.4.4.1 Stack Device A . . . 128
4.4.4.2 Stack Device B . . . 128
4.4.4.3 Other Devices . . . 129
4.4.5 Electrical Measurement Setup . . . 131
4.5 Results . . . 132
4.5.1 Stack Device A . . . 132
4.5.2 Stack Device B . . . 134
4.6 Discussion . . . 136
4.6.1 Size Effects in Graphitic Stack Devices . . . 136
4.6.2 Pseudogaps in Graphitic Stack Devices . . . 140
4.6.3 Measuring c-axis Conduction . . . 146
4.7 Summary . . . 147

5 Summary and Next steps **149**

Bibliography **151**

List of Figures

2.1 Crystalline structure of hexagonal graphite. The dimensions of the unit cell, represented by dotted-dashed lines, are $a_0 = 2.456\,\mathring{A}$ and $c_0 = 6.708\,\mathring{A}$. $a_{NN} = 1.42\,\mathring{A}$ is the distance between nearest neighbours. In the c-direction the graphene sheets are registered in an AB stacking order and are separated by $d_c = 3.35\,\mathring{A}$. Figure adapted from [1]. 28

2.2 Brillouin zone of graphite, showing several high-symmetry points and a schematic version of the graphite electron and hole Fermi surfaces located along the $H - K$ axes. Symmetric points are labelled with Bouckaert-Smoluchowski-Wigner notation ($\Gamma AHKLM$). The direction $\Gamma - A$ is perpendicular to the graphene sheets; $\Gamma - K$ is parallel to the graphene sheets. Figure taken from [2]. 28

2.3 Rocking curve of [002] x-ray diffraction peak (theta-theta scan). Left: $300\,\mu m$ thick kish graphite (KG) flake and $500\,\mu m$ thick HOPG sample. Right: A different kish graphite sample at $300\,\mu m$ thick and cleaved to $40\,\mu m$ thick. Figure adapted from [3]. 29

2.4 Upper: ECCI image of a kish graphite surface. The lack of contrast indicates that the crystallite size is greater than the field of vision of the image. Lower: ECCI image of an HOPG surface showing the typical extent of the in-plane crystallites as $\sim 60\,\mu m$. This sample has a mosaic spread of 0.9^o. Figure adapted from [3]. 30

2.5 TEM image of an HOPG sample (mosaic spread 0.4^o) taken parallel to the graphene layers. The c-axis is perpendicular to the clearly observable stripes of different grey colours, each representing a crystalline region with a different orientation. Typical c-axis crystallite sizes are $60 \pm 20\,nm$. Figure adapted from [4]. 31

2.6 Schematic diagram of the layer lattice dynamics of graphite. The lattice dynamics are characterised by high-frequency intralayer modes and low frequency interlayer modes, the latter separated into layer breathing, layer shear and bending modes. The intralayer modes occur at energies above $\sim 125\,meV$, while the interlayer modes occur at lower energies as shown in figure 2.7. Figure adapted from [5]. 34

2.7 Phonon dispersion of graphite from inelastic x-ray scattering (symbols). Solid lines are force-constant calculations for graphene. The dashed line is a quadratic extrapolation of the data. The phonon branches are specified as following: out-of-plane acoustic (ZA), transverse acoustic (TA), longitudinal acoustic (LA), out-of-plane optical (ZO), transverse optical (TO) and longitudinal optical (LO). The vertical lines are denoted by their symmetry representation. Figure adapted from [6]. 34

2.8 Left: Band structure of graphene. The $\pi-$band is completely filled in the ground state and touches the empty π^*-band at the K point where both bands have conical shape. Right: Zoom-in of the energy bands close to one of the Dirac points. Figure taken from [7]. 36

2.9 The electronic structures shown schematically of (left) graphene and (right) graphite, where $g(E)$ is the DOS as a function of energy and E_F is the Fermi energy. 36

2.10 Density functional theory (DFT), local density approximation (LDA) calculated electronic band structure of graphite along high-symmetry directions in the Brillouin zone. Band types are colour-coded as: π orange; σ green; interlayer blue. $\pi-$ and $\sigma-$bands are below the Fermi level, π^{*-} and σ^*-bands are above the Fermi level. Figure adapted from [8]. 37

2.11 Layered structure of stage-1 CaC_6 displaying $A\alpha A\beta A\gamma$ stacking order. . 39

2.12 Layered structure of stage-1 SrC_6/BaC_6 displaying $A\alpha A\beta$ stacking order. 40

2.13 Left: The hexagonal Brillouin zone. The direction $\Gamma - A$ is perpendicular to the graphene sheets; $\Gamma - K$ is parallel to the graphene sheets. Right: The rhombohedral Brillouin zone, in which the hexagonal K-point is refolded at Γ. The direction $\Gamma - L$ is perpendicular to the graphene sheets; $\Gamma - \chi - X$ is parallel to the graphene sheets. Figure taken from [9]. . . . 41

2.14 DFT calculated phonon dispersion of $\mathrm{CaC_6}$. The amount of Ca vibration is represented by the size of ●, of C_z by the size of ○, and of C_{xy} by the size of ◊. Figure taken from [10]. 41

2.15 Phonon dispersion of $\mathrm{CaC_6}$ (left) and $\mathrm{BaC_6}$ (right) (00l) measured using inelastic x-ray scattering at $5\,K$ (squares), $50\,K$ (triangles) and $300\,K$ (circles). Empty symbols denote M_z phonon intensity, full symbols label M_{xy} phonon intensity. The theoretical dispersion of the M_z and M_{xy} phonons are plotted with solid lines and dashed lines respectively. A guide to the eye is plotted showing the dispersion of the experimental M_z phonons at $300\,K$ (thick solid line). The symmetry point L ($\mathrm{CaC_6}$) is located at $q = 0.694\,A^{-1}$. The symmetry point A ($\mathrm{BaC_6}$) is located at $q = 0.299\,A^{-1}$. The crosses mark the phonon energies calculated at Γ using the experimental lattice parameters and space group of $\mathrm{BaC_6}$. Figures taken from [9]. 42

2.16 The electronic structures shown schematically of (left) donor-GICs and (right) acceptor GICs, where $g(E)$ is the DOS as a function of energy E and E_F is the Fermi energy. Filled states are shown in grey, empty states in white. 43

2.17 DFT calculated electronic band structures of $\mathrm{CaC_6}$, $\mathrm{SrC_6}$ and $\mathrm{BaC_6}$. The zero energy corresponds to the Fermi energy E_F. Bands are colour-coded as: graphite-π orange; interlayer-intercalate (free-electron-like) blue. Figure adapted from [11]. 44

3.1 Left: Comparison of flux penetration behaviour of type I and type II superconductors. H_C is the critical field for a type I superconductor. H_{C1} and H_{C2} are the lower and upper critical fields for a type II superconductor. Right: Temperature dependence of the critical field H_C. Figures taken from [12]. 50

3.2 An isotropically gapped Fermi surface in a BCS superconductor at $T = 0$. The shaded region represents the occupied states of the superconducting electrons. 50

3.3 Temperature dependence of the energy gap in the BCS theory. Strictly speaking, the curve holds only in a weak-coupling limit, but it is a good approximation in most cases. Figure taken from [12]. 51

3.4 Heat capacity of a material at and below the BCS superconducting transition showing the discontinuous jump in heat capacity at T_C. Figure from [12]. 53

3.5 Peierls distortion in a 1D metal with a half-filled band: (left) undistorted metal; (right) Peierls insulator. $d(r)$ is the electronic density; a is the lattice constant. Figure taken from [13]. 54

3.6 Heat capacity of 2H-$NbSe_2$ showing the CDW transition at $T_{CDW} = 33\,K$. The superconducting transition is seen at $7\,K$. Figure adapted from [14]. 58

3.7 Heat capacity of 2H-TaS_2 showing the CDW transition at $T_{CDW} = 78\,K$. Figure adapted from [14]. 58

3.8 Heat capacity of 2H-$TaSe_2$ showing the CDW transitions at $T_{CDW} = 121\,K$ and $90\,K$ for the ICDW and CCDWs, respectively. Figure adapted from [14]. 59

3.9 Temperature dependence of the heat capacity of $K_{0.3}MoO_3$ (blue bronze). The CDW transition is clear at $T_{CDW} = 180\,K$. The solid line is a polynomial fit through the background of the heat capacity data. Figure adapted from [15]. 59

3.10 Temperature dependences of the superconducting (Δ_{SC}) and CDW (Δ_{CDW}) order parameters for different values of the parameter μ, the portion of the Fermi surface where the CDW gap develops. Figure taken from [16]. . 61

3.11 Temperature dependence of $\frac{\Delta C_P}{T} = \frac{C_P(H=0)}{T} - \frac{C_P(H=10\,kOe)}{T}$ for CaC_6. The red solid line is the best fit according to a scaled isotropic s-wave BCS model. Inset: $H_{C2}(T)$ for $H \parallel c$ estimated from heat capacity (filled squares) and susceptibility (open circles) measurements. The blue dashed line demonstrates the WHH prediction and the red solid line is a linear fit for the low magnetic field data ($H < 1\,kOe$). Figure adapted from [17]. 64

3.12 Deviation of the calculated (Boeri [18]) strong-coupling heat capacity from experimental results (Kim [17]) for CaC_6. Figure taken from [19]. 65

3.13 Left: Comparison of the reduced heat capacity of CaC_6 as measured by Kim [17] to isotropic and moderately anisotropic gap models. Right: Experimental normalized conductance [20] compared to isotropic and anisotropic gap predictions. Figure adapted from [21]. 66

3.14 Temperature dependence of $\frac{\Delta C_P}{T} = \frac{C_P(H=0)}{T} - \frac{C_P(H=500\,Oe)}{T}$ for SrC_6. The red solid line is the best fit according to a scaled isotropic s-wave BCS model. The blue dashed line represents the BCS curve. Figure taken from [22]. 67

3.15 T_C as a function of interlayer spacing for CaC_6, YbC_6, SrC_6, BaC_6, KC_8, RbC_8 and CsC_8. For CaC_6 T_C at a pressure of $8\,GPa$ is also plotted in grey. An upper limit for BaC_6 of $T_C = 0.3\,K$ is labelled with an arrow [22], although this upper limit has been subsequently superseded (now $0.06\,K$ [23]). Figure taken from [22]. 68

3.16 Field-cooled magnetisation M as a function of temperature at constant applied magnetic fields indicated in the legend. No superconducting transition is seen at any field. Figure taken from [24]. 69

3.17 Left: Constant current STM image of a CaC_6 surface recorded at $78\,K$, $+400\,mV$ showing atomic resolution with a superimposed one-dimensional, $1.125\,nm$ period stripe. Right: Conductance spectroscopy showing the CDW gap with $2\Delta_{CDW} \approx 475\,meV$. Figures provided by K.C. Rahnejat, University College London [25]. 70

3.18 2Θ x-ray diffraction patterns for samples of CaC_6, and SrC_6 and BaC_6 from the same batches as those tested below. Sample purities as detailed in table 3.4 calculated by ratios of peak heights taking local backgrounds. SrC_6 background variation is due to small sample size and Kapton tape used to secure the sample in the diffractometer. 73

3.19 Schematic representation of the sample environment in the Quantum Design PPMS. Figures taken from the PPMS documentation supplied by Quantum Design. 74

3.20 Heat capacity as a function of temperature for CaC_6 from $300\,K$ to $2\,K$ at zero magnetic field. Error bars are smaller than datapoints at all temperatures. Inset: The superconducting transition onset is at $11.5\,K$. . . . 77

3.21 Heat capacity of CaC_6 as a function of temperature between $12.5\,K$ and $2\,K$ showing the superconducting transition in zero magnetic field and its suppression in applied fields up to $10\,kOe$. Error bars are smaller than datapoints at all temperatures. 77

3.22 Heat capacity as a function of temperature for SrC_6 between $75\,K$ and $2\,K$ in zero magnetic field. 78

3.23 Heat capacity as a function of temperature for SrC_6 from $10\,K$ to $0.386\,K$ in zero magnetic field. 78

3.24 Heat capacity as a function of temperature for BaC_6 from $150\,K$ to $2\,K$ in zero magnetic field. 79

3.25 Heat capacity as a function of temperature for BaC_6 from $10\,K$ to $0.386\,K$ in zero magnetic field. 80

3.26 Low temperature heat capacities of CaC_6, SrC_6 and BaC_6 as a function of temperature. The red lines are fits to the function described by equation 3.19 with parameters given in table 3.5. 81

3.27 Debye temperature Θ_D as a function of molecular mass for (red) CaC_6, SrC_6 and BaC_6 (left to right) as measured here. Red error bars are experimental uncertainty. Other points (black) are average values from other studies as detailed in table 3.6. Black error bars demonstrate the upper and lower limits of previously measured values. 84

3.28 Very low temperature measurements of the heat capacity of SrC_6 plotted as $\frac{C}{T}$ as a function of T^2 showing a Schottky-like anomaly below $6\,K^2$. The red line is a fit to equation 3.21 with parameters given in table 3.9. . . 87

3.29 Very low temperature measurements of the heat capacity of BaC_6 plotted as $\frac{C}{T}$ as a function of T^2 showing a Schottky-like anomaly below $10\,K^2$. The red line is a fit to equation 3.21 with parameters given in table 3.9. . . 87

3.30 Heat capacity of an Airco-Speer chlorine-purified polycrystalline graphite (AS) neutron irradiated to various doses. Figure taken from [26] 89

3.31 Heat capacity of CaC_6 as a function of temperature (black points) from $300\,K$ to $2\,K$ at zero magnetic field. Red line is a polynomial fit to the data between $50\,K$ and $180\,K$ extrapolated to $300\,K$ for comparison with data. 92

3.32 ΔC as a function of temperature from $78\,K$ to $300\,K$ for CaC_6 in zero magnetic field (black points), in a field of $10\,kOe$ (red points) and $0.25\,mg$ of Apiezon N grease in zero magnetic field (blue points). Apiezon N data taken from [27]. All curves obtained by subtracting an extrapolated polynomial fitted between $50\,K$ and $180\,K$. 93

3.33 $\frac{\Delta C}{T}$ as a function of temperature for CaC_6 (blue points) showing the superconducting anomaly with $T_C = 11.3 \pm 0.1\,K$ at the centre of the transition (onset at $11.5\,K$), $\frac{\Delta C(T_C)}{T_C} = 8.6 \pm 0.1\,mJ/K^2/mol$, $\gamma = 6.95 \pm 0.03\,mK/K^2/mol$. Error bars are smaller than symbols at all temperatures. Also shown is a BCS curve (black line) calculated from the tabulated values of Mühlschlegel [28] with $T_C = 11.3\,K$ and $C_{en}(T_C) = \gamma T_C = 7.12 T_C\,mJ/K/mol$. 95

3.34 $H_{C2}(T)$ estimated from heat capacity measurements at the CaC_6 superconducting transition. T_C is measured at the mid-point of the transition and is shown with an error bar corresponding to the transition width. At fields greater than $1.5\,kOe$ the transition is too heavily smeared to measure. The red line is a linear fit to the data with $H \leq 1\,kOe$ indicating $H_{C2}(T = 0) = 2.31 \pm 0.02\,kOe$. 96

3.35 Sommerfeld constant γ as a function of magnetic field at $2\,K$. Note: While recording the superconducting heat capacity anomaly as a function of magnetic field it was observed that field history affected the outcome. For fields of $250\,Oe$ and $500\,Oe$ the field was applied at $2\,K$ and data recorded as the sample warmed through T_C. In all other cases the field was applied with $T > T_C(H = 0)$. At temperatures close to $T_C(H)$ no hysteresis effects were seen (this is clear from the linear relationship in figure 3.34). However, at low temperatures ($T < 4\,K$) behaviour for $H = 250\,Oe$ and $H = 500\,Oe$ is erroneous, due to pinning and surface barrier effects. Data points at fields $H = 250\,Oe$ and $H = 500\,Oe$ were omitted from the figure for this reason. 97

3.36 $\frac{\Delta C}{T}$ as a function of temperature for CaC_6 (blue points). The black line represents the BCS curve calculated from the tabulated values of Mühlschlegel [28]. The red line shows the high and low temperature behaviour of the anisotropic gap BCS model with $< a^2 >= 0.05$ [29]. This model is not applicable to the regime $0.3 < \frac{T}{T_C} < 0.7$ although a smooth interpolation between the low and high temperature ranges is expected. . 98

4.1 Schematic representation of electron energy states localised in space in the ES system. Left: A set of localised states at $T = 0$. All states below the Fermi level are occupied while all states above the Fermi level are unoccupied. Right: An electron from below the Fermi level is moved to a state above the Fermi level, leaving a hole behind. The shaded region represents the resulting Coulomb interaction between the electron and hole. 106

4.2 Resistivity as a function of temperature in-plane of two kish graphite samples showing typical behaviour. Key designations are according to RRR. Data taken from [30, 31]. 109

4.3 Resistivity as a function of temperature in-plane of two natural graphite samples showing typical behaviour. Published relative resistance values have here been scaled by absolute values of resistivity in similar samples measured by Primak of $\rho_{ab}(300\,K) = 4.0\text{x}10^{-7}\,\Omega m$. Key designations are according to RRR. Data taken from [32]. 109

4.4 Resistivity as a function of temperature in-plane of four HOPG graphite samples showing typical behaviour. Key designations are according to RRR for purely metallic samples only. Data taken from [33, 34]. 110

4.5 Resistivity as a function of temperature along the c-axis of five kish graphite samples showing typical behaviour. This data is presented normalised in figure 4.6. Key designations are according to RRR. Data taken from [35]. 110

4.6 $\rho_C(T)/\rho_C(300\,K)$ of the five kish graphite samples shown in figure 4.5. Key designations are according to RRR. Data taken from [35]. 111

4.7 Resistivity as a function of temperature along the c-axis of two kish graphite samples showing typical behaviour. RRR values are not available for these measurements. Data taken from [36]. 111

4.8 Resistivity as a function of temperature along the c-axis of two natural graphite samples showing typical behaviour. Published relative resistance values have here been scaled by absolute values of resistivity in similar samples measured by Primak of $\rho_c(300\,K) = 5\text{x}10^{-5}\,\Omega m$. RRR values are not available for these measurements. Data taken from [32]. . 112

4.9 Resistivity as a function of temperature c-axis of four HOPG graphite samples showing typical behaviour. Samples are the same as those presented in figure 4.4. Key designations are according to RRR for purely metallic samples only. Data taken from [33, 34]. 112

4.10 Schematic of the FIB-milled structure used to study superconductivity in high temperature superconductors. The ab direction is in-plane; c is the cross-plane direction. Figure adapted from [37]. 115

4.11 Scanning electron microscope (SEM) image of a 1 μm x 1 μm stack device. Figure taken from [38]. 115

4.12 Left: Temperature dependence of the scaled resistance of the device and an in-plane measurement of a graphite sample from the same batch. Right: Temperature dependence of $\frac{dI}{dV}$ as a function of voltage for the natural graphite device. Figures adapted from [39]. 117

4.13 Left: Resistance as a function of temperature for the HOPG $1\,\mu m$ x $1\,\mu m$ x $100\,nm$ stack device showing semiconducting-like dependence (curve fit is a c-axis conduction fit based on [40, 34]) Inset: precursor HOPG flake. Right: IV characteristics at $300\,K$ and $20\,K$ for $1\,\mu m$ x $1\,\mu m$ x $100\,nm$ and $1\,\mu m$ x $1\,\mu m$ x $200\,nm$ devices showing linear behaviour at 300 K and smooth nonlinear behaviour at $20\,K$. Figures adapted from [41]. 117

4.14 Conductance as a function of voltage for the $1\,\mu m$ x $1\,\mu m$ x $100\,nm$ stack device. Note the absence of the pseudogap feature observed in [39]. Figure adapted from [41]. 118

4.15 Main stages involved in macro- and microscopic processing of graphite flakes to form stack devices. From left to right: Bulk flake is cleaved to thin and then trimmed to narrow; current (I) and voltage (V) contacts are deposited and the stack device fabricated by FIB milling between the voltage contacts. 119

4.16 Rocking curve of [002] x-ray diffraction peak (theta-theta scan). 120

4.17 Left: SEM image of initial kish top surface. Right: SEM image of kish top surface after several cleaves. 121

4.18 Optical microscopy of a kish graphite cleave showing large areas of flat, undisturbed graphite. Images share a common centre. 121

4.19 SEM image of macroscopic graphite sample mounted on a SiO_2 substrate after gold deposition. Light areas are gold, dark lines are regions from which deposited gold has been mechanically removed to electrically separate contacts. 122

4.20 The Carl Zeiss XB1540 Cross-Beam SEMFIB. 123

4.21 View inside the vacuum chamber of samples mounted on flat stage for top-down (left) and angled stage for lateral milling (right) showing SEM and FIB gun positions. 124

4.22 Schematic representation of FIB milling process to form stack devices. (a) Initial top down milling narrows the $\sim 300\,\mu m$ wide sample to several microns and defines a target device region; (b) the target region is further narrowed to a width of $1\,\mu m$; (c) the sample is repositioned such that the FIB beam is parallel to the substrate and two lateral cuts are made, leaving an undisturbed region of $1\,\mu m$ x $1\,\mu m$ in between; (d) the lateral cuts overlap by a height of $230\,nm$ (device A) and $290\,nm$ (device B) creating the stack device in the circled area. 125

4.23 Overview (left) and close-up (right) of stack device A after major cuts, at the point of site selection. 126

4.24 Overview (left) and close-up (right) of stack device B after major cuts. . . 126

4.25 FIB view of stack device A during lateral milling. 127

4.26 False-colour SEM image of stack device A viewed along the lateral cut. . 128

4.27 False-colour SEM image of stack device B. 129

4.28 Additional graphite-based stack device showing a shear fracture at the stack site. 130

4.29 Two devices fabricated from CaC_6 precursors. 130

4.30 IV characteristics for stack device A between $246\,K$ and $2\,K$. 133

4.31 Numerical $\frac{dI}{dV}$ for stack device A between $246\,K$ and $2\,K$. Values calculated from IV characteristics shown in figure 4.30. 133

4.32 Resistance as a function of temperature for stack device A between $250\,K$ and $2\,K$. 134

4.33 IV characteristics for stack device B between $200\,K$ and $4\,K$. 135

4.34 Numerical $\frac{dI}{dV}$ for stack device B between $200\,K$ and $4\,K$. Values calculated from IV characteristics shown in figure 4.33. 135

4.35 Resistance as a function of temperature for stack device B between $200\,K$ and $4\,K$. Resistance values are calculated as the inverse gradient of the IV characteristics shown in figure 4.33. 136

4.36 Schematic representation of the series combination of the resistance due to the device (R_{device}) with that of the ab-plane leads where $R_{leads}(T) = R_1(T) + R_2(T)$. 137

4.37 Estimated resistivity of lead sections of devices A and B. Device A shows a metallic behaviour at all temperatures ($\frac{d\rho}{dT} < 0$) while device B has $\frac{d\rho}{dT} < 0$ at low temperatures but for $T \gtrsim 140\,K$ $\frac{d\rho}{dT} > 0$ showing an additional contribution. Resistivity is calculated as $\rho_{leads} = [R(T) - R(2\,K)] \left[\frac{A_{lead}}{l_{lead}}\right]$.138

4.38 Estimated mean free path for devices A and B. Black horizontal lines are positioned at the device width of $W = 1\,\mu m$ and average device c-axis height of $h_c = 290\,nm$. Black arrow is positioned at $130\,K$, the temperature at which R_{device} for device B begins to decrease. 139

4.39 Conductance of device A as a function of voltage for $T \leq 56\,K$ showing the development of the pseudogap centred at zero bias. Curves have been vertically offset for ease of viewing but share a common scale. . . . 140

4.40 Low voltage region of the conductance of device A as a function of voltage for $10\,K \leq T \leq 56\,K$ showing the development of the pseudogap centred at zero bias. Grey arrow indicates decreasing temperature. Curves have been vertically offset for ease of viewing but share a common scale. 141

4.41 Low voltage conductance of device A at 10K. Red line is a fit to equation 4.17 with parameters $G_0 = 0.58153 \pm 0.00007\,S$, $m = 2.2 \pm 0.2$ and $E_C = 49 \pm 3\,mV$. 142

4.42 Fitted pseudogap size E_C (blue points) as a function of temperature - individual values given in table 4.3. Grey points are estimated values as described in the text. 143

4.43 Conductance of device A as a function of voltage for $2\,K \leq T \leq 10\,K$ showing the complex gapping at low temperatures. Curves have been vertically offset for ease of viewing but share a common scale. 144

List of Tables

2.1 Concentrations of magnetic impurities in samples of HOPG (AC1/2, UC3/4, HOPG-2/3), kish and natural (Ticonderoga, USA) graphites. All concentrations are in units of $\mu g/g$. [a]The Fe concentration in this sample is not homogeneous; in two different positions the values were $13\,\mu g/g$ and $165\,\mu g/g$. Data taken from [42]. 33

2.2 Structural parameters of stage-1 donor-GICs, with the subjects of this thesis highlighted. Data taken from [43, 44] 38

3.1 CDW transitions in the layered dichalcogenides. N $\rightarrow$ ICDW signifies a transition from the normal state to the incommensurate CDW state. CCDW $\rightarrow$ ICDW signifies a transition from the commensurate CDW state to the incommensurate CDW state. Data taken from [14]; column 6 from [45]. 57

3.2 Superconducting group I, II and III donor-GICs, their transition temperatures and discovering references. *Metastable compound formed under high pressure. 62

3.3 Overview of the intercalation methods used. 72

3.4 GIC sample quality assessment from x-ray diffraction patterns shown in figure 3.18. 72

3.5 Table of fit coefficients for curve shown in figure 3.26. Θ_D value calculated from β using equation 3.5. 81

3.6 Table of Sommerfeld constants γ and Debye temperatures Θ_D of graphites and alkali-metal GICs. *Grayson-Alexander 1980 82

3.7 Values of the electron-phonon coupling λ_{el-ph} as estimated from the experimental Sommerfeld constant γ and theoretical electronic DOS at the Fermi level $g(E_F)$. ^{a} Data taken from [11]. 83

3.8 Values of δ for group I and group II GICs. 85

3.9 Table of coefficients to fits to equation 3.21 for curves shown in figures 3.28 and 3.29. 88

3.10 Comparison of $NbSe_2$ and CaC_6. 91

4.1 Values of RRR, λ_{MFP} at $4.2\,K$ and average in-plane crystallite size for kish and HOPG samples. Data taken from ^{a}[3] and ^{b}[46]. 108

4.2 Dimensions of the graphite samples after macroscopic preparation. $^*\pm$ represents variation in dimension across sample as seen under SEM imaging, not uncertainty. 122

4.3 Fit parameters of equation 4.17 to $\frac{dI}{dV}(V)$ of device A for $10\,K \leq T \leq 56\,K$. 143

Nomenclature

AC	Alternating Current
BCS	Bardeen Cooper Schrieffer
CCDW	Commensurate Charge Density Wave
CDW	Charge Density Wave
CITS	Current Imaging Tunneling Spectroscopy
DC	Direct Current
DFT	Density Functional Theory
DOS	Density of States
ECCI	Electron Channeling Contrast Imaging
ECP	Electron Channeling Pattern
FIB	Focused Ion Beam
GIC	Graphite Intercalation Compound
HOPG	Highly Oriented Pyrolytic Graphite
ICDW	Incommensurate Charge Density Wave
IV	Current-Voltage
LDA	Local Density Approximation
MIT	Metal-Insulator Transition
PPMS	Physical Properties Measurement System

RRR Residual Resistance Ratio

SDW Spin Density Wave

SEM Scanning Electron Microscopy

STM Scanning Tunneling Microscopy

STS Scanning Tunneling Spectroscopy

SWMcC Slonczewski Weiss McClure

TEM Transmission Electron Microscopy

WHH Werthamer Helfand Hohenberg

Chapter 1

Introduction

1.1 Graphitic Systems

Graphite has a layered structure which gives it highly anisotropic electronic properties; e.g. the ratio of the in-plane to the interplane electrical conductivities can reach $\sim 10^4$ in highly crystalline samples [47]. It is a metallic conductor but with a very small band overlap which yields a correspondingly low density of carriers [48]. The mean free paths of its carriers have been found to be on the order of 1000 times those of normal metals [49]. The structural anisotropy also gives highly anisotropic vibrational properties due to strong in-plane bonding but very weak interplane bonding [48].

The physical structure of graphite makes its electronic and vibrational properties and behaviours easily altered and tuned [2]. The weak bonding between the layers in graphite allows the easy accommodation of foreign species ('intercalants') which alter its electronic and vibrational properties, the resulting compounds being termed graphite intercalation compounds [50]. Graphite is an amphoteric substance, meaning that it can act as either a donor or an acceptor of charge so that intercalants can increase or reduce the occupation of the graphitic bands, as well as introduce new bands [48]. The presence of intercalates also alters interlayer interactions and introduces new vibrational modes [48]. In the mid-1960s it was discovered that these modified electronic and vibrational spectra could result in superconductivity [51] and since then many superconducting graphite intercalation compounds have been discovered. Most recently the alkali earth metal graphite intercalation compounds CaC_6 and SrC_6 have been seen to superconduct [52, 22], while theoretical studies have also predicted superconductivity

in another group II graphite intercalation compound, BaC_6 [53, 11].

Due to its mean free path electrical transport in graphite is very sensitive to system size. The very long mean free path means that low-dimensional phenomena usually only seen in metals at nanometre sizes and liquid helium temperatures can become evident in graphitic systems with micro- and even macroscopic dimensions and at temperatures up to room temperature [54, 4]. Electrical transport in micron-sized graphitic systems created by advanced microfabrication techniques has been observed to stop behaving Ohmically and instead exhibit ballistic characteristics [49, 55].

1.2 Aims, objectives and motivation

This doctoral work began as the study of the potential applications of graphitic microstructures to electrical engineering, both in their raw and Ca intercalated, superconducting forms. Micro-size graphitic cone structures thought to be single crystals were to be studied as potential FETs, while graphitic fibres with a herringbone-type internal structure had potential wiring applications. The particular interest in these materials stems from their intrinsic, 'ready made' micro and nano dimensions, as well as their potential to exhibit properties similar to those of graphene. The normal and superconducting states of both types of structure would be studied using low temperature electrical transport measurements, with contact made using FIB-deposited metals.

At the same time, other members of the UCL Carbon Physics group were performing STM experiments showing a charge density wave state in CaC_6 at liquid nitrogen temperatures. This discovery was of particular import as it was the first such reporting of a charge density wave in a graphitic material. It was decided to apply the skills and techniques gained with the handling, intercalating, contacting and testing of the microstructures in experiments to study the new charge density wave state. Following the work of Latyshev et al FIB milling would be applied to CaC_6 samples to create micro-sized devices, contacted using the remaining, unmilled sample. Electrical transport measurements would then be performed over a wide temperature range to observe the charge density wave gap, the superconducting gap and their temperature dependence. Additionally, heat capacity measurements would be performed on macro samples of CaC_6 to further describe the new charge density wave state, as well as to verify previous findings on the superconducting state.

For both the planned electrical transport experiments and heat capacity experiments on CaC_6 equivalent studies of raw graphite and other MC_6 GICs were to be used to gener-

ate a more complete picture and further substatiate results. Additionally, this approach would allow us to connect to the wider body of work in this area in two particular ways. Firstly, in the case of superconductivity in MC_6 GICs, it would allow us to contribute to discussion on the predicted but as yet unobserved superconducting state of BaC_6 and verify recently observed supeconductivity in SrC_6. Secondly, in the case of electrical transport in graphitic micro-structures, it would allow us to repeat and potentially verify the pseudogap observations of Latyshev et al in graphite.

1.3 Form of the Dissertation

The thesis begins with a common, background theory section on the materials before dividing into two to address firstly superconductivity and charge density wave heat capacity studies, and secondly pseudogap electrical transport studies, before coming back together for a joint conclusion:

Chapter 2 introduces graphite and graphite intercalation compounds and details their main structural, vibrational and electronic properties.

Chapter 3 presents heat capacity studies of the superconducting states of CaC_6, SrC_6 and BaC_6, as well as a charge density wave state in CaC_6. Initially, the theoretical basis of the heat capacity is described and an experimental perspective of the superconducting and charge density wave states and their competition is given. By way of specific introduction previous work studying superconductivity in MC_6 graphite intercalation compounds is discussed and a recent paper which discovered a charge density wave state in CaC_6 is described. Sample preparation and quality are detailed preceding a description of the experimental setup and presentation of the heat capacity measurement results. For each of CaC_6, SrC_6 and BaC_6 the low temperature heat capacity is described by a Debye model with an additional low energy intercalant mode. The fitted electronic coefficients yield calculations of the electron-phonon coupling for comparison with theory for each of the three studied compounds. Attempts to observe the charge density wave onset in the high temperature heat capacity of CaC_6 are presented, and the nature of the compound's superconductivity is discussed in the context of anisotropy of the order parameter and competition with the charge density wave state.

Chapter 4 presents electrical transport studies of a micro-machined graphite system. As background, the theoretical basis of electrical transport in a number of systems is outlined before the electrical resistance of graphites is examined and the previous use of microfabrication techniques to create similar test systems is detailed. Specific

processing and experimental setup details are then given and electrical transport results presented. Resistance measurements as a function of temperature are described by ballistic transport through a constriction, while an observed pseudogap is analysed in the context of Coulomb interactions. The use of micro-devices to study the conductivity mechanisms of ideal graphite is also discussed.

Chapter 5 concludes across both pieces, providing a summary of the findings of this work against its aims and next steps.

Chapter 2

Materials

2.1 Graphite

2.1.1 Structural Properties

Graphite consists of layered sheets of graphene - 2D planes of hexagonally arranged carbon atoms - with an AB stacking order, as shown in figure 2.1. Within the planes atoms are connected by strong covalent bonds ($7\,eV/atom$ binding energy), whereas between planes bonding is by weak van der Waals forces ($0.02\,eV/atom$) [56, 57].

Each graphene sheet lies in the ab plane, while the interplane direction is the c-axis. The planes are separated by a distance $d_c = 3.35\,\mathring{A}$ along the c-axis, more than twice the intralayer nearest-neighbour distance $a_{NN} = 1.42\,\mathring{A}$ [1]. This arrangement makes graphite highly anisotropic; e.g. it has extremely high thermal conductivity, strength and stiffness along the planes but it is a bad thermal conductor across the planes and is easily cleaved.

The graphite unit cell (marked in figure 2.1) contains four atoms: two atoms for each graphitic plane and two planes per cell. It has dimensions: $c_0 = 6.708\,\mathring{A}$ and $a_0 = 2.456\,\mathring{A}$ [48]. The corresponding Brillouin zone in the reciprocal lattice is shown in figure 2.2.

Macroscopic samples of graphite with the ideal structure don't exist in nature. Crystal boundaries, defects, impurites and stacking faults combine in varying quantities to disrupt the perfect structure in real graphites such as kish, natural and highly-oriented

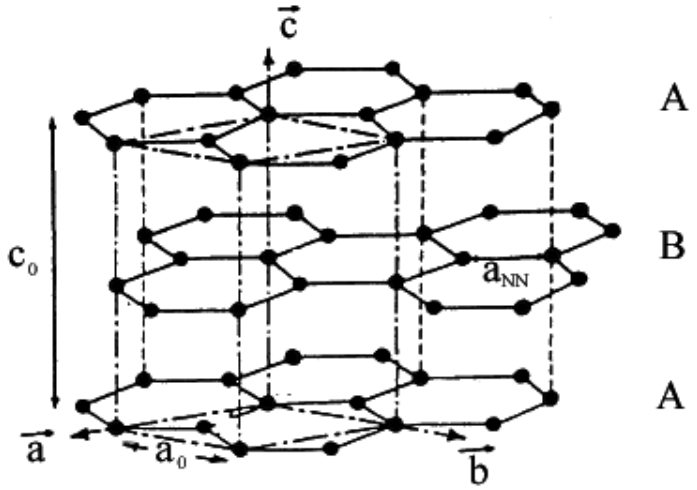

Figure 2.1: Crystalline structure of hexagonal graphite. The dimensions of the unit cell, represented by dotted-dashed lines, are $a_0 = 2.456\,\mathring{A}$ and $c_0 = 6.708\,\mathring{A}$. $a_{NN} = 1.42\,\mathring{A}$ is the distance between nearest neighbours. In the c-direction the graphene sheets are registered in an AB stacking order and are separated by $d_c = 3.35\,\mathring{A}$. Figure adapted from [1].

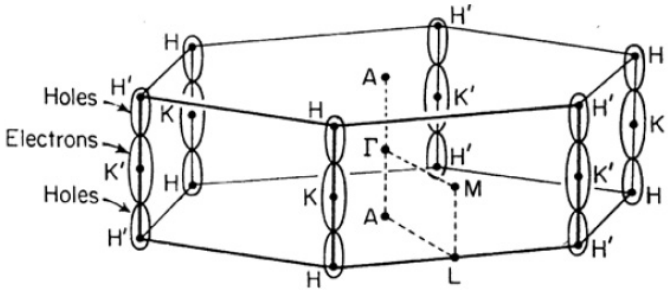

Figure 2.2: Brillouin zone of graphite, showing several high-symmetry points and a schematic version of the graphite electron and hole Fermi surfaces located along the $H - K$ axes. Symmetric points are labelled with Bouckaert-Smoluchowski-Wigner notation ($\Gamma AHKLM$). The direction $\Gamma - A$ is perpendicular to the graphene sheets; $\Gamma - K$ is parallel to the graphene sheets. Figure taken from [2].

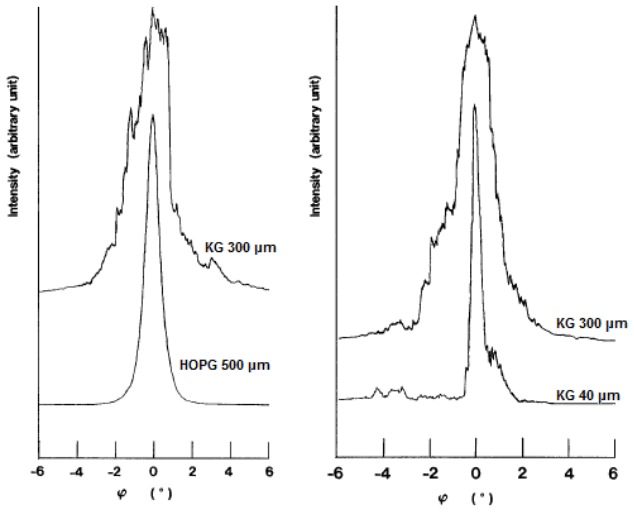

Figure 2.3: Rocking curve of [002] x-ray diffraction peak (theta-theta scan). Left: $300\,\mu m$ thick kish graphite (KG) flake and $500\,\mu m$ thick HOPG sample. Right: A different kish graphite sample at $300\,\mu m$ thick and cleaved to $40\,\mu m$ thick. Figure adapted from [3].

pyrolytic graphites (HOPG). Their differing properties are detailed below, with structure described first for each and then purity.

Kish graphite is typically a byproduct of the steel-making process, formed as crystalline flakes of graphite precipitated from a carbon-rich iron melt [58]. It is more highly crystalline than HOPG but less so than natural single crystal graphite [36]. The flakes contain either one crystallite or a series of fairly well aligned crystallites. In-plane crystallite sizes are typically several hundreds of microns and can be up to $\sim 1000\,\mu m$, as shown by electron channeling contrast imaging (ECCI) in the upper panel of figure 2.4 [3]. Electron channeling patterns (ECP) also show single-crystal patterns over large areas. c-axis crystallite sizes are typically on the order of $\sim 100\,nm$ [59]. X-ray diffraction studies of the [002] (c-axis) reflection of kish graphite flakes tend to show a broad peak composed of many narrow peaks arising due to its highly crystalline polycrystal composition (figure 2.3). Typical flakes are $\sim 300\,\mu m$ thick and have a full-width at half maximum ('mosaic spread') $\sim 3.5^{\,o}$, showing the considerable variation in the orientation of the c-axis between crystallites. Flakes of thickness $\sim 40\,\mu m$, achieved by cleaving show a single, narrow peak with width $\lesssim 0.5^{\,o}$ (figure 2.3, right panel), indicating a far smaller number of crystallites but with the same high crystallinity [3].

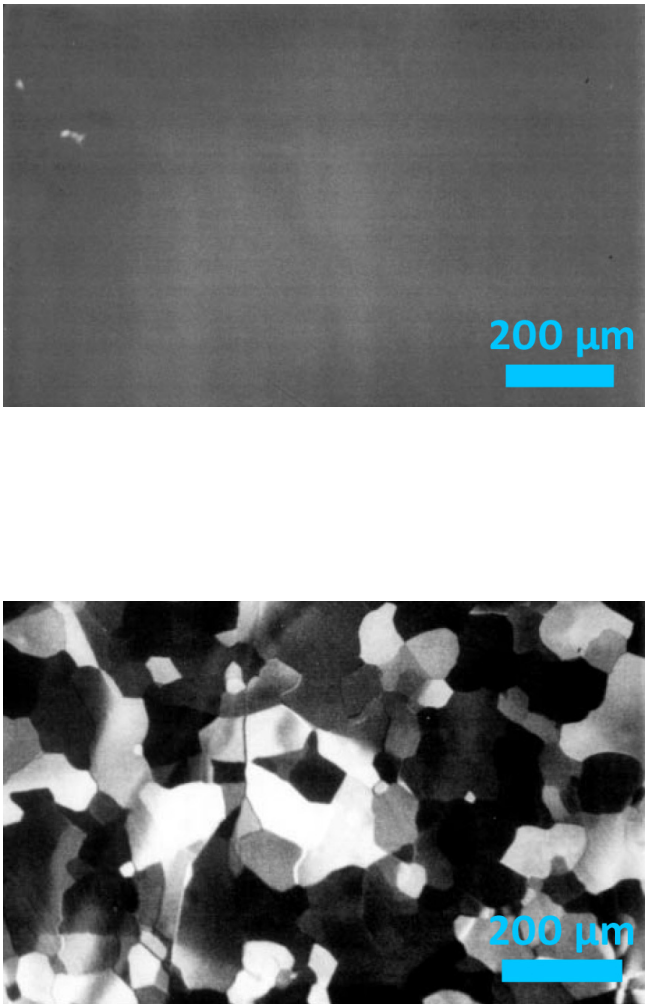

Figure 2.4: Upper: ECCI image of a kish graphite surface. The lack of contrast indicates that the crystallite size is greater than the field of vision of the image. Lower: ECCI image of an HOPG surface showing the typical extent of the in-plane crystallites as $\sim 60\,\mu m$. This sample has a mosaic spread of 0.9^{o}. Figure adapted from [3].

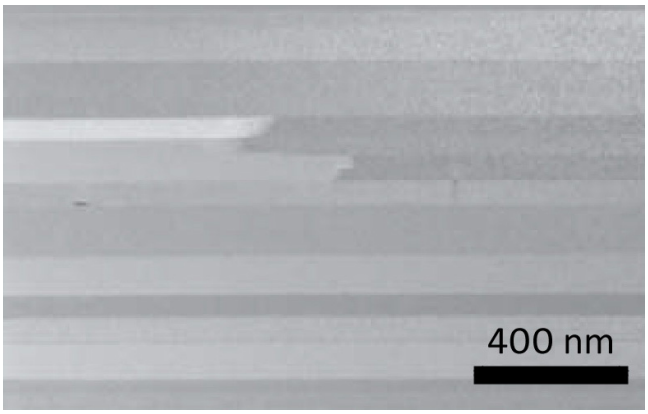

Figure 2.5: TEM image of an HOPG sample (mosaic spread $0.4\,^o$) taken parallel to the graphene layers. The c-axis is perpendicular to the clearly observable stripes of different grey colours, each representing a crystalline region with a different orientation. Typical c-axis crystallite sizes are $60 \pm 20\,nm$. Figure adapted from [4].

Within crystallites kish graphite has a much higher concentration of crystal defects than either natural graphite or HOPG [3] (this point is discussed further in section 4.3.1 for each of kish, natural and HOPG graphites).

Natural graphite is mined in countries such as China, Brazil, Madagascar, Russia and Sri Lanka. It is formed in metamorphic and igneous environments under high temperature and pressure. In terms of crystallinity it is very similar to kish graphite, although with a much lower crystal defect concentration [3].

HOPG is a synthetic graphite formed by heat treatment of pyrolytic carbon at high temperatures ($\sim 3600\,^oC$) and under pressure. It is less highly crystallised than both kish and natural graphites with ECP studies showing a superposition of distorted patterns demonstrating its polycrystalline nature [3]. ECCI shows a typical in-plane crystallite size of $\sim 60\,\mu m$, as shown in the lower panel of figure 2.4, although it has been noted that these crystallites may actually consist of slightly misaligned smaller crystallites with dimensions $\sim 6\,\mu m$ [46]. Crystal defect concentrations are higher than natural graphite but considerably lower than in kish graphite.

Figure 2.5 shows a transmission electron microscopy (TEM) image of an HOPG sample showing typical c-axis crystallite sizes of $60 \pm 20\,nm$ [4]. X-ray diffraction studies of the [002] reflection show a single, gaussian peak with mosaic spread $0.4 - 3.5\,^o$ (figure 2.3, left panel), indicating that its graphene planes can be very well aligned along the c-axis. However, the ECP and ECCI studies show that the orientation of the crystallites

in-plane is random.

Due to the method by which it is formed the concentrations of impurities in raw kish graphites are much greater than those of natural and HOPG graphites [60]. These impurities are mainly of two forms: non-metallic and metallic particles. The former consist of calcium, silicon and iron oxides; the latter iron particles. These particles are adhered to the outer surface of the flakes and so can be removed by washing or cleaving. Very small amounts of iron particles can become trapped in the foliated structure, with concentrations typically estimated at a maximum of $\sim$few ppm [61, 31].

Natural graphites can also contain appreciable concentrations of impurities though of a different composition to kish, being predominantly Ca, Fe, Al and Mg - a comprehensive list and discussion are given in [32] - while HOPG is generally considered to have the highest purity due to its formation process. However, a recent study of the magnetic impurities of kish, natural and HOPG graphites found a great deal of variation in impurity concentrations, not only across graphite types but also within each type [42]. Table 2.1 reproduces some of the findings showing the wide range of impurity concentrations observed. The work suggests that impurity concentrations cannot be inferred from graphite type.

2.1.2 Vibrational Properties

The layered structure of graphite gives rise to strongly anisotropic lattice dynamics [2]. The strong intralayer, covalent bonds and the low mass of the carbon atom yield high frequency/energy intralayer modes, while the significantly weaker interlayer interaction gives low frequency modes. These are shown schematically in figure 2.6.

Phonons are the quasi-particles that describe the quantized lattice vibrations of a crystal. A crystal possesses $3N$ phonon branches where N is the number of atoms in the unit cell. Since the graphite unit cell consists of four atoms this gives 12 phonon branches although it is commonly approximated by that of graphene where the two atom unit cell gives six branches, as most of the phonon branches of graphite are nearly doubly degenerate. The phonon dispersion relation is shown in figure 2.7.

Impurity	AC1	AC2	UC3/UC4	HOPG-2	HOPG-3	Kish	Natural
Fe	13 ± 1	< 0.3	16 ± 2	8 ± 2	7.8 ± 2	0.7 ± 0.3	[a]
Ni	1.3 ± 0.5	< 0.4	2.1 ± 0.7	0.8 ± 0.5	< 0.2	< 0.4	3 ± 2
Mn	< 0.3	< 0.3	< 0.2	< 0.2	< 0.2	< 0.3	10 ± 5
Cu	16 ± 2	< 0.5	73 ± 5	1.2 ± 0.5	1.3 ± 0.5	< 0.5	3 ± 2
Ca	< 0.7	< 0.7	56 ± 6	2.6 ± 0.8	9.7 ± 2.5	< 0.7	100 ± 30
Ti	9 ± 2	7 ± 1	3.3 ± 1	0.8 ± 0.5	1.0 ± 0.7	< 0.5	< 1

Table 2.1: Concentrations of magnetic impurities in samples of HOPG (AC1/2, UC3/4, HOPG-2/3), kish and natural (Ticonderoga, USA) graphites. All concentrations are in units of $\mu g/g$. [a]The Fe concentration in this sample is not homogeneous; in two different positions the values were $13\,\mu g/g$ and $165\,\mu g/g$. Data taken from [42].

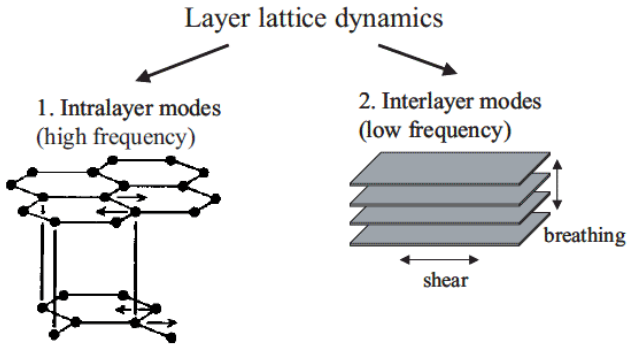

Figure 2.6: Schematic diagram of the layer lattice dynamics of graphite. The lattice dynamics are characterised by high-frequency intralayer modes and low frequency interlayer modes, the latter separated into layer breathing, layer shear and bending modes. The intralayer modes occur at energies above $\sim 125\,meV$, while the interlayer modes occur at lower energies as shown in figure 2.7. Figure adapted from [5].

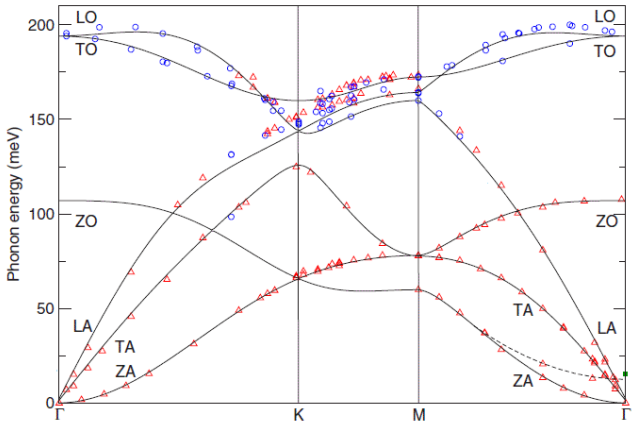

Figure 2.7: Phonon dispersion of graphite from inelastic x-ray scattering (symbols). Solid lines are force-constant calculations for graphene. The dashed line is a quadratic extrapolation of the data. The phonon branches are specified as following: out-of-plane acoustic (ZA), transverse acoustic (TA), longitudinal acoustic (LA), out-of-plane optical (ZO), transverse optical (TO) and longitudinal optical (LO). The vertical lines are denoted by their symmetry representation. Figure adapted from [6].

2.1.3 Electronic Properties

In a single graphene sheet the carbon $2s$, $2p_x$ and $2p_y$ orbitals are hybridized, forming the strongly coupled trigonal bonding and antibonding orbitals [2]. These trigonal orbitals give rise to three bonding and three antibonding $\sigma-$bands, yielding covalent bonds between the carbon atoms in-plane. The remaining p_z orbitals form a single bonding $\pi-$band and a single antibonding π^*-band; the valence and conduction bands respectively. These bands are degenerate at the six equivalent Brillouin zone K point corners through which the Fermi level passes - shown in figure 2.8. As such graphene is modelled as a zero-gap semiconductor.

In the vicinity of each K point the energy is proportional to the magnitude of the wavevector k for both the $\pi-$ and π^*-bands, in contrast to the parabolic energy dispersion in free electron systems. The density of states (DOS) $g(E)$ derived from the electronic dispersion is proportional to the energy E, decreasing linearly as the energy approaches the Fermi level for both the $\pi-$ and π^*-bands giving a characteristic 'V' shape. $g(E)$ for graphene is shown schematically in the left panel of figure 2.9.

In graphite the electronic structure of the graphene sheet is modified by the presence of the adjacent graphene sheets. The graphite unit cell containing four carbon atoms has double the number of π-bands (marked in orange in figure 2.10). These bands are subject to a weak interlayer interaction that causes a small band overlap of $\sim 40\,meV$ at the Fermi level, yielding one electron and two hole pockets between the K and H points (figure 2.2). This overlap gives rise to a low carrier concentration at the Fermi level of $\sim 10^{18}\,cm^{-3}$ [48] (vs $\sim 10^{23}\,cm^{-3}$ in a metal) and the semi-metallic behaviour of graphite. The derived electronic DOS is shown schematically in the right panel of figure 2.9. In addition, the interlayer interaction yields a free-electron-like, parabolic band above the Fermi level, distributed in the space between the graphene sheets. This is the interlayer band, marked in blue in figure 2.10.

The full band structure of graphite may be calculated using the semi-phenomenological Slonczewski-Weiss-McClure (SWMcC) model [62, 63]. A thorough discussion of the band structure of graphite is contained in the extensive review by Dresselhaus [2].

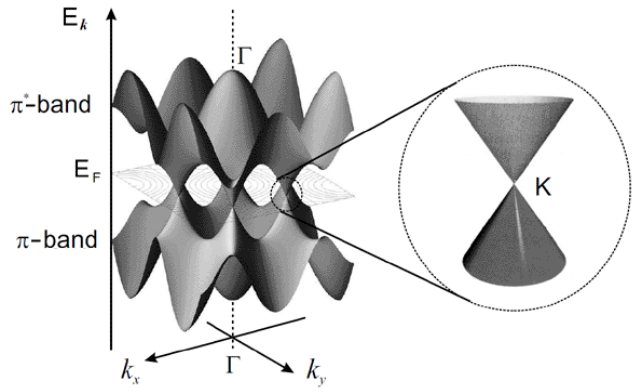

Figure 2.8: Left: Band structure of graphene. The $\pi-$band is completely filled in the ground state and touches the empty π^*-band at the K point where both bands have conical shape. Right: Zoom-in of the energy bands close to one of the Dirac points. Figure taken from [7].

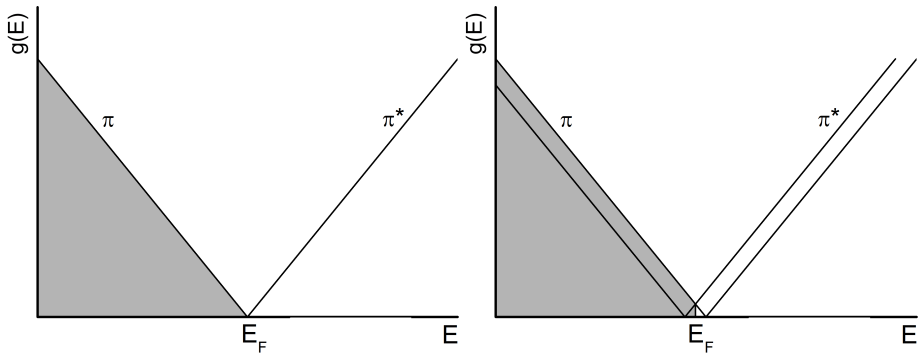

Figure 2.9: The electronic structures shown schematically of (left) graphene and (right) graphite, where $g(E)$ is the DOS as a function of energy and E_F is the Fermi energy.

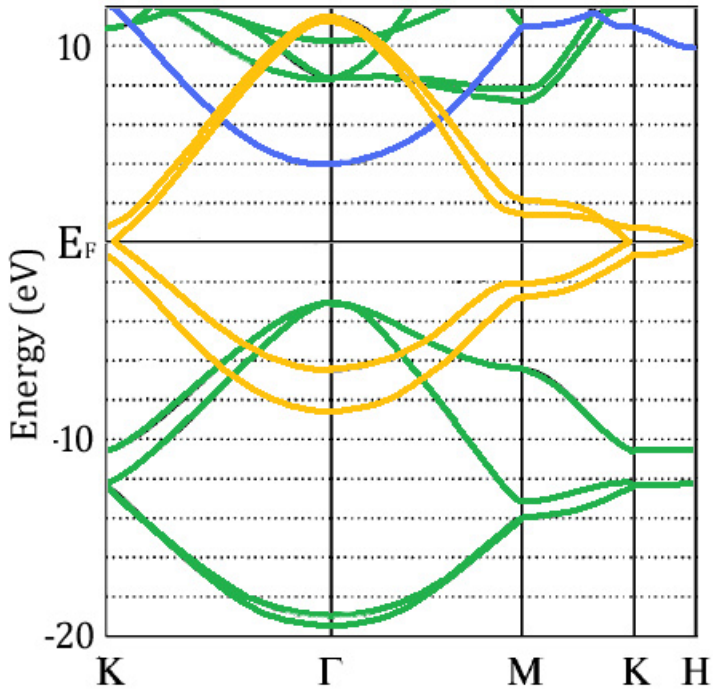

Figure 2.10: Density functional theory (DFT), local density approximation (LDA) calculated electronic band structure of graphite along high-symmetry directions in the Brillouin zone. Band types are colour-coded as: π orange; σ green; interlayer blue. $\pi-$ and $\sigma-$bands are below the Fermi level, π^{*-} and $\sigma^{*}-$bands are above the Fermi level. Figure adapted from [8].

2.2 MC_6 Graphite Intercalation Compounds

2.2.1 Structural Properties

Graphite intercalation compounds (GICs) are layered compounds consisting of graphene sheets with guest elements or molecules in the galleries between them. In GICs the in-plane C-C bond length varies from that of graphite by less than $1\,\%$ [64] but the c-axis spacing can change by up to $200\,\%$ upon intercalation [2].

Along the c-axis GICs exhibit a unique ordering called 'staging'. On intercalation the intercalant fills some galleries preferentially in an ordered way, giving complete layers of intercalant between graphene sheets. A stage n GIC has n graphene sheets between successive intercalant layers.

The stacking of the graphene layers in GICs is sheared from the AB stacking of graphite such that each graphene layer has identical registry: AA stacking. The intercalant species in between can have a stacking sequence as simple as $\alpha\alpha$ as in LiC_6 or as complex as $\alpha\beta\gamma\delta$ as in KC_8. The subjects of this work are the stage-1 GICs CaC_6 with stacking $A\alpha A\beta A\gamma$ and BaC_6 and SrC_6 both with stacking order $A\alpha A\beta$. These structures are shown in figures 2.11 and 2.12, respectively, and further detailed in table 2.2.

Material	Structure		a_{NN} ($\mathring{A}$)	d_c ($\mathring{A}$)
Graphite / C_6	AB	$P6_3/mmc$	1.420	3.350
LiC_6	$A\alpha$	$P6/mmm$	1.435	3.706
KC_8	$A\alpha A\beta A\gamma A\delta$	$Fddd$	1.432	5.320
RbC_8	$A\alpha A\beta A\gamma A\delta$	$Fddd$	1.431	5.618
CsC_8	$A\alpha A\beta A\gamma$	$P6_22$	1.431	5.928
CaC_6	$A\alpha A\beta A\gamma$	$R\bar{3}m$	1.430	4.520
SrC_6	$A\alpha A\beta$	$P6_3/mmc$	1.439	4.940
BaC_6	$A\alpha A\beta$	$P6_3/mmc$	1.434	5.250
EuC_6	$A\alpha A\beta$	$P6_3/mmc$	1.438	4.870
SmC_6	$A\alpha A\beta$	$P6_3/mmc$	1.437	4.580
YbC_6	$A\alpha A\beta$	$P6_3/mmc$	1.440	4.570

Table 2.2: Structural parameters of stage-1 donor-GICs, with the subjects of this thesis highlighted. Data taken from [43, 44] .

It is perhaps surprising that CaC_6 should have a different structure to SrC_6 and BaC_6. However, its $A\alpha A\beta A\gamma$ structure and $R\bar{3}m$ space group can be described by using

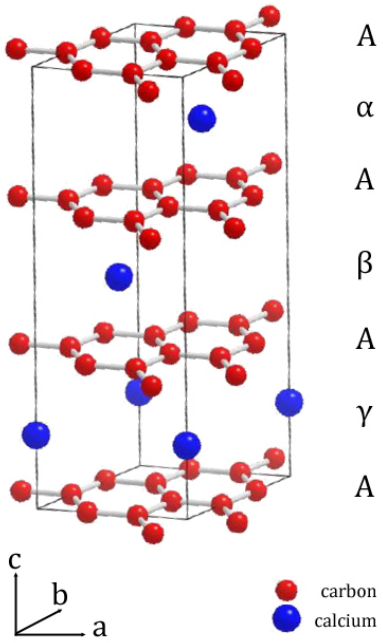

Figure 2.11: Layered structure of stage-1 CaC_6 displaying $A\alpha A\beta A\gamma$ stacking order.

either a hexagonal or rhombohedral basis. Use of the hexagonal representation aids comparison with other GICs and graphite, while the rhombohedral representation is more commonly used by theoretical groups. The reciprocal space Brillouin zones corresponding to each representation are shown for comparison in figure 2.13. In the hexagonal basis the $\Gamma - A$ direction is perpendicular to the graphene sheets, whereas for the rhombohedral basis the equivalent direction is the $\Gamma - L$. The directions parallel to the graphene sheets are $\Gamma - K$ and $\Gamma - \chi - X$, respectively.

2.2.2 Vibrational Properties

The lattice vibrations of GICs have a basis similar to those of graphite but modified by the presence of the intercalant atoms. The graphitic modes consist of the high-frequency intralayer modes and low frequency interlayer modes, as well as the very soft bending or 'ripple' modes, as detailed above and shown in figure 2.6. In addition to these there are modes specific to the intercalant atoms or molecules. These are simple longitudinal and transverse modes for monoatomic intercalate layers or more complex

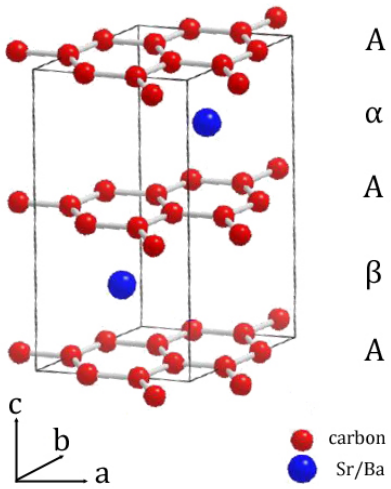

Figure 2.12: Layered structure of stage-1 SrC_6/BaC_6 displaying $A\alpha A\beta$ stacking order.

intramolecular modes for molecular intercalates.

The DFT calculated phonon dispersion of $\mathrm{CaC_6}$ is shown in figure 2.14 [10] - measurements by neutron [65], inelastic x-ray [66, 67] and Raman [68, 69, 70] scattering show reasonable quantitative agreement with the DFT predictions (left panel of figure 2.15).

In $\mathrm{CaC_6}$ the Ca atoms are much heavier and more weakly bonded than the C atoms so the Ca-related phonons occur at the lowest energies ($\lesssim 40\,meV$ as seen in the figure). The strong planar bonding of the graphene sheets means that the out-of-plane C_z modes fall between $40 - 80\,meV$ while the in-plane C_{xy} modes are higher energy and dominate the spectrum from $100 - 180\,meV$.

The similarity of the structures of $\mathrm{MC_6}$ GICs means that their phonon dispersions are broadly the same as that of $\mathrm{CaC_6}$ as detailed above [11]. However, some differences are observed. The greater mass of the intercalant atoms in the cases of $\mathrm{SrC_6}$ and $\mathrm{BaC_6}$ shifts the energy of the intercalant modes down. The graphene C_z modes are softened by increased occupation of the π^*-band, which correlates with decreased interlayer spacing d_c (see table 2.2). This effect is due to the anti-bonding nature of the π^*-band, meaning that greater filling of the band causes the destabilisation of the graphene bonds [64, 68].

The right panel of figure 2.15 shows the phonon dispersion of $\mathrm{BaC_6}$ as measured by inelastic x-ray scattering. The agreement between the experimental measurements

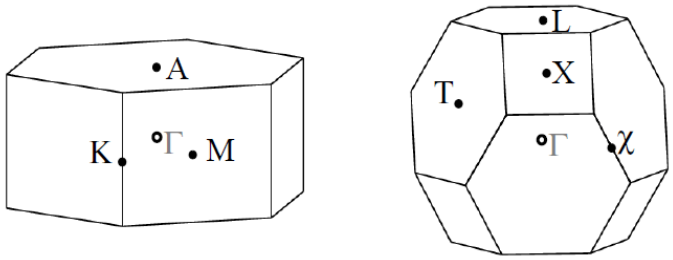

Figure 2.13: Left: The hexagonal Brillouin zone. The direction $\Gamma - A$ is perpendicular to the graphene sheets; $\Gamma - K$ is parallel to the graphene sheets. Right: The rhombohedral Brillouin zone, in which the hexagonal K-point is refolded at Γ. The direction $\Gamma - L$ is perpendicular to the graphene sheets; $\Gamma - \chi - X$ is parallel to the graphene sheets. Figure taken from [9].

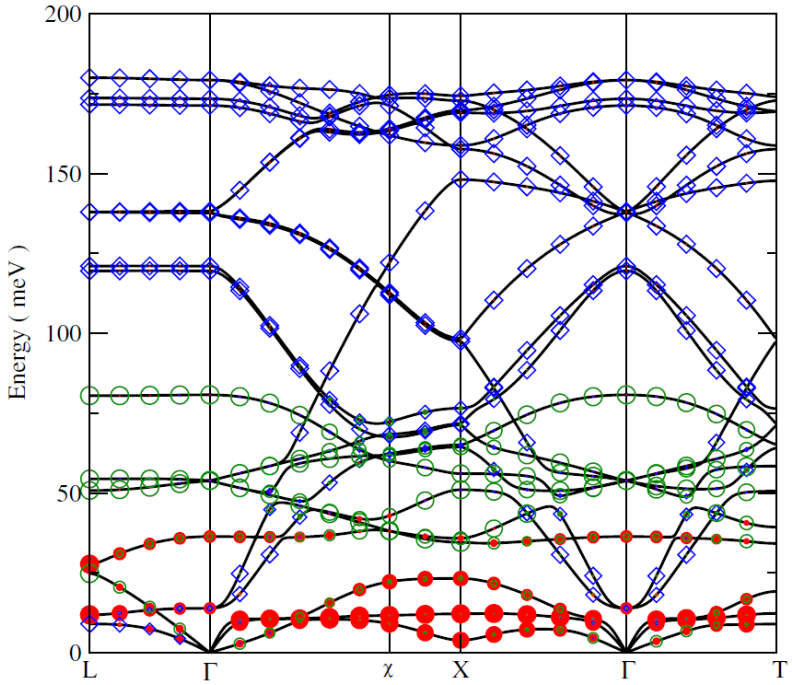

Figure 2.14: DFT calculated phonon dispersion of $\mathrm{CaC_6}$. The amount of Ca vibration is represented by the size of ●, of C_z by the size of ○, and of C_{xy} by the size of ◇. Figure taken from [10].

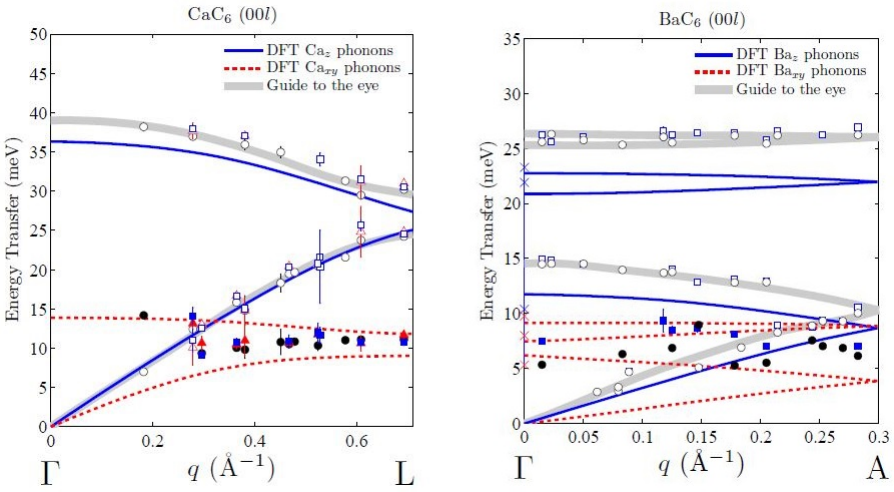

Figure 2.15: Phonon dispersion of $\mathrm{CaC_6}$ (left) and $\mathrm{BaC_6}$ (right) (00l) measured using inelastic x-ray scattering at $5\,K$ (squares), $50\,K$ (triangles) and $300\,K$ (circles). Empty symbols denote M_z phonon intensity, full symbols label M_{xy} phonon intensity. The theoretical dispersion of the M_z and M_{xy} phonons are plotted with solid lines and dashed lines respectively. A guide to the eye is plotted showing the dispersion of the experimental M_z phonons at $300\,K$ (thick solid line). The symmetry point L ($\mathrm{CaC_6}$) is located at $q = 0.694\,A^{-1}$. The symmetry point A ($\mathrm{BaC_6}$) is located at $q = 0.299\,A^{-1}$. The crosses mark the phonon energies calculated at Γ using the experimental lattice parameters and space group of $\mathrm{BaC_6}$. Figures taken from [9].

and the DFT predicted dispersion is significantly less good than for $\mathrm{CaC_6}$ (left panel). Experimentally observed energies are seen to be up to $20\,\%$ above those predicted by DFT calculations.

2.2.3 Electronic Properties

GICs are characterised as either donor or acceptor depending upon whether the intercalant donates charge to the graphene layers or removes it. This behaviour is described most simply by the rigid band model [48, 71] as follows: Electrons transferred from donor to graphene layer occupy the π^*-band in donor-GICs, shifting the Fermi level up above the Dirac point, and creating an electron pocket in the π^*-band. The electronic DOS corresponding to donor-GICs is shown in the left panel of figure 2.16. In acceptor GICs the charge transfer from graphene layer to acceptor empties the top of the $\pi-$band, shifting the Fermi level down (right panel of figure 2.16). This creates a hole pocket in the $\pi-$band. The shifting of the Fermi level and the resulting carrier pockets around the Fermi energy make GICs metallic in contrast to the semimetallic unintercalated graphite.

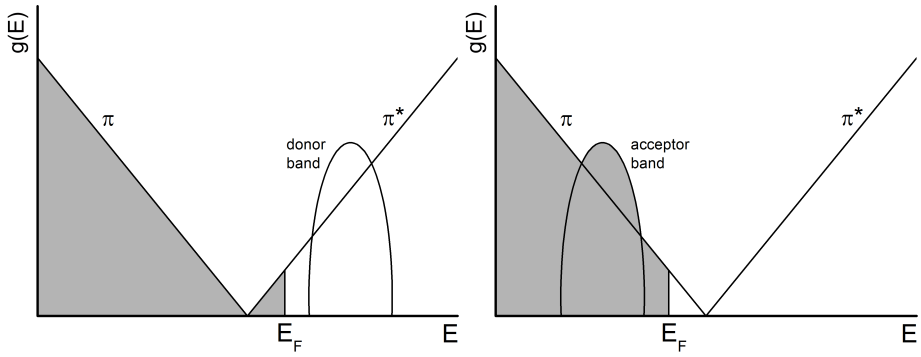

Figure 2.16: The electronic structures shown schematically of (left) donor-GICs and (right) acceptor GICs, where $g(E)$ is the DOS as a function of energy E and E_F is the Fermi energy. Filled states are shown in grey, empty states in white.

In GICs the intercalant species are accommodated between the graphene sheets in the same region as the graphitic interlayer band and, for donor species, contribute additional bands [72]. Where there is an overlap between the interlayer and the intercalate bands the hybridization of the two gives interlayer-intercalate bands. These bands have a free-electron-like, 3D nature and become occupied in donor-GICs with raised Fermi levels. Figure 2.17 shows the DFT calculated electronic band structure of the three donor-GICs

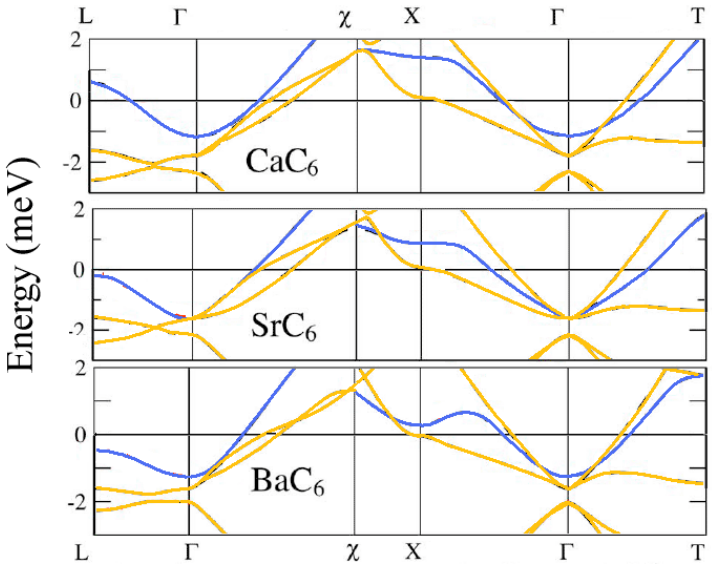

Figure 2.17: DFT calculated electronic band structures of $\mathrm{CaC_6}$, $\mathrm{SrC_6}$ and $\mathrm{BaC_6}$. The zero energy corresponds to the Fermi energy E_F. Bands are colour-coded as: graphite-π orange; interlayer-intercalate (free-electron-like) blue. Figure adapted from [11].

studied here: $\mathrm{CaC_6}$, $\mathrm{SrC_6}$ and $\mathrm{BaC_6}$.

The band structures clearly show the metallic nature of each GIC, seen by the upward shift of the Fermi level into the π^*-band, in contrast to its position between the $\pi-$ and π^*-bands in graphite (figure 2.10). In contrast to the simple rigid band model, in each case there are three bands which cross the Fermi level; two graphitic $\pi-$bands and a third interlayer-intercalate band. The degree of occupation of each band is similar in each material.

Chapter 3

Superconductivity and Charge Density Waves in MC_6 Graphite Intercalation Compounds

3.1 Abstract

The interaction of electrons and phonons is at the heart of many of the most interesting phenomena in condensed matter physics. States such as superconductivity and charge densty waves result directly from electron-phonon coupling in a wide variety of systems. In order to examine these phenomena it is necessary to study the electronic and vibrational properties of the systems where they exist.

Graphite intercalation compounds are one class of system which exhibits both of these phenomena. Many graphite intercalation compounds are superconductors at low temperatures, such as the MC_6 compounds CaC_6, YbC_6 and SrC_6 ($T_C = 11.5\,K$, $6.5\,K$ and $1.65\,K$ respectively). Another, BaC_6, has been predicted to superconduct at $230\,mK$, although recent magnetisation measurements have refuted this. In addition, CaC_6 has very recently been seen to exhibit a charge density wave at $78\,K$ with an onset temperature which is, as yet, unknown.

Measurements of the heat capacity of solids can provide considerable information about the electronic and vibrational properties of materials. Heat capacity measurements,

particularly when performed at low temperatures, directly probe the electronic energy levels and phonon states of a material and hence allow comparisons between theory and experiment. In addition they are sensitive to phase transitions such as those that signify the onset of superconducting and charge density wave states.

In this work heat capacity measurements have been performed from $300\,K$ down to $\sim 390\,mK$ in order to study the electronic and vibrational properties of CaC_6, SrC_6 and BaC_6 and their superconducting and charge density wave states. In CaC_6 study of the superconducting anomaly as a function of temperature and magnetic field has confirmed an intermediate-coupling ($\lambda_{el-ph} = 0.7$), BCS-like state with deviations suggested as due to a combination of moderate anisotropy and Fermi surface competition with the charge density wave state. At higher temperatures, up to a maximum of $300\,K$, the charge density wave onset transition has not been observed, indicating that the onset is above this temperature in line with other systems with similarly large charge density wave gaps.

For CaC_6, SrC_6 and BaC_6 low temperature heat capacity has been well described by a Debye model modified to include an additional low energy optical phonon mode. Both the Debye temperatures and the characteristic additional phonon temperatures have been found to decrease with increasing intercalant mass, as expected. The Sommerfeld electronic constant has been seen to decrease from CaC_6 to SrC_6 to BaC_6, yielding electron-phonon coupling values for CaC_6 and SrC_6 in agreement with predictions and that are consistent with known values of T_C. The electron-phonon coupling constant in BaC_6 has been found to be only a quarter of the predicted value, explaining the absence of superconducting effects at the predicted T_C in recent magnetisation measurements.

Measurements of the heat capacity of SrC_6 and BaC_6 at temperatures below $2\,K$ have detected previously unobserved features centered at $\sim 0.2\,K^2$ and $\sim 0.3\,K^2$, respectively. These features are well described by Schottky-like fits and have similarity with features exhibited by defective and polycrystalline graphites. The temperature range over which these features persist means that the region at which superconductivity has previously been observed in SrC_6 is obscured and makes any assessment of possible superconductivity in BaC_6 impossible. However, it is noted that the observed disparity between the measured and predicted values of the electron-phonon coupling constant in BaC_6 is such that the predicted T_C is likely to be inaccurate in any case.

3.2 Theory and Phenomena

3.2.1 Heat Capacity

[This section follows the description of heat capacity found in *Specific Heats at Low Temperatures* by *Gopal* [73]. Full derivations of the formulae included below are found therein].

The measurement of the heat capacity of solids can provide considerable information about the vibrational, electronic and magnetic properties of materials. Heat capacity measurements, particularly when taken at low temperatures, directly probe the electronic and magnetic energy levels of a material and hence allow comparisons between theory and experiment.

The heat capacity C describes the response of the temperature T of a material to a change in its internal energy U due to an influx of heat ∂Q, as:

$$C = \frac{\partial U}{\partial T} = \frac{\partial Q}{\partial T} \tag{3.1}$$

Using the second law of thermodynamics $dQ = TdS$, C can also be described in terms of entropy, as:

$$C = T\frac{\partial S}{\partial T} \tag{3.2}$$

C can be defined as the amount of heat required to raise the temperature of one mole of a substance by one degree Kelvin. This is the molar heat capacity C_n in units of $J/K/mol$.

C_n is a function of pressure, volume and temperature. Measurements can be made at constant pressure (C_P) or constant volume (C_V), with the latter typically used for gas and liquid samples. For solids C_P and C_V are effectively equal assuming negligible thermal expansion. As such, this work will discuss heat capacity only as $C = C_n$.

C of a substance is governed by the manner in which its internal energy is distributed amongst its constituents. The basic total heat capacity of a metallic crystal is a sum of the contributions from atomic vibrations about lattice sites, the motion of atoms within molecules and thermal excitation of conduction electrons (magnetic contributions can also arise but are not discussed here). These are the *lattice mode of thermal excitation*, *molecular modes* and *electronic contribution*, respectively.

At low temperatures the lattice and molecular (phonon) modes combine to give a T^3 relationship [74] for C and the electronic contribution is proportional to T [75], as:

$$C = \gamma T + \beta T^3 \tag{3.3}$$

where γ is the Sommerfeld constant; β is the lattice contribution coefficient. The coefficients γ and β are described by:

$$\gamma = \frac{\pi^2 N_A k_B^2}{2E_F} \tag{3.4}$$

$$\beta = \frac{12\pi^4 N_A k_B}{5\Theta_D^3} \tag{3.5}$$

where N_A is the Avogadro constant; k_B is the Boltzmann constant; E_F is the Fermi energy; Θ_D is the Debye temperature.

Θ_D is the temperature which corresponds to the highest occupied phonon mode of a material. It can equally be thought of as the temperature required to activate all the phonon modes of a crystal. A higher value of Θ_D therefore indicates higher energy phonon modes due, for example, to a lower atomic mass or stronger bonding.

At high temperatures C tends towards a constant value of $3k_B N_A/mol = 24.94\, J/K/mol$ (the Dulong-Petit law [76]).

As described above the relationship between heat and temperature is governed by the heat capacity. However, at a phase transition the heat capacity is not well defined. At a first-order transition the heat added or removed during a phase change does not change the temperature, making the heat capacity technically infinite at that point (equation 3.2). In second-order transitions the first derivative is continuous but the second derivative shows an infinity. In practice the heat capacity does not become infinite at a phase change but instead displays a cusp or discontinuous jump. The behaviour of the heat capacity at two second-order phase transitions, those of superconductivity and the charge density wave (CDW) state, is discussed in sections 3.2.2 and 3.2.3, respectively.

3.2.2 Superconductivity

[This section follows the description of superconducting phenomena found in *Introduction to Superconductivity* by *Tinkham* [12]. Full derivations of the formulae included below are found therein].

Superconductivity is defined by the coexistence of two phenomena, perfect conductivity and perfect diamagnetism: Below a critical temperature T_C the electrical resistance falls to zero [77] and any magnetic field is expelled [78].

Superconductors are classified as type I or type II based on their response to applied magnetic fields H. A magnetic field applied to a superconductor is screened by currents flowing in its surface which allow the field to penetrate only a short distance into the superconductor [79]. The magnetic field can be screened in this way up to a critical field. For a type I superconductor this critical field is H_C and for $H \geq H_C$ superconductivity is destroyed (left panel of figure 3.1). For a type II superconductor [80] at a field H_{C1} discrete lines of magnetic flux penetrate the superconductor and form a flux lattice with normal cores but superconductivity persists in this mixed state. Only at a field $H \geq H_{C2} > H_{C1}$ is superconductivity destroyed.

The right panel of figure 3.1 shows the behaviour of H_C as a function of temperature T for a type I superconductor - for type II superconductors $H_{C2}(T)$ is given by the Werthamer-Helfand-Hohenberg (WHH) equations [81] which describe a similar shape. Empirically $H_C(T)$ is seen to vary as:

$$H_C(T) \approx H_C(0) \left[1 - \left(\frac{T}{T_C} \right)^2 \right] \tag{3.6}$$

In layered superconductors $H_{C2}(T)$ has been observed to exhibit an extended linear dependence as an almost universal property [82].

Superconductivity occurs when normal electrons form pairs in the presence of an attractive potential, resulting in a condensate with an energy lower than that of the normal state. This formation of 'Cooper pairs' is described by the microscopic, mean-field BCS theory [83]:

In a superconductor at $T = 0$ all the Cooper pairs are in the ground state. This ground state is separated from the excited states by an energy gap $2\Delta_{SC}(T)$, as shown schematically in figure 3.2. The size of the gap at $T = 0$ is related to T_C by the equation:

$$\frac{2\Delta_{SC}(0)}{k_B T_C} = 3.528 \tag{3.7}$$

At $T > 0$ some Cooper pairs break apart and quasiparticles, which include both electron- and hole-like excitations, are generated. As T increases the quasiparticles

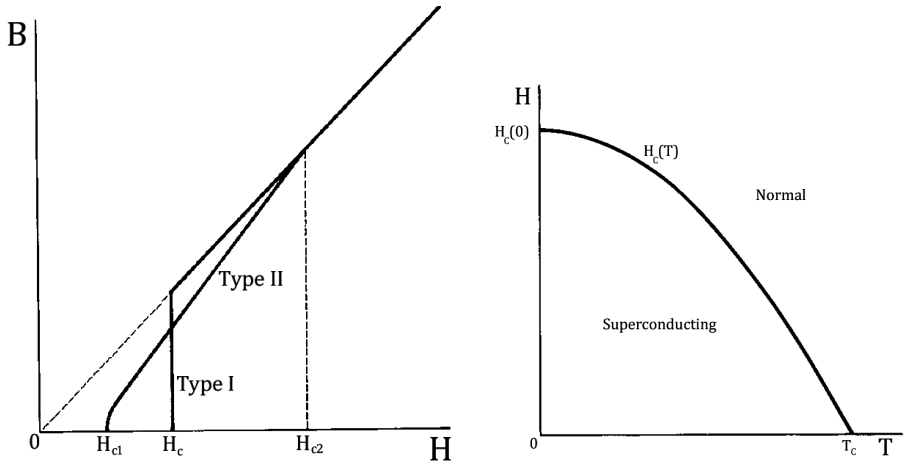

Figure 3.1: Left: Comparison of flux penetration behaviour of type I and type II superconductors. H_C is the critical field for a type I superconductor. H_{C1} and H_{C2} are the lower and upper critical fields for a type II superconductor. Right: Temperature dependence of the critical field H_C. Figures taken from [12].

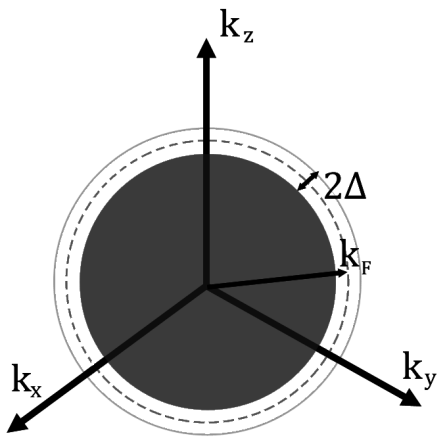

Figure 3.2: An isotropically gapped Fermi surface in a BCS superconductor at $T = 0$. The shaded region represents the occupied states of the superconducting electrons.

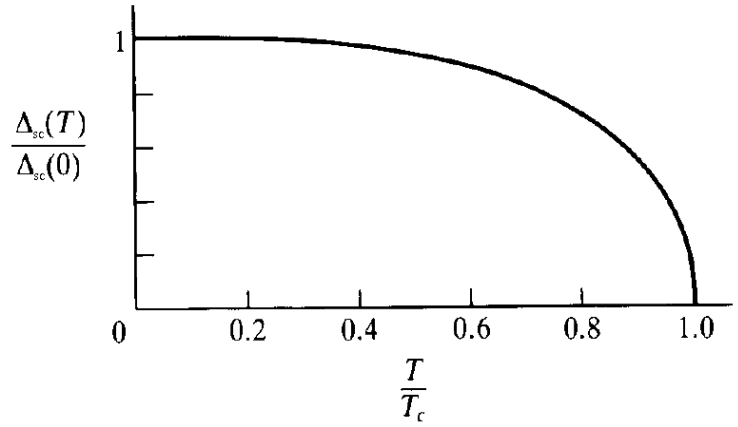

Figure 3.3: Temperature dependence of the energy gap in the BCS theory. Strictly speaking, the curve holds only in a weak-coupling limit, but it is a good approximation in most cases. Figure taken from [12].

are excited across the gap and there are fewer Cooper pairs in the superconducting ground state, so that $\Delta_{SC}(T) \rightarrow 0$ as $T \rightarrow T_C$. At T_C the number of Cooper pairs goes to zero and the material becomes normal. The temperature dependence of Δ_{SC} is shown in figure 3.3.

The attractive potential which joins the electrons in Cooper pairs can have various origins. In conventional superconductivity the attraction between electrons is due to interaction with phonons. Electrons with equal and opposite momenta and spin join to form the Cooper pairs below T_C, forming an isotropic energy gap in reciprocal space (as previously shown in figure 3.2). The net angular momentum of these pairs is 0, thus the superconducting state is the lowest in energy. This is conventional s-wave superconductivity.

In d-wave superconductivity electrons form into Cooper pairs in which the net angular momentum is not zero. This pairing yields an energy gap which is anisotropic and contains nodes in reciprocal space. The gap is not 'clean' as in the s-wave case but contains states, even in the superconducting phase. This type of pairing has been proposed as a potential mechanism for high-temperature superconductors [84].

BCS theory is very successful in accounting for the behaviour of superconductors where the electron-phonon interaction is weak. In this *weak-coupling* limit the electron-phonon coupling constant $\lambda_{el-ph} \ll 1$. Coupling is described as of *intermediate* strength when

$\lambda_{el-ph} \lesssim 1$, and *strong* when $\lambda_{el-ph} \gtrsim 1$. The Sommerfeld constant γ is related to λ_{el-ph} via the DOS at the Fermi level $g(E_F)$. This relationship allows λ_{el-ph} to be estimated using the equation:

$$(1 + \lambda_{el-ph}) = \frac{0.212\gamma}{g(E_F)} \tag{3.8}$$

where γ has units of $mJ/K^2/gat$; $g(E_F)$ has units of $states/eV/atom/spin$. Coupling strength can similarly be assessed using equation 3.7 such that superconductors with values of the ratio $\frac{2\Delta_{SC}(0)}{k_B T_C} < 3.528$ have weak-coupling, while those with greater values have strong-coupling.

Measurement of the heat capacity of a superconductor in both its normal and superconducting states can be used to characterise the nature of its superconductivity. For $T > T_C$ the heat capacity follows the Debye model, as detailed in section 3.2.1; the electronic contribution to the heat capacity in the normal state is C_{en} and is proportional to temperature:

$$C_{en} = \gamma T \tag{3.9}$$

For $T < T_C$ BCS theory predicts that the electronic contribution to the heat capacity C_{es} will depend exponentially on temperature as:

$$C_{es} \approx \gamma T_C a e^{-b\frac{T_C}{T}} \tag{3.10}$$

At T_C, therefore, there is a discontinuity in C_e, while the lattice heat capacity is assumed to be unaffected. Figure 3.4 shows the nature of the discontinuity ΔC and the exponential dependence below T_C. BCS theory predicts the size of the discontinuity to be:

$$\Delta C = 1.426 C_{en} \tag{3.11}$$

or equivalently, using equation 3.9:

$$\frac{\Delta C}{\gamma T_C} = 1.426 \tag{3.12}$$

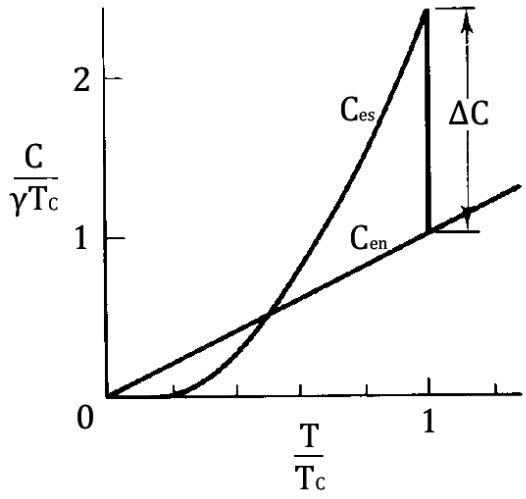

Figure 3.4: Heat capacity of a material at and below the BCS superconducting transition showing the discontinuous jump in heat capacity at T_C. Figure from [12].

3.2.3 Charge Density Waves

[This section follows the description of CDWs in the text *Density Waves in Solids* by *Grüner* [85]].

Density waves are broken-symmetry states of metals brought about by electron-phonon or electron-electron interactions. Their ground states are a coherent superposition of electron-hole pairs in which the charge density or spin density displays a periodic spatial variation. The former is a CDW [86, 87] and the latter a spin density wave (SDW) [88].

The CDW ground state is that of a coupled carrier-phonon system, similar to that of BCS superconductivity. The pairs here are formed by electrons and holes on opposite sides of the Fermi surface, with wavevectors $\pm k_F$. The resulting coupled states are separated from the normal states by an energy gap $2\Delta_{CDW}$.

CDWs are low-dimensional phenomena exhibited by quasi-1D (e.g. 1T-$TaSe_2$ [89], $K_{0.3}MoO_3$ [90]) and quasi-2D systems (e.g. the transition metal dichalcogenides 2H-$TaSe_2$, 2H-TaS_2, 2H-$NbSe_2$ and 2H-NbS_2 [91, for a review]). The purely 1D case is described by the Peierls theory [87] and, although not quantitatively accurate for the higher-dimensional cases, does give a good qualitative picture:

At $T = 0$ in a 1D metal in the absence of electron-electron or electron-phonon inter-

actions the ground state corresponds to the situation shown in the left panel of figure 3.5.

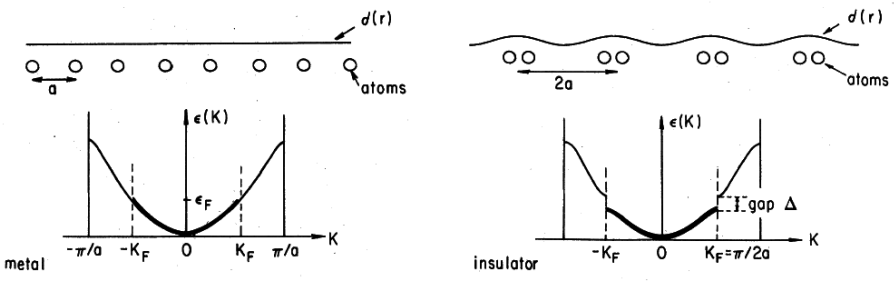

Figure 3.5: Peierls distortion in a 1D metal with a half-filled band: (left) undistorted metal; (right) Peierls insulator. $d(r)$ is the electronic density; a is the lattice constant. Figure taken from [13].

In the presence of an electron-phonon interaction it is energetically favourable to create a periodic lattice distortion (right panel of figure 3.5) with period x related to the Fermi wave vector by:

$$x = \frac{\pi}{k_F} \tag{3.13}$$

This distortion opens up a gap Δ_{CDW} at the Fermi level which modifies the dispersion relation as shown in the figure and lowers the electronic energy. In 1D Δ_{CDW} is proportional to the amplitude of the lattice distortion. The modification of the dispersion relation leads to a position-dependent electron density - the CDW - which locally neutralises the lattice distortion. If the ratio of the distortion period to the lattice constant is rational the CDW is called *commensurate* (CCDW) with the lattice, otherwise it is called *incommensurate* (ICDW). In some materials the transition from the normal state to an ICDW state is followed at lower temperatures by a further transition to a CCDW state (e.g. 2H-$TaSe_2$ [92]).

At $T > 0$ normal electrons are excited across the gap, causing screening of the electron-phonon interaction. This reduces both Δ_{CDW} [93] and the magnitude of the distortion leading to a second-order, 'Peierls transition' at a temperature T_P. The main features of the transition are described by mean-field theory in the same way as that of BCS superconductivity [94]. Consequently, the temperature dependence of the gap

$\Delta_{CDW}(T)$ has the same form as that of BCS superconductivity (figure 3.3) and it vanishes at the transition temperature:

$$\frac{2\Delta_{CDW}(0)}{k_B T_P} = 3.528 \tag{3.14}$$

In the form of a ratio of the gap size to the transition temperature equation 3.14 is used to compare CDW coupling strengths across different host systems [13]. Similarly to BCS superconductivity (equation 3.7), CDW coupling is termed *weak* if the ratio is less than 3.528 and *strong* if it is greater.

The mean-field treatment neglects the effects of thermodynamic fluctuations which for a strictly 1D system would prevent the CDW phase transition occurring above $T = 0$ [95]. In real, quasi-1D systems interchain coupling partially suppresses the effects of such fluctuations, allowing the Peierls transition to occur but at a lower temperature $T_{CDW} < T_P$.

In the 1D case at $T > T_{CDW}$ the material is a metal; at $T < T_{CDW}$ it is an insulator because the Fermi surface is fully gapped. In cases where gapping is incomplete the number of states around the Fermi level is depleted but does not fall to zero and the material remains conducting to some degree giving a metal-metal or metal-semiconductor transition.

The concept of 'nesting' of sections of the Fermi surface is useful in describing incomplete gapping. In systems whose Fermi surface topologies include large parallel faces spanned by a (nesting) vector there will be an instability toward the opening up of gaps on these faces only [96]. Where this is the case portions of the Fermi surface can host a CDW gap while other sections remain normal, giving partial gapping and a metallic CDW state below T_{CDW}.

The effect of an applied magnetic field H on the 1D CDW state is similar to that on a BCS superconductor, in that increasing fields weaken the pairing interaction and reduce the transition temperature. The field dependence of T_{CDW} is predicted [97, 98] by:

$$\frac{\Delta T_{CDW}}{T_{CDW}(0)} \approx -\frac{1}{4}\left(\frac{\mu_B H}{k_B T_{CDW}(0)}\right)^2 \tag{3.15}$$

where μ_B is the Bohr magneton.

The equation shows that very large fields are required in order to destroy a CDW state; e.g. the quasi-1D organic metal CDW system $(\mathrm{Per})_2 M(\mathrm{mnt})_2$ [99] has a relatively low $T_{CDW}(0) = 11.3\,K$ and this corresponds to a critical field of $\sim 37\,T$ [98].

A variety of experiments have been conducted on quasi-1D and quasi-2D materials with CDW states. The second order phase transition at the onset of the CDW state has been examined by measurements of various thermodynamic quantities such as heat capacity, thermal expansion and elastic constants, as well as electrical transport coefficients and structural measurements by x-ray and neutron diffraction [100, for a review].

As noted above, the equations of the 1D CDW state are of the same form as those of BCS superconductivity. Therefore, in measurements of the heat capacity the CDW phase transition leads to an equivalent anomoly in the heat capacity at the onset temperature. In the 1D case described above this transition occurs at T_P causing a heat capacity jump ΔC described [100] by:

$$\Delta C = 1.426\gamma T_P = \frac{\pi^2}{8.414} g(E_F) k_B^2 T_P \tag{3.16}$$

where $g(E_F)$ is the DOS at the Fermi level; k_B is the Boltzmann constant and γ is the Sommerfeld constant (c.f. equation 3.12 and figure 3.4 for the BCS equivalent).

The above equation assumes the participation of all states at the Fermi level, as indicated by the use of $g(E_F)$, resulting in complete gapping of the Fermi surface. In systems where partial gapping occurs the number of states participating in the CDW is less than $g(E_F)$ and ΔC is correspondingly smaller. As such $\Delta C(g(E_F))$ is treated as an upper limit on the size of the heat capacity jump.

Heat capacity measurements of the CDW transitions of the quasi-2D dichalcogenides 2H-$NbSe_2$, 2H-TaS_2 and 2H-$TaSe_2$ and quasi-1D $K_{0.3}MoO_3$ are shown in figures 3.6, 3.7, 3.8 and 3.9, respectively. In the figures transition shapes and widths are typical and are seen to vary in the range $\Delta T \sim 5 - 40\,K$. The magnitude of the excess contribution to the heat capacity at the transition ΔC varies widely between materials and across material classes. General behaviour is described by equations 3.10 and 3.12 while comparison between materials is made more simply by calculating the ratio of ΔC to the total heat capacity at T_{CDW} $\frac{\Delta C}{C(T_{CDW})}$. Table 3.1 presents electronic and vibrational parameters for several layered dichalcogenides with CDW states.

As is clear from table 3.1 transition into the CDW state generally occurs at high temperatures. From an experimental point of view a difficulty in analyzing such high-temperature features in heat capacity measurements is the substantial contribution from background thermal excitations which must be subtracted from the total. This is especially the case since the normal state is not easily attained by applying a magnetic field as for superconductors. To obtain ΔC for a CDW transition the following procedure is typically

Material	γ $(mJ/K^2/mol)$	β $(mJ/K^4/mol)$	$\Theta_D\ (K)$	$T_{CDW}\ (K)$		$\frac{2\Delta_{CDW}}{k_B T_{CDW}}$	$\frac{\Delta C}{C(T_{CDW})}(\%)$
2H-$NbSe_2$	16.0	0.55	222	N $\rightarrow$ ICDW	33.5	23.9	6.5
2H-TaS_2	7.5	0.44	236	N $\rightarrow$ ICDW	78.0	15.4	4.5
2H-$TaSe_2$	4.5	0.71	202	N $\rightarrow$ ICDW	121	15.2	22
				ICDW $\rightarrow$ CCDW	90	–	< 0.1

Table 3.1: CDW transitions in the layered dichalcogenides. N $\rightarrow$ ICDW signifies a transition from the normal state to the incommensurate CDW state. CCDW $\rightarrow$ ICDW signifies a transition from the commensurate CDW state to the incommensurate CDW state. Data taken from [14]; column 6 from [45].

followed [15]: First, a polynomial fit is made to the surrounding background heat capacity by masking the transition region during fitting. Subtraction of this fit then yields an estimate for the excess heat capacity ΔC associated with CDW formation.

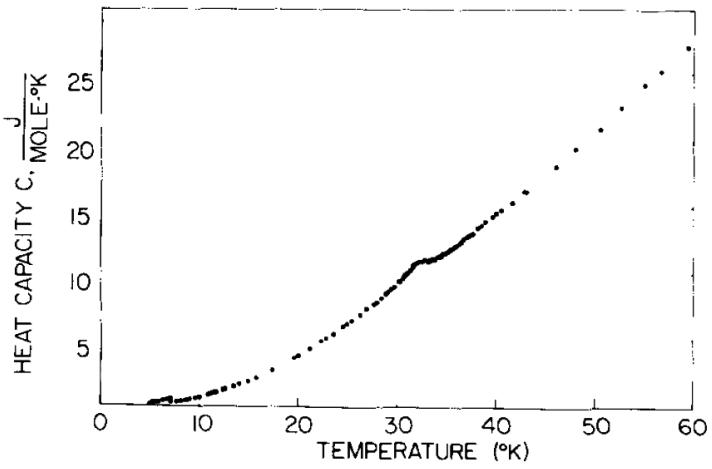

Figure 3.6: Heat capacity of 2H-$NbSe_2$ showing the CDW transition at $T_{CDW} = 33\,K$. The superconducting transition is seen at $7\,K$. Figure adapted from [14].

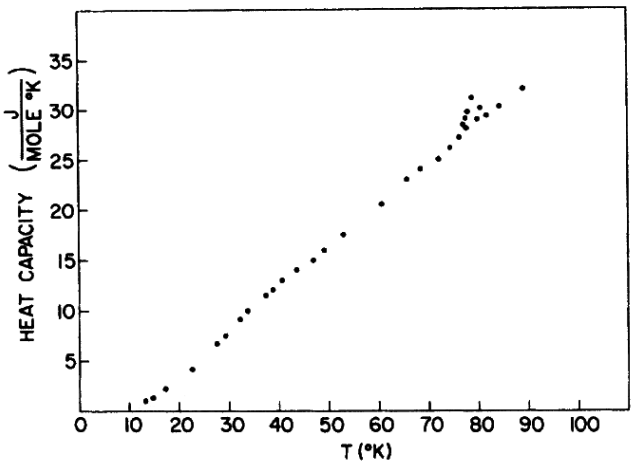

Figure 3.7: Heat capacity of 2H-TaS_2 showing the CDW transition at $T_{CDW} = 78\,K$. Figure adapted from [14].

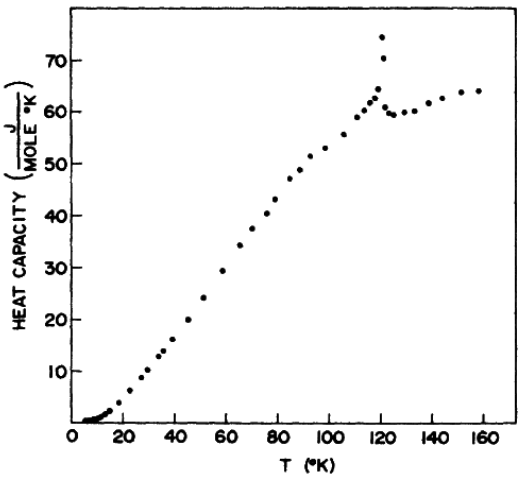

Figure 3.8: Heat capacity of 2H-$TaSe_2$ showing the CDW transitions at $T_{CDW} = 121\,K$ and $90\,K$ for the ICDW and CCDWs, respectively. Figure adapted from [14].

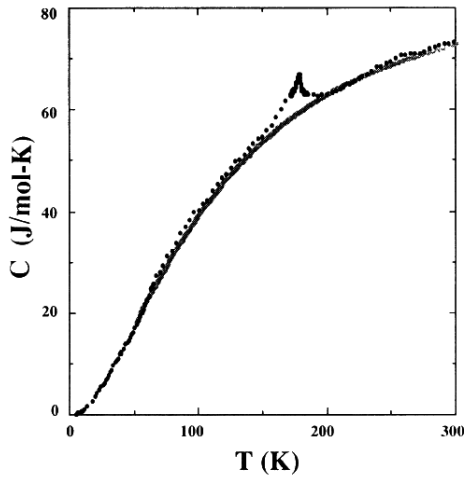

Figure 3.9: Temperature dependence of the heat capacity of $K_{0.3}MoO_3$ (blue bronze). The CDW transition is clear at $T_{CDW} = 180\,K$. The solid line is a polynomial fit through the background of the heat capacity data. Figure adapted from [15].

3.2.4 Competition between Superconductivity and CDWs

Some systems exhibit both superconducting and CDW states; a recent review by Gabovich [101] extensively documented the superconducting and CDW properties of many such systems including the layered dichalcogenides, A15 and C15 structured materials and high T_C oxides (the review contains a table which details the superconducting and CDW parameters of some 40 compounds). Both superconducting and CDW states arise from carrier pairing via electron-phonon coupling and both exhibit gapping of the Fermi surface. As a result, in materials where they coexist the superconducting and CDW states conflict [102]. These mutual effects have been observed in a number of ways; as the exclusion of the nested portions of the Fermi surface from participating in superconductivity in $NbSe_2$ [103] and the high-T_C oxides [104, 105]; in Cu_xTiSe_2 competition between CDW and superconducting states has been observed by the suppression of the CDW by tuning the amount of Cu [106]; while in the organic conductor $(Per)_2[Au(mnt)_2]$ a similar suppression of the CDW state under pressure has shown an emergent superconducting state [107].

The Gabovich model [102] predicts thermodynamic properties in the case of an s-wave BCS superconductor with a CDW, where $T_C \ll T_{CDW}$. In the combined superconducting-CDW state it defines the Fermi surface gapping as:

$$D(T) = \left[\Delta_{SC}^2(T) + \Delta_{CDW}^2(T)\right]^{\frac{1}{2}} \tag{3.17}$$

This is the combined gap appearing on the nested Fermi surface sections. The remaining (unnested) sections are defined solely by the superconducting order parameter $\Delta_{SC}(T)$. Each of the gaps has the BCS form. In the superconducting-CDW state both the $T = 0$ superconducting energy gap $\Delta_{SC}(0)$ and CDW energy gap $\Delta_{CDW}(0)$ are reduced compared to the lone case i.e. the CDW inhibits superconductivity and vice versa. Figure 3.10 shows the reductions of $\Delta_{SC}(T)$ and $\Delta_{CDW}(T)$ resulting from the presence of CDW gapping of a proportion μ of the Fermi surface compared to the BCS case.

Since the BCS character of the gap dependences for the CDW s-wave superconductor is preserved the temperature dependence of both the CDW and superconducting heat capacity anomalies is unaltered from the situation described in sections 3.2.2 and 3.2.3, when $T_C \ll T_{CDW}$. In the case where $T_C \approx T_{CDW}$ the heat capacity anomalies are more complex and are described further in [102].

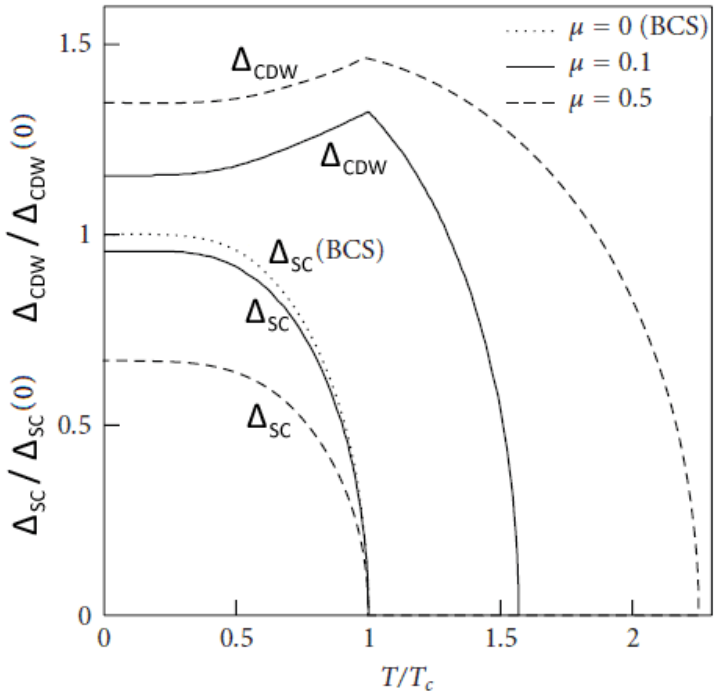

Figure 3.10: Temperature dependences of the superconducting (Δ_{SC}) and CDW (Δ_{CDW}) order parameters for different values of the parameter μ, the portion of the Fermi surface where the CDW gap develops. Figure taken from [16].

3.3 Introduction and Experimental Motivation

3.3.1 Superconductivity in GICs - The Study of CaC_6

Superconductivity has been observed in more than 20 donor-GICs - it has not been seen in any acceptor GICs. Table 3.2 lists the T_C of the superconducting group I, II and III donor-GICs and their discovering references.

GIC	$T_C\ (K)$	Reference
RbC_8	0.026	Hannay 1965 [51]; Kobayashi 1985 [108]
KC_8	0.15	Hannay 1965 [51]; Koike 1980 [109]
KC_6	1.5	Avdeev 1986 [110]
SrC_6	1.65	Kim 2007 [22]
$Li_3C_6{}^*$	1.9	Belash 1989 [111]
$Na_3C_6{}^*$	5	Belash 1987 [112]
$K_2C_8{}^*$	5.5	Avdeev 1986 [110]
$Cs_2C_8{}^*$	6	Avdeev 1990 [113]
YbC_6	6.5	Weller 2005 [52]
CaC_6	11.5	Weller 2005 [52]

Table 3.2: Superconducting group I, II and III donor-GICs, their transition temperatures and discovering references. *Metastable compound formed under high pressure.

Superconductivity has been known in alkali-metal GICs from the first experiments in 1965 [51] but since the discovery of superconducting CaC_6 and YbC_6 in 2005 [52] interest in the mechanism underlying the superconducting GICs has been rejuvenated. With the highest T_C CaC_6 has been the main focus of both theoretical and experimental work.

Immediately following the discovery of superconductivity in CaC_6 and YbC_6 a novel pairing mechanism involving excitons and acoustic plasmons was proposed as explanation by Csanyi [53]. This was suggested due to an empirical observation that superconductivity coincides with electronic occupation of the interlayer band in GICs. This explanation was subsequently criticised in a paper by Mazin [114] in which a more conventional picture was proposed of Cooper pairing via electron-phonon coupling. Based on the BCS isotope effect the different electron-phonon coupling contributions were predicted as $85\,\%$ from coupling to intercalant phonons and $15\,\%$ from coupling to graphitic phonons.

DFT calculations by Calandra proposed to make a complete description of the electron-phonon coupling mechanism in CaC_6 [10]. This was done by calculating electronic structure and phonon structure as well as electron-phonon coupling constants for Ca and graphitic phonons. Their findings were contrary to those of Mazin in that the electron-phonon coupling contributions were calculated to be approximately equal between Ca and graphitic phonons with $\alpha_{Ca} = 0.24$ and $\alpha_{graphitic} = 0.26$ (summing to the BCS value of 0.5). They concluded that the primary electron-phonon coupling results from the Ca-derived part of the Fermi surface interacting with out-of-plane graphitic phonons and in-plane Ca phonons, and estimated the total electron-phonon coupling constant $\lambda_{el-ph} = 0.83$. Similar electronic and phonon structures were subsequently used in another theoretical work which described well the experimentally observed increase in T_C with pressure [115].

The first measurements of the Ca isotope effect in CaC_6 were made by Hinks [116], who found a significant effect suggesting that Ca phonons are heavily involved in the superconducting mechanism. The Ca isotope effect was found to be 0.53, greater than the BCS value of 0.5. Given this result the natural conclusion is that if the superconductivity is BCS-like there must be virtually no electron-phonon coupling with the graphitic phonons, contrary to the DFT picture. Other explanations include potential magnetic sample impurities; or that the total isotope effect is significantly greater than 0.5 as is the case for some high temperature superconductors [117]. The latter of these explanations is supported by tunneling measurements [118] which find a large superconducting gap of $2.3\,meV$ which corresponds to a value of $\frac{2\Delta_{SC}}{k_B T_C} \sim 4.6$, putting CaC_6 well into the strong-coupling regime. However, this value is disputed by scanning tunneling microscopy (STM) measurements which find a gap of only $1.6\,meV$ [20].

Recent work by Yang [119] has resolved theπ^* and interlayer bands in CaC_6 with new clarity and elaborated upon the nature of the coupling underlying superconductivity. ARPES measurements found that a superconducting gap opens on both the π^* and interlayer bands and that the π^*-interlayer interaction contributes $> 50\,\%$ to the total electron-phonon coupling strength. Additionally, Yang et al found evidence of coupling between the C_z phonon modes and both the π^* and interlayer bands, but no interaction between the C_{xy} modes and the interlayer band, in agreement with [10, 18]. Ca_{xy} modes could not be resolved.

The first measurement of the heat capacity of the superconducting phase of CaC_6 was made by Kim in 2006 [17]. The samples tested, created using an HOPG base intercalated by the Li-Ca alloy method [44], were estimated to contain approximately $5\,\%$ impurities but the superconducting anomaly was still clearly observed. Measurements

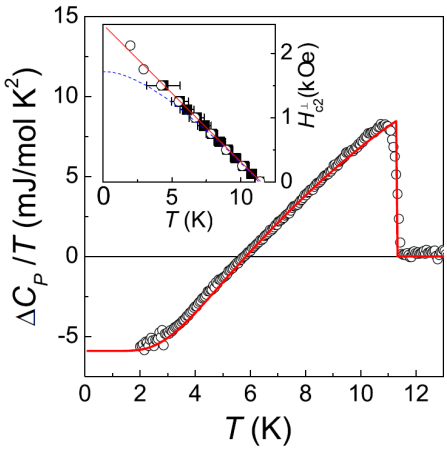

Figure 3.11: Temperature dependence of $\frac{\Delta C_P}{T} = \frac{C_P(H=0)}{T} - \frac{C_P(H=10\,kOe)}{T}$ for CaC_6. The red solid line is the best fit according to a scaled isotropic s-wave BCS model. Inset: $H_{C2}(T)$ for $H \parallel c$ estimated from heat capacity (filled squares) and susceptibility (open circles) measurements. The blue dashed line demonstrates the WHH prediction and the red solid line is a linear fit for the low magnetic field data ($H < 1\,kOe$). Figure adapted from [17].

in the normal state found a Debye temperature of $593\,K$. Measurements of the superconducting anomaly are shown in figure 3.11 as $\frac{\Delta C}{T} = \frac{(C_s - C_n)}{T}$, the heat capacity difference between the superconducting and normal states. Applying a scaled isotropic s-wave fit the heat capacity jump at T_C was found to be $\frac{\Delta C}{\gamma T_C} = 1.432$, close to the weak limit BCS value of 1.426. Measurements of $T_C(H \parallel c)$ found a linear dependence (figure 3.11 inset) characteristic of layered superconductors and $H_{C2} = 2.48\,kOe$. Linear behaviour of the Sommerfeld constant $\gamma(H)$ at low fields was interpreted as being consistent with an isotropic gap, while the exponential temperature dependence of C_{es} showed the absence of gap nodes. The electron-phonon coupling constant was estimated at $\lambda_{el-ph} = 0.70$, in reasonable agreement with the prediction of Calandra. Taken together this suggests that CaC_6 has a fully gapped, isotropic superconducting order parameter and fits within the intermediate coupling BCS approach.

A 2007 paper entitled 'Unresolved problems in superconductivity of CaC_6' [19] clearly laid out the findings, agreements and contradictions outlined above. With respect to the heat capacity a significant difference was noted between experimental data and the values calculated using the electronic and vibrational structures of Boeri [115]. As shown in figure 3.12 both the magnitude of the superconducting heat capacity anomaly

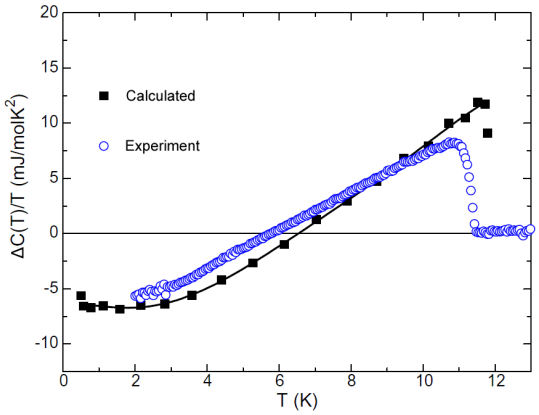

Figure 3.12: Deviation of the calculated (Boeri [18]) strong-coupling heat capacity from experimental results (Kim [17]) for CaC_6. Figure taken from [19].

as predicted by Boeri and its temperature dependence differ markedly from experiment.

Two possible explanations appear for the disagreement. Firstly, sample impurities noted by Kim could play a role, meaning a confirmation of Kim's findings is desirable in order to discern whether the inconsistency is on the side of the experimental work. Secondly, the theoretical predictions may be inaccurate because the model assumes an isotropic superconducting gap, whereas the gap could be to some degree anisotropic as suggested by ARPES measurements which show anisotropic coupling of the graphitic Fermi surface and phonons [120]. Indeed the fit to the Kim data does show more curvature than is evident in the data implying a possible lack of suitability of the isotropic s-wave BCS model.

Work by Sanna [21] has attempted to resolve the problem of the heat capacity disagreement by performing calculations assuming a 'moderately anisotropic gap' rather than an isotropic one. This approach, while contradicting the linear $\gamma(H)$ observed by Kim, does improve agreement with the experimentally found $\frac{\Delta C}{T}$, though the detailed temperature dependence remains poorly described (left panel of figure 3.13). Sanna also used this model to predict a corroborating superconducting gap shape as measured by scanning tunnelling spectroscopy (STS) but no better agreement is achieved for the anisotropic case than for the isotropic (right panel of figure 3.13), leaving the question of the degree of gap anisotropy unresolved.

In addition to the theoretical and experimental work done on CaC_6 other alkali earth-metal GICs have been tested to provide a better picture of the field as a whole. In

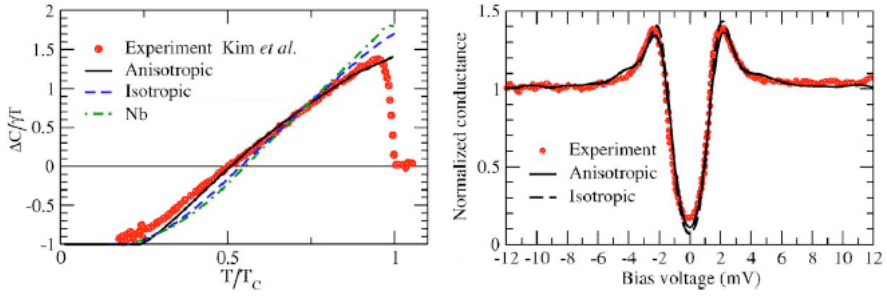

Figure 3.13: Left: Comparison of the reduced heat capacity of CaC_6 as measured by Kim [17] to isotropic and moderately anisotropic gap models. Right: Experimental normalized conductance [20] compared to isotropic and anisotropic gap predictions. Figure adapted from [21].

2007 measurements of the magnetisation and heat capacity of SrC_6 showed it to superconduct with $T_C = 1.65\,K$ [22], showing order of magnitude agreement with the Calandra DFT predicted value of $T_C = 3.1\,K$ [11]. ΔC was found to be less than the BCS value close to T_C and greater than BCS at lower temperatures (figure 3.14) indicating an anisotropic gap, a conclusion supported by anisotropy in the upper critical field (although $\frac{\Delta C}{\gamma T_C}$ is calculated confusion arises in the paper as to its value). This conclusion was extended to suggest that gap anisotropy in CaC_6 is greater than originally suggested as well as being greater than in SrC_6, lending support to the case for the importance of investigations into an anisotropic gap in CaC_6.

In this work fresh measurements of the superconducting heat capacity anomaly of CaC_6 are presented such that previous measurements of its magnitude and temperature dependence can be verified and compared with theoretical models. Furthermore this and previous data is analysed in the context of the recent finding of a CDW state at $78\,K$ (detailed in section 3.3.3).

3.3.2 Prediction of Superconductivity in BaC_6

Attempts to further understand the superconducting mechanism in CaC_6 have been aided by studying the relationship between different physical parameters and superconductivity. Figure 3.15 shows that the graphitic interlayer separation d_c correlates well with T_C, showing an exponential-like decrease of T_C with increasing interlayer separation across a number of GICs. This observation is also consistent with the measured increase of T_C with increasing pressure, a process which decreases interlayer sepa-

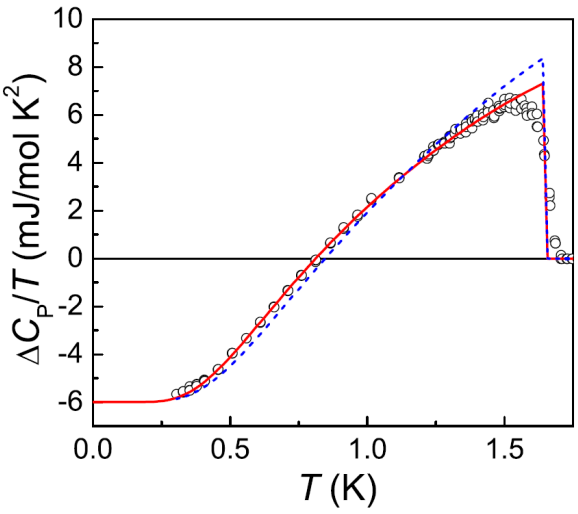

Figure 3.14: Temperature dependence of $\frac{\Delta C_P}{T} = \frac{C_P(H=0)}{T} - \frac{C_P(H=500\,Oe)}{T}$ for SrC_6. The red solid line is the best fit according to a scaled isotropic s-wave BCS model. The blue dashed line represents the BCS curve. Figure taken from [22].

ration, in CaC_6 [115] and a smaller effect in YbC_6 [121]. The mechanism for this is suggested to be as follows: a decrease in the interlayer spacing promotes an inter-band interaction between the graphitic π and interlayer parts of the Fermi surface which intersect, which increases the amount of electron-phonon coupling possible [22, 18].

The emprical relationship between T_C and d_c, and application of the rigid band model lead Csanyi to suggest BaC_6 as a possible superconductor in his 2005 paper. Although contradicting Csanyi's proposed coupling mechanism, Calandra also suggested BaC_6 to be superconducting, predicting a T_C of $0.23\,K$ [11].

Recently several experiments have been performed on samples of BaC_6 with the aim of comparing the superconducting T_C, if found, with the predicted value. Each experiment has measured the temperature dependence of the magnetic susceptibility of mm-sized samples of vapour-phase, Madagascan natural graphite-based BaC_6. To date no measurements of the heat capacity of BaC_6 have been published.

In 2007 Kim found no signature of superconductivity in a BaC_6 sample down to $300\,mK$ [22], and in 2008 Nakamae extended that conclusion down to $80\,mK$ [24]. Figure 3.16 shows the field-cooled magnetisation results of Nakamae at low fields, with no signs of the diamagnetic transition characteristic of superconductivity. In 2010 Heguri performed the same measurement still lower in temperature and found no superconducting

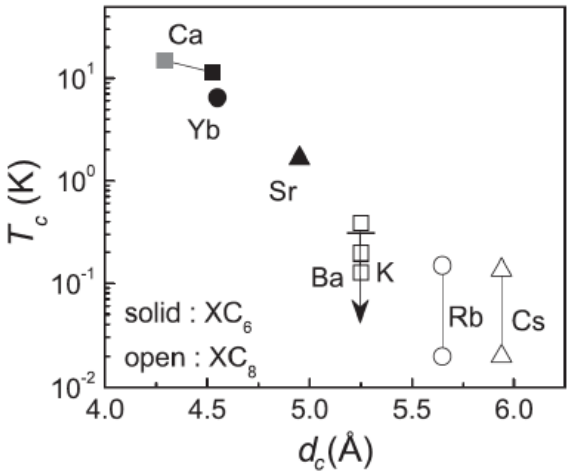

Figure 3.15: T_C as a function of interlayer spacing for CaC_6, YbC_6, SrC_6, BaC_6, KC_8, RbC_8 and CsC_8. For CaC_6 T_C at a pressure of $8\,GPa$ is also plotted in grey. An upper limit for BaC_6 of $T_C = 0.3\,K$ is labelled with an arrow [22], although this upper limit has been subsequently superseded (now $0.06\,K$ [23]). Figure taken from [22].

signature down to $60\,mK$ [23].

Two possible explanations arise for this apparent disagreement between the theoretical and experimental results. The first is based on the findings of [9] showing the DFT underestimation of the BaC_6 low energy phonons suggests that the predicted T_C may be erroneous. If this is the case BaC_6 may have a significantly reduced T_C, or it may not be superconducting at all. The second is based on the complexity of the cryogenic set-up required for achieving sub-$300\,mK$ temperatures with respect to sample reactivity and thermalisation. To meet these constraints the Nakamae experiment attached the BaC_6 sample with Apiezon H grease (a high temperature grease intended for use above $-10\,^{\circ}C$) to the inside of a quartz capsule which was sealed under a weak helium pressure. This capsule was thermally connected to the cold head-thermometer assembly by copper whiskers wrapped around the capsule and fixed with a small amount of silicon-based grease. Given the extremely low temperatures, the number of thermal boundaries and the low thermal conductivity of the quartz capsule at these temperatures, it is reasonable to ask whether complete thermalisation was achieved - i.e. whether the temperatures relayed from the thermometer attached to the cryostat cold head were the same as those at the sample. For the results of Heguri it is not possible to assess the experimental setup as no details are given.

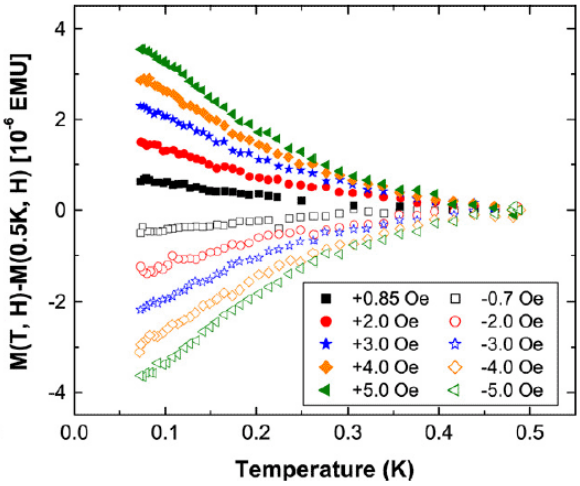

Figure 3.16: Field-cooled magnetisation M as a function of temperature at constant applied magnetic fields indicated in the legend. No superconducting transition is seen at any field. Figure taken from [24].

The above outlined disagreement between the theoretical predictions and experimental results requires further experimental work for several reasons: (i) BaC_6 has been predicted as superconducting by models which have described very similar GICs well but to date experimental studies have found no evidence of this; (ii) to this point only the magnetisation of BaC_6 has been studied for signs of superconductivity and other sensitive methods, such as heat capacity measurement, could well provide further detail; (iii) given the uncertainties discussed above about some of the experimental techniques employed to this point it seems sensible to perform verifying measurements. This thesis aims to provide these experiments, and thus clarify the situation with respect to any superconducting nature in BaC_6.

3.3.3 Evidence of a Charge Density Wave in CaC_6

Recently, STM and STS measurements have observed a CDW state in CaC_6. These experiments were performed by K.C. Rahnejat at University College London. The paper detailing these findings and supporting work is currently in review. It is referenced here as [25].

The observation of a CDW state in CaC_6 was unexpected but is not entirely unsurprising

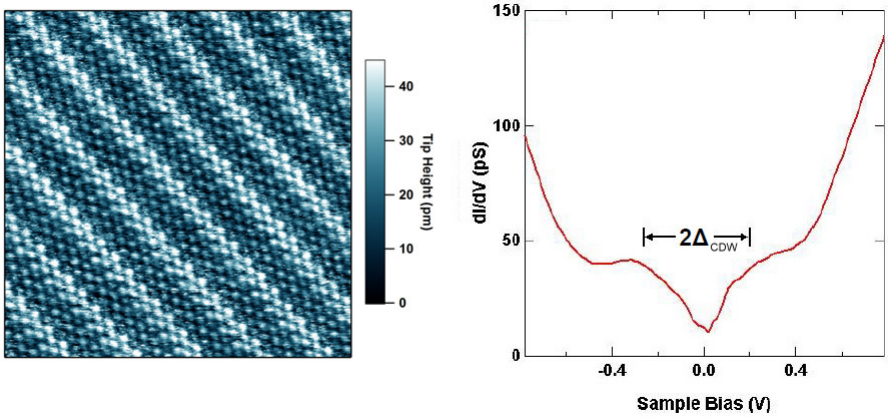

Figure 3.17: Left: Constant current STM image of a CaC_6 surface recorded at $78\,K$, $+400\,mV$ showing atomic resolution with a superimposed one-dimensional, $1.125\,nm$ period stripe. Right: Conductance spectroscopy showing the CDW gap with $2\Delta_{CDW} \approx 475\,meV$. Figures provided by K.C. Rahnejat, University College London [25].

given that other similarly layered compounds exhibit both superconducting and CDW states, including the transition-metal dichalcogenides [122, 123, 45], metal-containing organic compounds [124] and cuprate high-temperature superconductors [125]. The recent work observed a modulation across CaC_6 surfaces at $78\,K$, in addition to an associated gap of $2\Delta_{CDW} \approx 475\,meV$ in the electronic DOS at the Fermi level. The left panel of figure 3.17 shows an STM scan of a CaC_6 surface showing this modulation, identified in the work as a 1D CDW. The right panel shows STS measurements of the CDW gap.

STM imaging measured the hexagonal graphite lattice in CaC_6 as having $a_0 = 2.50\,\mathring{A}$, and the Ca superlattice $3a_0 = 4.33\,\mathring{A}$, as expected. The periodicity of the CDW was measured as $1.125\,nm$, identifying it as commensurate with both the graphite and Ca lattices. STM imaging further showed a transverse distortion of $0.6\,\mathring{A}$ of the Ca lattice conincident with the stripe but no measurable distortion of the graphite lattice. It was also noted that a graphene terminated surface was required for the CDW to be imaged. Together these observations imply that the CDW involves only the electrons in the graphene planes with no distortion of the carbon atoms, while the Ca atoms between planes are displaced.

The CDW gap was measured by STS current imaging tunneling spectroscopy (CITS) which yields a position-dependent conductivity map of the surface. The Fourier transform of this map was used to deconvolve the contributions to the gap of the graphite

and Ca lattices and the stripe, and found strong association of the gap with the stripe. The large gap size of $2\Delta_{CDW} \approx 475\,meV$ indicates a significant modification of the Fermi surface, although zero bias conductivity is non-zero showing that CaC_6 remains metallic in the CDW state.

As detailed, the results of [25] provide strong evidence for the existence of a CDW state in CaC_6. Such an observation is of particular interest in CaC_6 as a superconductor because the relationship between superconductivity and CDWs is not yet fully understood. To date, no measurements of heat capacity of CaC_6 have been published above $\sim 20\,K$, as all interest to this point has focused on the superconducting transition at $11.5\,K$. The STM/STS measurements of [25] showing the CDW were made at $78\,K$, thus the CDW onset temperature must be above this point. Therefore, in order to characterise the CaC_6 CDW high resolution measurements of properties sensitive to CDW formation, such as heat capacity, are required. This thesis aims to provide these measurements.

3.4 Experimental Details

3.4.1 Sample Creation by Intercalation

The intercalated graphite samples measured in this thesis were prepared by Dr Chris Howard of University College London using previously published methods. Therefore, only brief descriptions of the fabrication methods are presented, along with basic sample characterisation used to assess the sample quality.

Table 3.3 presents an overview of the intercalation methods used to form the CaC_6, SrC_6 and BaC_6 samples tested here. Representative x-ray diffraction patterns of each material are shown in figure 3.18. These patterns were used to assess sample quality by identifying the phases present in each sample and calculating peak height ratios of the desired phase to any other phases present. The results of this diffraction study are shown in table 3.4. In CaC_6 and BaC_6 samples quality is seen to be high with purity percentages of $100\,\%$ in both cases (i.e. no other phases were detected). In scans of SrC_6 it was also the case that no undesired phases were detected, however the small sample size and contribution from the Kapton tape securing the sample to the diffractometer combined to give a background with variation approximately $5\,\%$ of the [004] peak height, meaning sample purity can be stated only as $> 95\,\%$.

Material	Method	Temp ($^\circ C$)	Press. ($mbar$)	Time
CaC_6	Li:Ca alloy in 3:1 ratio & outgassed HOPG graphite [44]	350	$\sim 1\text{x}10^{-6}$	10 days
SrC_6	One-zone vapour transport with excess Sr metal & outgassed Madagascan natural graphite [65]	465	$\sim 1\text{x}10^{-6}$	4 weeks
BaC_6	One-zone vapour transport with excess Ba metal & outgassed Madagascan natural graphite	500	$\sim 1\text{x}10^{-6}$	4 weeks

Table 3.3: Overview of the intercalation methods used.

GIC	Graphite base	Appearance	Purity from XRD (%)
CaC_6	HOPG	Silvery; metallic	100
SrC_6	Madagascan natural graphite	Silvery; metallic	$\gtrsim 95$
BaC_6	Madagascan natural graphite	Silvery; metallic	100

Table 3.4: GIC sample quality assessment from x-ray diffraction patterns shown in figure 3.18.

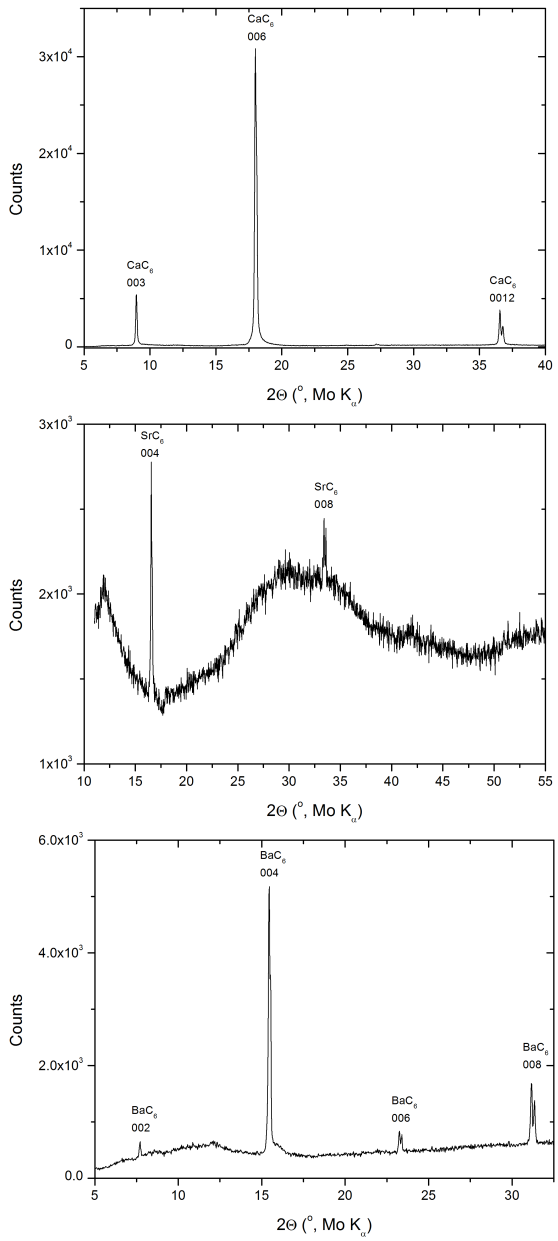

Figure 3.18: 2Θ x-ray diffraction patterns for samples of CaC_6, and SrC_6 and BaC_6 from the same batches as those tested below. Sample purities as detailed in table 3.4 calculated by ratios of peak heights taking local backgrounds. SrC_6 background variation is due to small sample size and Kapton tape used to secure the sample in the diffractometer.

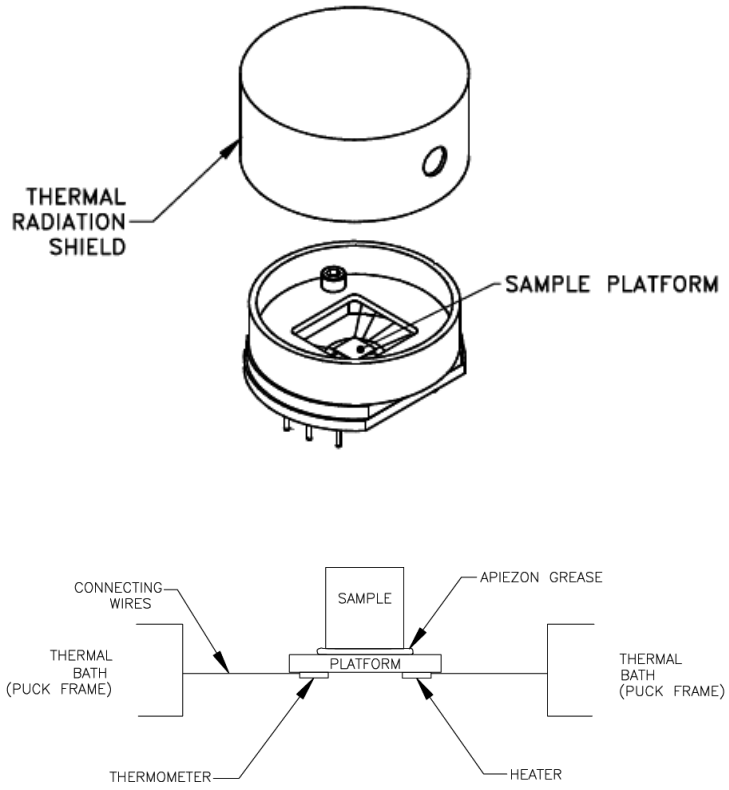

Figure 3.19: Schematic representation of the sample environment in the Quantum Design PPMS. Figures taken from the PPMS documentation supplied by Quantum Design.

3.4.2 Heat Capacity Measurement Setup

Measurements of the heat capacity of samples presented in this thesis were performed using Quantum Design Physical Properties Measurement Systems (PPMS) at University College London and Warwick University. With the standard probe (figure 3.19) heat capacity measurements were performed from a maximum of $300\,K$ down to $2\,K$. Measurements made between $2\,K$ and $350\,mK$ utilised a Quantum Design low temperature ^{3}He probe. The systems are fitted with superconducting magnets capable of producing fields above H_{C2} in all cases, directed along the graphitic c-axis ($H \parallel c$).

The measurement technique employed by the PPMS is the two-tau relaxation method [126, and PPMS documentation available from Quantum Design]. Each measurement cycle consists of a heating period followed by a cooling period during which the entire

temperature response of the sample platform is fitted to a model that accounts for both the thermal relaxation of the sample platform and the sample itself.

The measurement of the heat capacity of each sample consists of two stages. In the first stage the heat capacity of the sample holder and a minute amount of Apiezon N grease on the platform is measured over the required temperature range. This is the 'addenda' measurement. The sample is then secured to the grease on the platform and the measurement run again over the same temperature range to give a 'total' measurement. The heat capacity of the sample is then calculated by subtracting the addenda from the total.

The magnitude of the uncertainty in each measurement is dependent upon the mass of the sample through the relative sizes of the sample and addenda contributions. This is an important effect for some of the samples measured here. Samples of several milligrams of CaC_6 can be readily formed using the Li:Ca alloy method with HOPG [44] but sample masses are necessarily smaller ($\leq 0.5\,mg$) for Madagascan natural graphite-based SrC_6 and BaC_6. As such the absolute heat capacity values presented here are accurate to within $\pm 2\,\%/5\,\%/6\,\%$ for $5 \leq T \leq 300\,K$ and $\pm 3\,\%/14\,\%/6\,\%$ for $T \leq 5\,K$ for CaC_6/SrC_6/BaC_6, respectively.

A well recognised difficulty in the interpretation of heat capacity measurements at high temperatures is the sizable background and correspondingly large noise in the data [15]. Given the observation of the CDW in CaC_6 at $78\,K$ (i.e. $T_{CDW} \gtrsim 78\,K$) and the possible small feature size, this was foreseen as an issue. In order to reduce this noise to a minimum and yield a high resolution measurement the heat capacity was recorded in steps of $0.5\,K$ over the entire temperature range with two averaged datapoints per temperature setpoint. As heat capacity is a slow measurement at high temperatures a single $H = 0\,Oe$ run from $2\,K$ to $300\,K$ took over a week - given this timescale the corresponding addenda measurement was recorded with high temperature steps of $10\,K$.

Due to the air and moisture reactivity of alkali earth-metal GICs significant care was taken in preparing samples for the heat capacity measurements. Samples were prepared for and loaded into the PPMS cryostat as follows: In an argon filled glovebox (max $O_2 < 0.1\,ppm$, $H_2O < 0.1\,ppm$) samples were cleaved, cut and shaved flat with razor blades under a binocular microscope. Resulting samples were a maximum of $\sim 3\,mm$ x $\sim 3\,mm$, smaller than the heat capacity sample platform, and had clean, flat surfaces to ensure good thermal contact. The samples were sealed in an airtight travel case for transport to the PPMS and, subsequently, opened inside a helium filled glovebag

containing a binocular microscope and the puck mounting apparatus. Included in the travel case was a $\sim 5\,mm$ sized piece of Li metal which was used as a rough indicator of the purity of the transport and glovebag environment. The Li did not lose its metallic shine, indicating that oxidation of the samples was unlikely to have taken place. Each sample was seated on a minute amount of Apiezon N vacuum grease on the platform. The puck cap was attached and the assembly then loaded onto the end of the required probe. For CaC_6 samples the probe was then removed from the glovebag and inserted rapidly into the bore of the cryostat where the sample space was quickly purged and evacuated several times. The total exposure to air was less than 5 seconds from the beginning to the end of this process. For the more reactive SrC_6 and BaC_6 samples the probe end was sealed in a helium atmosphere during transfer from the glovebag to the PPMS. This atmosphere was broken only in the flowing ^{4}He gas of the cryostat and the probe loaded immediately.

3.5 Results

3.5.1 CaC_6 - Heat Capacity Measurements

Figure 3.20 shows a plot of the heat capacity of a CaC_6 sample as a function of temperature between $300\,K$ and $2\,K$. The overall shape of the $C(T)$ curve is that described by the Debye model, with a steep low temperature rise tending to a high temperature constant value. The inset in figure 3.20 of the same heat capacity measurement between $12\,K$ and $2\,K$ clearly shows the superconducting transition with onset at $T_C = 11.5\,K$ (centre at $11.3\,K$).

Figure 3.21 shows measurements of the heat capacity of a CaC_6 sample at low temperatures as a function of applied magnetic field, showing the zero field superconducting transition at $11.5\,K$ and its suppression in applied fields up to $10\,kOe$.

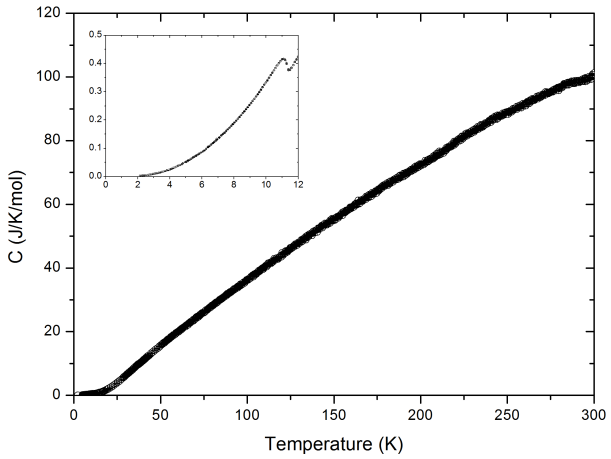

Figure 3.20: Heat capacity as a function of temperature for CaC_6 from $300\,K$ to $2\,K$ at zero magnetic field. Error bars are smaller than datapoints at all temperatures. Inset: The superconducting transition onset is at $11.5\,K$.

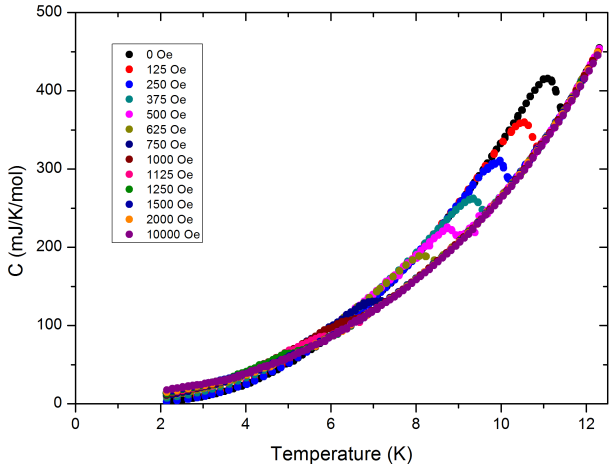

Figure 3.21: Heat capacity of CaC_6 as a function of temperature between $12.5\,K$ and $2\,K$ showing the superconducting transition in zero magnetic field and its suppression in applied fields up to $10\,kOe$. Error bars are smaller than datapoints at all temperatures.

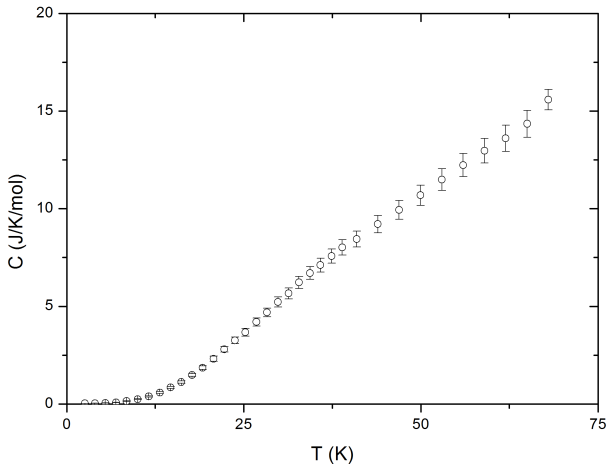

Figure 3.22: Heat capacity as a function of temperature for SrC_6 between $75\,K$ and $2\,K$ in zero magnetic field.

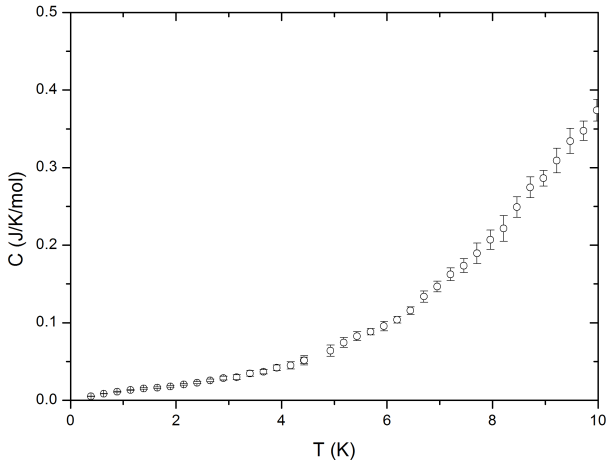

Figure 3.23: Heat capacity as a function of temperature for SrC_6 from $10\,K$ to $0.386\,K$ in zero magnetic field.

3.5.2 SrC_6 - Heat Capacity Measurements

Figure 3.22 shows a plot of the heat capacity of an SrC_6 sample as a function of temperature between $75\,K$ and $2\,K$ showing similar behaviour to CaC_6, with an additional slight hump seen at $\sim 40\,K$.

Figure 3.23 shows a plot of the low temperature heat capacity of an SrC_6 sample between $14\,K$ and $0.386\,K$. Unexpectedly the superconducting anomaly previously observed at $T_C = 1.65\,K$ [22] is not seen.

3.5.3 BaC_6 - Heat Capacity Measurements

Figure 3.24 shows a plot of the high temperature heat capacity of a BaC_6 sample as a function of temperature between $150\,K$ and $2\,K$ showing similar behaviour to CaC_6 and SrC_6.

Figure 3.25 shows a plot of the low temperature heat capacity of a BaC_6 sample between $10\,K$ and $0.386\,K$.

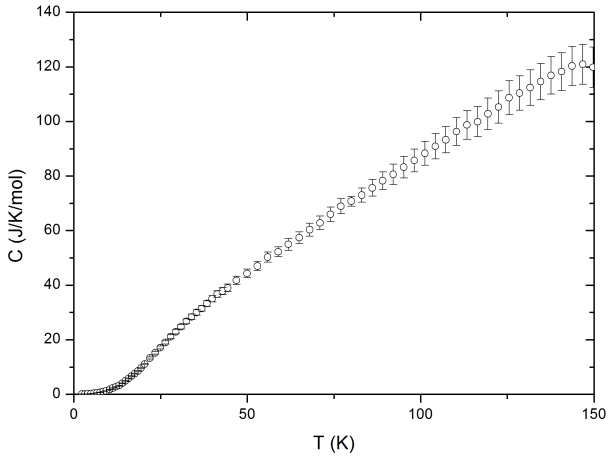

Figure 3.24: Heat capacity as a function of temperature for BaC_6 from $150\,K$ to $2\,K$ in zero magnetic field.

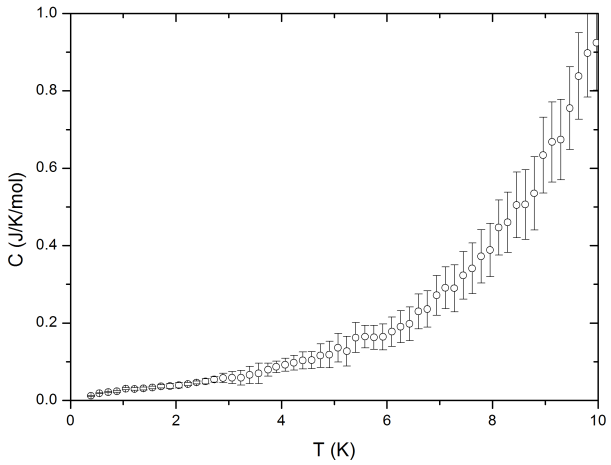

Figure 3.25: Heat capacity as a function of temperature for BaC_6 from $10\,K$ to $0.386\,K$ in zero magnetic field.

3.6 Discussion

3.6.1 Low Temperature Heat Capacity of MC_6 GICs

In the low temperature limit ($T \ll \Theta_D$) the Debye heat capacity relation (equation 3.3) is expressed as:

$$C = \gamma T + \beta T^3$$

Previous measurements of the low temperature heat capacity of GICs have shown deviation from this Debye description, with $C(T)$ showing slightly steeper curvature. Studies of KC_8, RbC_8 [127] and CsC_8 [128] showed that this deviation was due to the contribution of a dispersionless optical phonon mode of the intercalant and could be fitted using an Einstein mode. (Recent studies of CaC_6 [17] and SrC_6 [22] fitted instead an empirical T^5 term but still employed the same explanation.) From [127] this additional contribution to the heat capacity C_{Int} is:

$$C_{Int} = A\left(\frac{\delta}{T}\right)^2 \exp\left(\frac{-\delta}{T}\right) \tag{3.18}$$

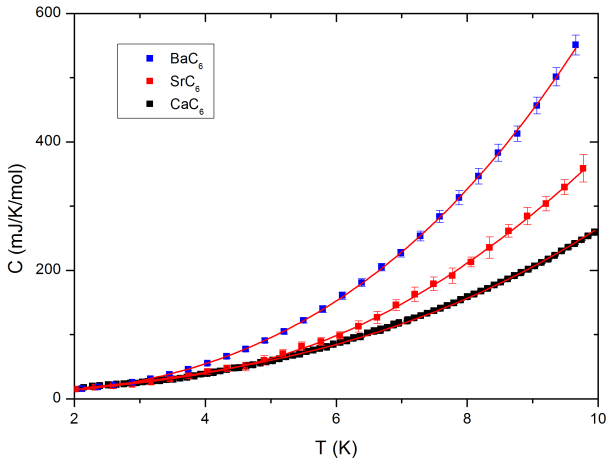

Figure 3.26: Low temperature heat capacities of CaC_6, SrC_6 and BaC_6 as a function of temperature. The red lines are fits to the function described by equation 3.19 with parameters given in table 3.5.

Material	γ $(mJ/K^2/mol)$	β $(mJ/K^4/mol)$	Θ_D (K)	δ (K)	A
CaC_6	7.12 ± 0.06	0.1943 ± 0.0009	412 ± 2	$-$	$-$
SrC_6	6.4 ± 0.2	0.211 ± 0.002	402 ± 4	45 ± 1	0.054 ± 0.007
BaC_6	4.2 ± 0.4	0.54 ± 0.01	293 ± 5	24 ± 4	0.004 ± 0.002

Table 3.5: Table of fit coefficients for curve shown in figure 3.26. Θ_D value calculated from β using equation 3.5.

where $A = \left(\frac{N}{N_A}\right) f$ is a coefficient relating to the degree of participation $(\frac{N}{N_A})$ and dimensionality (f) of the vibration; δ is the characteristic temperature. Following on from these studies the low temperature heat capacities of CaC_6, SrC_6 and BaC_6 have been interpreted by fitting the following function:

$$C = \gamma T + \beta T^3 + A \left(\frac{\delta}{T}\right)^2 \exp\left(\frac{-\delta}{T}\right) \tag{3.19}$$

Figure 3.26 shows the resulting curves and table 3.5 details the fit coefficients. Each of γ, β, δ and A is discussed in turn in the following section with comparison made to previously measured values where available.

The values of γ found in this work (presented in table 3.5) are seen to decrease from

Material	$\gamma\ (mJ/K^2/mol)$	$\Theta_D\ (K)$	Reference
Mad. natural / Spectro. Powder / HOPG	$0.0138/0.03/0.0173$	$413/421/427$	van der Hoeven 1963 [129] / Mizutani 1978 [128] / GA 1980 [130]*
LiC_6	3.0	$590-710$	Delhaes 1976 [131]
KC_8	$0.697/0.75$	$235/374$	Mizutani 1978 [128] / GA 1980 [130]*
RbC_8	$0.646/1.15$	$362/439$	Suganuma 1981 [127] / GA 1980 [130]*
CsC_8	$0.63/0.45$	$341/397$	Mizutani 1978 [128] / GA 1980 [130]*
CaC_6	$6.66/7.12$	$593/412$	Kim 2006 [17] / This work
SrC_6	$5.92/6.4$	$414/401$	Kim 2007 [22] / This work
BaC_6	4.2	293	This work

Table 3.6: Table of Sommerfeld constants γ and Debye temperatures Θ_D of graphites and alkali-metal GICs. *Grayson-Alexander 1980

CaC_6 to SrC_6 to BaC_6. Table 3.6 shows that the values obtained for CaC_6 and SrC_6 are in agreement with previous measurements, while BaC_6 has not previously been measured.

Recent Raman scattering work on alkali earth-metal GICs [68] found softening of the C_z phonons with decreasing interlayer distance d_c. This was suggested as due to increased filling of the $\pi^* -$band with decreasing d_c, as π^* is an antibonding band whose occupation acts to destabilise the in-plane bonds. γ is proportional to the DOS at the Fermi level (equation 3.8), which is positioned in the $\pi^* -$band in donor-GICs (figure 2.17). Therefore, the observation made here of decreasing γ from CaC_6 to SrC_6 to BaC_6 (i.e. with increasing d_c) supports the argument and findings of the previous work.

The obtained values of γ can be used to calculate an estimate for the electron-phonon coupling strength λ_{el-ph} through its relationship with the electronic DOS at the Fermi level. This relationship can be expressed as (equation 3.8):

$$(1 + \lambda_{el-ph}) = \frac{0.212\gamma}{g(E_F)}$$

where λ_{el-ph} is the electron-phonon coupling constant; γ is the Sommerfeld coefficient $(mJ/K^2/gat)$; $g(E_F)$ is the electronic DOS at the Fermi level $(states/eV/atom/spin)$.

Results of this calculation are presented in table 3.7 alongside the predicted values of Boeri [18]. Agreement between the experimental and calculated values of λ_{el-ph} is good for CaC_6 and SrC_6. However, in the case of BaC_6 the experimental λ_{el-ph} is found to be substantially smaller than the calculated value. This discrepancy has been explained by recent experimental work [9] which has given cause to doubt the predicted

GIC	γ $(mJ/K^2/mol)$	$g(E_F)$ $(states/eV/$C spin$)$ [a]	Experimental λ_{el-ph}	Calculated λ_{el-ph} [a]
CaC_6	7.12	0.13	0.7	0.83
SrC_6	6.4	0.14	0.4	0.54
BaC_6	4.2	0.12	0.1	0.38

Table 3.7: Values of the electron-phonon coupling λ_{el-ph} as estimated from the experimental Sommerfeld constant γ and theoretical electronic DOS at the Fermi level $g(E_F)$. [a] Data taken from [11].

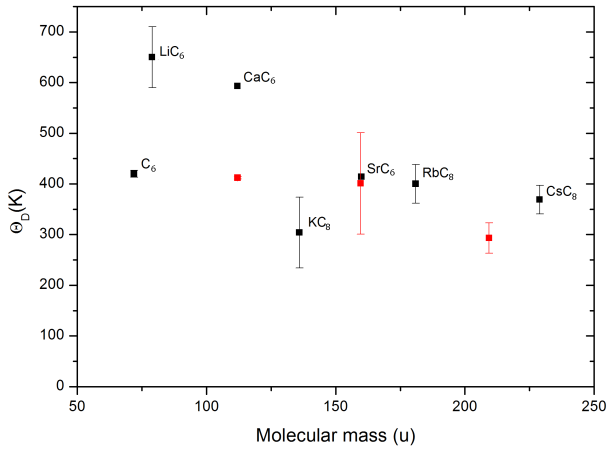

Figure 3.27: Debye temperature Θ_D as a function of molecular mass for (red) CaC_6, SrC_6 and BaC_6 (left to right) as measured here. Red error bars are experimental uncertainty. Other points (black) are average values from other studies as detailed in table 3.6. Black error bars demonstrate the upper and lower limits of previously measured values.

value of λ_{el-ph} and, therefore, of T_C in BaC_6; the work measured the low energy phonons of CaC_6 and BaC_6 by inelastic x-ray scattering as a function of temperature. In the case of superconducting CaC_6 the phonons observed showed reasonable agreement with those predicted by theory. However, for BaC_6 the phonon energies were observed at significantly higher (up to $20\,\%$) energies than predicted signifying that the theoretical phonon model for BaC_6 is incorrect. The resulting overestimate of λ_{el-ph} produces estimates of T_C in BaC_6 which are also likely to overestimate, explaining the absence of superconductivity in previous measurements at the predicted temperature.

The fitted values of β given in table 3.5 yield Debye temperatures which decrease with increasing molecular mass from CaC_6 to SrC_6 to BaC_6 as expected, at a rate of approximately $-1.2\,Ku^{-1}$. Figure 3.27 shows this trend clearly in a plot of Θ_D as a function of molecular mass (red points). Values of Θ_D found by previous studies are also shown in the figure (black points) and detailed in table 3.6.

Overall the values measured here of Θ_D are in good agreement with measurements for other alkali-metal GICs as shown in table 3.6, fitting the trend of decreasing Θ_D with increasing molecular mass. However, Θ_D for CaC_6 as measured here is noticably lower than the previously measured value. On the face of it this is a perplexing outcome given that the graphite-base in both cases is HOPG and the preparation procedures are very

Group I GIC	$\delta\,(K)$	Group II GIC	$\delta\,(K)$
KC_8	$-$ [128]	CaC_6	$-$
RbC_8	71 [127]	SrC_6	45
CsC_8	48 [128]	BaC_6	24

Table 3.8: Values of δ for group I and group II GICs.

similar. However, it was noted in the previous work that tested samples contained $\sim 5\,\%$ impurities, likely to be Li inclusions arising from the Li-Ca alloy used in intercalation. If these inclusions formed areas of LiC_6 within test samples the higher energy of the LiC_6 phonons would likely increase the measured Θ_D. An alternative possibility is that the prior value is affected by a reduced value of β caused by the additional fitting of the empirical T^5 factor in the heat capacity.

The parameter δ is the characteristic temperature of the optical phonon mode of the intercalant, as described by Suganuma [127], which provides an additional heat capacity C_{Int} in some GICs. It is dependent upon the type of intercalant atom rather than the graphite layers. In the case of CsC_8 $\delta = 48\,K$ and for RbC_8 $\delta = 71\,K$. For KC_8 the low temperature Debye model is followed well indicating a still higher value of δ and clarifying the trend of increasing δ with decreasing atomic mass. LiC_6 as a very light GIC also shows no low temperature C_{Int} [132].

The values of δ obtained here for the group II GICs CaC_6, SrC_6 and BaC_6 as presented in table 3.5 are repeated in table 3.8 alongside those of the group I GICs KC_8, RbC_8 and CsC_8 for comparison.

Table 3.8 shows that the trend of decreasing δ with increasing molecular mass shown by the group I GICs is also followed by the group II GICs as measured here. This effect is clear both within and across periods. As with KC_8, CaC_6 shows no appreciable contribution from the mode to the low temperature heat capacity because of its elevated value of δ. The values of $\delta = 45\,K$ and $24\,K$ equate to characteristic energies of $4\,meV$ and $2\,meV$ for SrC_6 and BaC_6, respectively. Comparison to the calculated phonon dispersion shown earlier for CaC_6 in figure 2.14 shows approximate agreement with the lowest energy modes calculated as resulting from intercalant motion.

The fitted values of the parameter A are given in table 3.5. $A = \left(\frac{N}{N_A}\right) f$ where f describes the number of degrees of freedom of the vibration and $\frac{N}{N_A}$ describes the proportion of atoms which participate. Clearly it is not possible here to obtain values for both f and $\frac{N}{N_A}$, however, assuming f takes a similar value to that suggested in [127]

of $f \sim 2$ (i.e. intercalant atoms vibrate parallel to the ab-plane but are hindered along the c-axis) values of $\frac{N}{N_A}$ of $\sim 2.5\%$ and $\sim 0.2\%$ are obtained for SrC_6 and BaC_6, respectively. These are small proportions of the intercalant atoms in each GIC and suggest that the observed modes correspond to areas of the tested samples which have a less complete intercalation. This in turn suggests that these modes are not intrinsic to GICs with the stoichiometry MC_6 due to their higher intercalant concentrations. In both cases this finding of small poorly intercalated volume is consistent with the assessment from x-ray diffraction of sample purity.

3.6.2 Very Low Temperature Effects in SrC_6 and BaC_6

Measurements of the heat capacity of SrC_6 and BaC_6 to temperatures below $2\,K$ have shown an unexpected and previously unobserved low temperature feature (CaC_6 was not measured). This is seen clearly in figures 3.28 and 3.29 where heat capacity is plotted as $\frac{C}{T}$ as a function of T^2, with fits described below - plotted in this way a heat capacity with simple electronic and lattice components is linear, with slope β and y-intercept γ. The observed shape is not that of a superconducting transition and, indeed, it obscures the region in which the superconducting anomaly already proven for SrC_6 would be expected ($T_C^2 = 2.72\,K^2$ [22]). In SrC_6 the peak arises below $\sim 6\,K^2$ with a center at $\sim 0.2\,K^2$, while for BaC_6 it arises below $\sim 10\,K^2$ with a center at $\sim 0.3\,K^2$.

The observed low temperature rise in the heat capacity is clearly common to both materials, and is suggested by the lowest temperature points in the BaC_6 plot to be an asymmetric peak shape. This additional contribution appears superimposed on the expected low temperature linear Debye behaviour (previously fitted additional modes become evident only above $25\,K^2$ and have been excluded from these plots for clarity).

The shape of the additional contribution is well described by the equation of a Schottky anomaly [73] as:

$$C_{Sch} = R\left(\frac{\delta}{k_B T}\right)^2 \frac{g_0}{g_1} \exp\left(\frac{\delta}{k_B T}\right)\left[1 + \left(\frac{g_0}{g_1}\right)\exp\left(\frac{\delta}{k_B T}\right)\right]^{-2} \tag{3.20}$$

where R is the molar gas constant; δ is the characteristic energy; $\frac{g_0}{g_1}$ is the degeneracy ratio.

The red lines shown in figures 3.28 and 3.29 are fits to the equation:

$$C = \gamma T + \beta T^3 + C_{Sch} \tag{3.21}$$

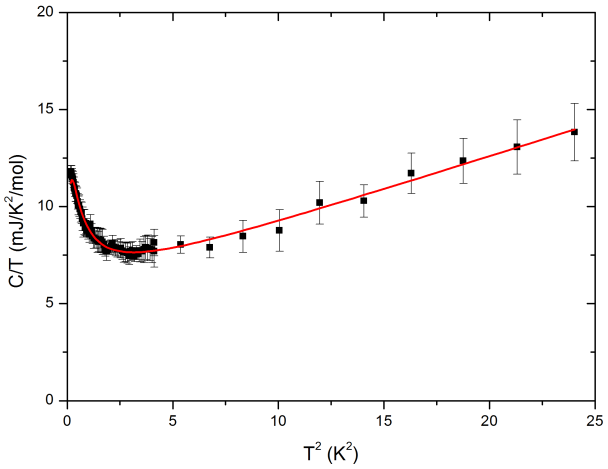

Figure 3.28: Very low temperature measurements of the heat capacity of SrC_6 plotted as $\frac{C}{T}$ as a function of T^2 showing a Schottky-like anomaly below $6\ K^2$. The red line is a fit to equation 3.21 with parameters given in table 3.9.

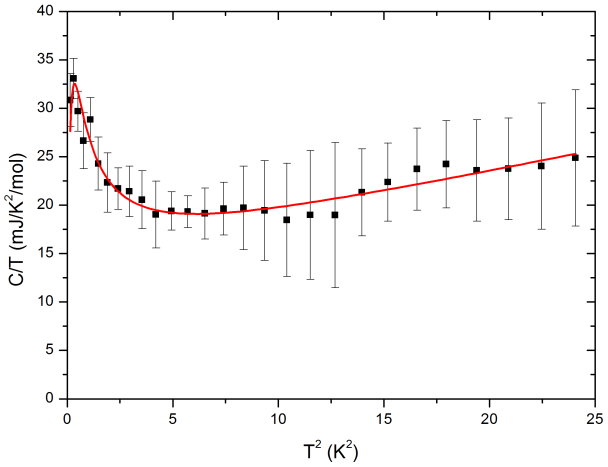

Figure 3.29: Very low temperature measurements of the heat capacity of BaC_6 plotted as $\frac{C}{T}$ as a function of T^2 showing a Schottky-like anomaly below $10\ K^2$. The red line is a fit to equation 3.21 with parameters given in table 3.9.

GIC	γ $(mJ/K^2/mol)$	$\beta(J/K^4/mol)$	$\delta(meV)$	$\frac{g_0}{g_1}$
SrC_6	5.6 ± 0.1	3.46 ± 0.06x10^{-4}	0.123 ± 0.006	1370 ± 50
BaC_6	14 ± 1	4.6 ± 0.5x10^{-4}	0.15 ± 0.02	340 ± 50

Table 3.9: Table of coefficients to fits to equation 3.21 for curves shown in figures 3.28 and 3.29.

The fit parameters are given in table 3.9. The fitted values of γ and β for SrC_6 are in approximate agreement with those found at higher temperatures in section 3.6.1, while for BaC_6 the fitted values differ substantially. This disagreement is thought due to the low mass of the BaC_6 sample and the relatively few data points available. In the context of a Schottky model the fitted values of $\frac{g_0}{g_1}$ for both compounds at 1370 ± 50 and 340 ± 50 are unusually large and suggest that strict application of this model is inappropriate. Instead other approaches are investigated.

Given the similarity of the features exhibited in terms of onset temperature and temperature dependence the origin of this effect seems likely to be common between SrC_6 and BaC_6. As this is the first published measurement of the heat capacity of BaC_6 no direct comparison can be made against other results, while one previous measurement of SrC_6 has been made [22], but it did not show the low temperature feature measured here.

It is interesting to compare the heat capacity anomalies observed above with similar features seen in poorly graphitised and defective graphites. In these systems a series of heat capacity anomalies are exhibited which are remarkably similar to those shown in figures 3.28 and 3.29 - a review by Mrozowski [26] documents these features in a variety of carbons and graphites of varying degrees of graphitisation. Figure 3.30 shows one such heat capacity anomaly in a polycrystalline graphite. The features are explained to arise in these systems as the result of the antiferromagnetic ordering of electron spins localised at defect centers, with the defect source and type being largely unimportant with respect to the exhibited behaviour. In the present systems of SrC_6 and BaC_6 it can be postulated that the defect centers which allow this behaviour to be exhibited are present in interior areas of the samples which remain unintercalated, or are perhaps due to the damage caused to the host graphite by the intercalation process itself. It has previously been suggested that the microstructure of the host graphite has important consequences for the measurement of materials properties [9] and the line of reasoning given here supports this suggestion in that the sole SrC_6 sample whose

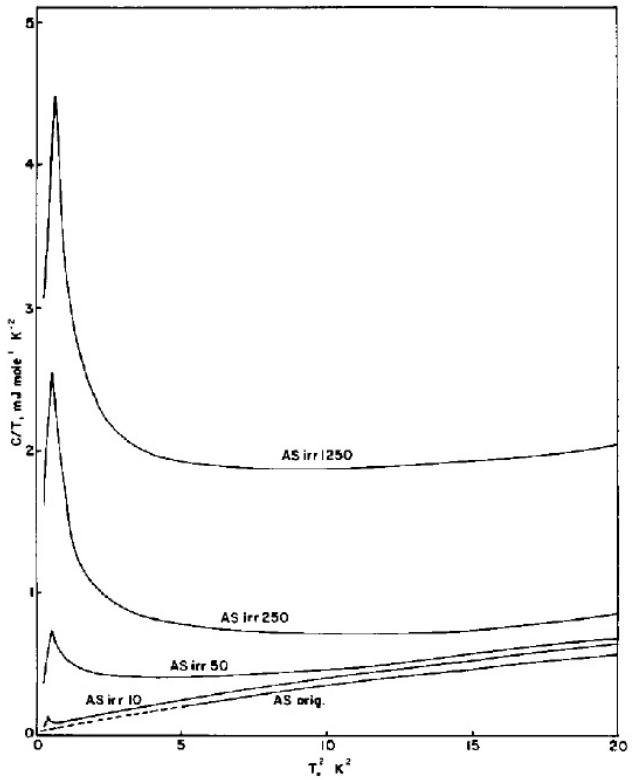

Figure 3.30: Heat capacity of an Airco-Speer chlorine-purified polycrystalline graphite (AS) neutron irradiated to various doses. Figure taken from [26]

heat capacity has been measured at these temperatures had an HOPG base and did not exhibit the effects seen here in natural flake based samples. A similar comparison cannot be made in the case of BaC_6 as there are no previously published heat capacity measurements. However, it is worth noting that previous measurements of the magnetisation of Madagascan natural graphite-based BaC_6 showed only a paramagnetic signal at temperatures below $1\ K$ with no additional features [24].

In order to rule out measurement problems the two types of artefact previously observed in measurements of the heat capacity in the very low temperature range are described below (documentation of these effects using the present system is available from Quantum Design). Firstly, below $\sim 10\ K$ it is possible for helium to condense onto the sample, the platform and its suspension wires resulting in a broad peak in the heat capacity in the range $3-5\ K$. Given the linear dependence evident over $9-25\ K^2$ range in fig-

ures 3.28 and 3.29 this effect is seen not to be responsible for the observed behaviour. Secondly, at temperatures below $\sim 1\,K$, too short a measurement duration with respect to the total time-constant can cause heat capacity to appear to decrease more rapidly than expected with decreasing temperature, due to increased thermal boundary resistance at low temperatures. This effect manifests as a dip in $\frac{C}{T}$ as a function of T^2 below $0.5\,K^2$ and is therefore not the source of the pronounced rise in $\frac{C}{T}$ as a function of T^2 below $3-4\,K^2$ in each sample.

This leaves the cause of the observed low temperature effects unclear and in need of further study. While interesting, in the case of BaC_6 it is frustrating that these previously unobserved anomalies should obscure the low temperature regime and thus make assessment of the predicted superconducting phase impossible. However, given the demonstration here of the inaccuracy of the predicted value of λ_{el-ph}, the recent work showing overestimation of the phonon energies and magnetisation studies reporting no superconducting phase at the predicted temperature, the issue is perhaps now resolved regardless.

3.6.3 Charge Density Wave Detection in CaC_6

The STM observation of a CDW phase in CaC_6 at a temperature of $78\,K$ [25] makes clear that $T_{CDW} \geq 78\,K$. In order to make an estimate of T_{CDW} equation 3.14 relating Δ_{CDW} and T_{CDW} can be used together with analogy with the similar system of $NbSe_2$.

$NbSe_2$ as a CDW system is a useful comparison for CaC_6. Both are hexagonally coordinated, quasi-2D, layered systems exhibiting type-II superconductivity [133] with superconducting transitions in the same temperature range and with similar superconducting gap size. Table 3.10 repeats several important characteristics of $NbSe_2$ with which comparison to CaC_6 is made.

For $NbSe_2$ $\frac{2\Delta_{CDW}}{k_B T_{CDW}} = 23.9$. Assuming the same ratio for CaC_6 the gap size of $2\Delta_{CDW} \approx 475\,meV$ yields an estimate of $T_{CDW} \sim 230\,K$. A cursory look at the measured heat capacity of CaC_6 above $78\,K$ (figure 3.20) shows no obvious transition-like shapes, although an extended feature is evident at high temperatures, above $\sim 215\,K$.

Interpretation of heat capacity measurements in this $210-300\,K$ region is complicated by the irregular contribution to the total heat capacity of the Apiezon N grease used to

Material	$\gamma\,(mJ/K^2/mol)$	$\beta\,(J/K^4/mol)$	$\Theta_D\,(K)$	$T_C\,(K)$	$\Delta_{SC}\,(meV)$	$\frac{2\Delta_{CDW}}{k_B T_{CDW}}$
$NbSe_2$	16.0[14]	$5.5x10^{-4}$ [14]	222[14]	7.2[134]	1.1[135, 136]	23.9 [14]
CaC_6	7.12	$1.943x10^{-4}$	406	11.5	1.6 [20] - 2.3 [118]	—

Table 3.10: Comparison of $NbSe_2$ and CaC_6.

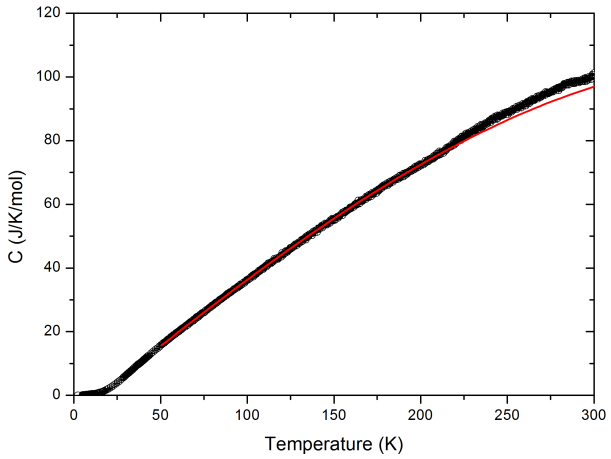

Figure 3.31: Heat capacity of CaC_6 as a function of temperature (black points) from $300\,K$ to $2\,K$ at zero magnetic field. Red line is a polynomial fit to the data between $50\,K$ and $180\,K$ extrapolated to $300\,K$ for comparison with data.

secure the sample to the platform. This difficulty manifests as variation in the temperature and magnitude of features due to the grease both across and within studies [137]. In order to make such features clear and avoid anomalous subtraction the high temperature heat capacity is presented in figure 3.31 without the grease contribution removed. Instead, following the analysis of Kwok [15] an extrapolated polynomial fit to the data has been subtracted in order to make clear any and all irregular features present in the CaC_6 heat capacity. The fit is shown in figure 3.31 and the data resulting from the subtraction in figure 3.32.

Figure 3.32 clearly shows that a step-like feature in the zero field and $10\,kOe$ heat capacity data arising at $\sim 210\,K$ and a peak at $\sim 290\,K$ are due to the Apiezon N grease (blue points). These two features are characteristic of the grease as studied by a number of heat capacity measurements [138, 27, 137], although it is noted that there is variation in both the temperature of the peak in the range $290 - 300\,K$, and its magnitude. The comparison here is made with $0.25\,mg$ of the grease, a good estimate of the amount used to mount the $5.0\,mg$ CaC_6 sample.

Other than the grease contribution the zero field CaC_6 curve shows a peak centred at $242\,K$ with a magnitude $1.4\,\%$ of C and a shape approximate to a smeared second-order transition. The $10\,kOe$ curve shows that the $242\,K$ peak is completely suppressed by magnetic field. Work by Graf [98] has shown suppression of a CDW state by

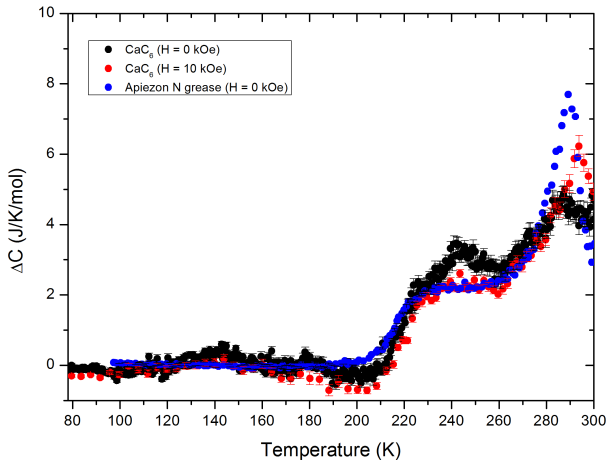

Figure 3.32: ΔC as a function of temperature from $78\,K$ to $300\,K$ for CaC_6 in zero magnetic field (black points), in a field of $10\,kOe$ (red points) and $0.25\,mg$ of Apiezon N grease in zero magnetic field (blue points). Apiezon N data taken from [27]. All curves obtained by subtracting an extrapolated polynomial fitted between $50\,K$ and $180\,K$.

magnetic field in a quasi-one-dimensional system but with complete suppression only achieved at high magnetic fields of $30 - 40\,T$ $(300 - 400\,kOe)$. It is therefore unlikely that this feature is a CDW peak given its suppression in an applied field of $1\,T$ $(10\,kOe)$. Further measurements will be needed to investigate this feature over a range of temperatures, magnetic fields and using grease with a less intrusive high temperature heat capacity contribution to discover its cause.

Overall, the above analysis suggests that the CDW transition in CaC_6 has not been observed. Several possible explanations for this conclusion are outlined below:

- The most simple explanation is that the CDW onset temperature is outside of the temperature range explored i.e. $T_{CDW} > 300\,K$. Given the large size of Δ_{CDW} in CaC_6 this is not unreasonable as other CDW systems with large Δ_{CDW} are known to have correspondingly high T_{CDW} e.g. the rare-earth tritellurides all have $T_{CDW} > 240\,K$ with $CeTe_3$ having $2\Delta_{CDW} \approx 400\,meV$ and $T_{CDW} > 450\,K$ [139].

- Despite the high resolution of the heat capacity measurements presented here it is possible that any transition in the temperature range $78 - 300\,K$ is unobserved because of the magnitude of the background C at these high temperatures. This would lead to a seemingly unreasonably small value of ΔC for a normal state to

CDW transition, but as STM measurements have observed the CDW is already commensurate with the lattice at $78\,K$. It is therefore possible that a smaller, ICDW to CCDW transition occurs in the temperature range $78 - 300\,K$ with the larger, normal to ICDW transition occuring above $300\,K$. If this were the case the ICDW-CCDW transition could well be hidden, given their general small size - e.g in TaS_2 the normal to ICDW transition is $22\,\%$ of C while the ICDW to CCDW transition is $< 0.1\,\%$ of C [14].

- Wang [140] observed that depending on the individual sample and method of preparation the magnitude of ΔC at the CDW transition and the width ΔT of the transition vary widely. Again it seems possible that any CDW transition has been smeared beyond recognition. This hypothesis could be tested by measuring more crystallographically perfect samples which could well yield a larger, detectable ΔC in future experiments.

- A final possibility is that the CDW observed in [25] is a surface state only i.e. the bulk of the CaC_6 remains normal. In this case the surface CDW's contribution to the overall heat capacity would likely be well below the measurable threshold at all temperatures.

3.6.4 The Nature of Superconductivity in CaC_6

The superconducting phase of CaC_6 is studied here as a function of both temperature and magnetic field. The superconducting heat capacity anomaly ΔC has been obtained by subtracting the normal state ($H = 10\,kOe > H_{C2}$) curve from the superconducting ($H = 0\,Oe$) curve. The results of this subtraction are shown below in figure 3.33 as $\frac{\Delta C}{T} = \frac{C_s - C_n}{T}$ as a function of T. For comparison a BCS curve with $T_C = 11.3\,K$ is shown.

Figure 3.33 shows that the transition temperature, defined as the centre of the transition, is consistent with previous measurements [44, 17, 141] with $T_C = 11.3 \pm 0.1\,K$. The electronic component at $T = 0$ is $\gamma = 6.95 \pm 0.03\,mJ/K^2/mol$, in line with the normal state fitted value from figure 3.26. The magnitude of the heat capacity jump $\frac{\Delta C}{T} = 8.6 \pm 0.1\,mJ/K^2/mol$. From this the reduced heat capacity jump is calculated as $\frac{\Delta C}{\gamma T_C} = 1.24 \pm 0.02$, lower than the BCS weak limit value of 1.426. This reduced value is further discussed below.

Also shown in figure 3.33 is a BCS curve calculated from tabulated values of $\frac{C}{C_{en}(T_C)}$ [28] using coefficients of $T_C = 11.3\,K$ and $C_{en}(T_C) = \gamma T_C = 7.12 T_C\,mJ/K/mol$.

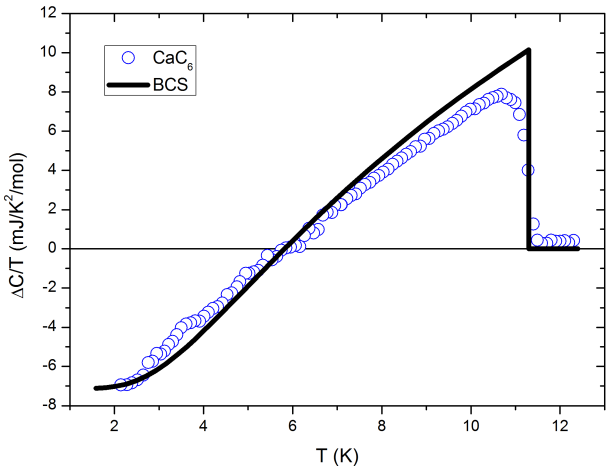

Figure 3.33: $\frac{\Delta C}{T}$ as a function of temperature for CaC_6 (blue points) showing the superconducting anomaly with $T_C = 11.3 \pm 0.1\,K$ at the centre of the transition (onset at $11.5\,K$), $\frac{\Delta C(T_C)}{T_C} = 8.6 \pm 0.1\,mJ/K^2/mol$, $\gamma = 6.95 \pm 0.03\,mK/K^2/mol$. Error bars are smaller than symbols at all temperatures. Also shown is a BCS curve (black line) calculated from the tabulated values of Mühlschlegel [28] with $T_C = 11.3\,K$ and $C_{en}(T_C) = \gamma T_C = 7.12 T_C\,mJ/K/mol$.

The overall temperature dependence is BCS-like, although at low temperatures ($0.2 < \frac{T}{T_C} < 0.5$) ΔC exceeds the BCS curve, while at higher temperatures ΔC is clearly lower.

As shown earlier in figure 3.21 the superconductivity is suppressed by the application of a magnetic field - with increasing field T_C falls and the transition broadens. Figure 3.34 shows the behaviour of T_C with field up to $H = 1.5\,kOe$ (above this field the transition is too smeared to measure accurately). A linear fit has been applied to the data which predicts $H_{C2}(T = 0) = 2.31 \pm 0.02\,kOe$, in agreement with previous measurements. This fit is used rather than a WHH fit because there is a clear linear relationship here, a feature exhibited by many other layered superconductors (e.g. [142, 143, 144]).

The dependence of γ on magnetic field can be used to describe the degree of anisotropy of the superconducting gap as a plot of $\gamma(H)$. If $\gamma(H) \propto H$ then the gap is isotropic, whereas if $\gamma(H) \propto H^{\frac{1}{2}}$ then the gap is strongly anisotropic. The difference between the isotropic and anisotropic cases is most marked at low fields because above $\sim 0.3 H_{C2}$ the slope of γ decreases even for isotropically gapped superconductors [145]. Figure 3.35 clearly shows a linear relationship of $\gamma(H)$ at low fields and a crossover into a non-linear regime above $\sim 0.3 H_{C2}$, suggesting an isotropic gap.

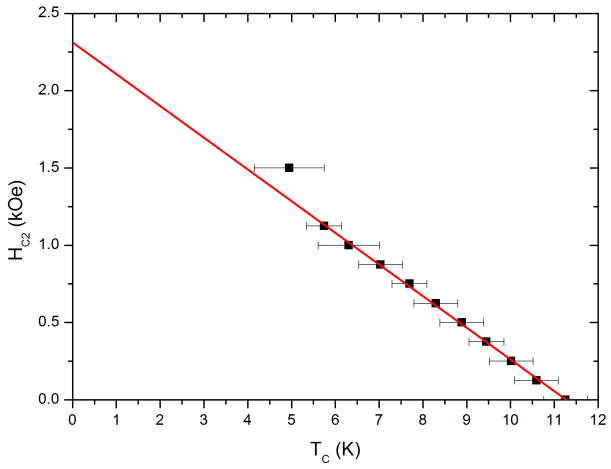

Figure 3.34: $H_{C2}(T)$ estimated from heat capacity measurements at the CaC_6 superconducting transition. T_C is measured at the mid-point of the transition and is shown with an error bar corresponding to the transition width. At fields greater than $1.5\,kOe$ the transition is too heavily smeared to measure. The red line is a linear fit to the data with $H \leq 1\,kOe$ indicating $H_{C2}(T=0) = 2.31 \pm 0.02\,kOe$.

From the calculation performed above, the electron-phonon coupling constant was estimated at $\lambda_{el-ph} = 0.7$, in the intermediate coupling regime. Thus, in summary, the results detailed above show that CaC_6 is a BCS-like superconductor in the intermediate-coupling limit with an isotropic or very slightly anisotropic gap in agreement with previous heat capacity measurements.

Above it was noted that while the temperature dependence of $\frac{\Delta C}{T}$ is clearly BCS-like, the measured value of $\frac{\Delta C}{\gamma T_C}$ is significantly reduced at 1.24 compared to the BCS value of 1.426. There are two main causes of a reduced $\frac{\Delta C}{\gamma T_C}$: Low coupling strength and gap anisotropy. If the electron-phonon coupling of a material is lower than that of the BCS weak-coupling case then $\frac{\Delta C}{\gamma T_C}$ will be reduced below 1.426. $\frac{\Delta C}{\gamma T_C} = 1.24$ is a significant reduction which implies weak-coupling. However, the electron-phonon coupling constant has been found in the normal state to be $\lambda_{el-ph} = 0.7$ which places CaC_6 firmly in the intermediate coupling regime and suggests that weak-coupling is not the cause of the reduced $\frac{\Delta C}{\gamma T_C}$.

Next the possibility that CaC_6 is an s-wave BCS-like superconductor but with some degree of gap anisotropy is assessed. Gap anisotropy manifests in heat capacity measurements as a redistribution of ΔC from temperatures close to T_C to lower temperatures,

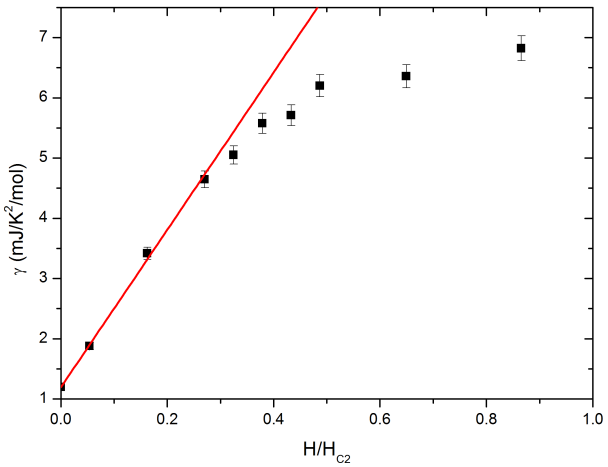

Figure 3.35: Sommerfeld constant γ as a function of magnetic field at $2\,K$. Note: While recording the superconducting heat capacity anomaly as a function of magnetic field it was observed that field history affected the outcome. For fields of $250\,Oe$ and $500\,Oe$ the field was applied at $2\,K$ and data recorded as the sample warmed through T_C. In all other cases the field was applied with $T > T_C(H = 0)$. At temperatures close to $T_C(H)$ no hysteresis effects were seen (this is clear from the linear relationship in figure 3.34). However, at low temperatures ($T < 4\,K$) behaviour for $H = 250\,Oe$ and $H = 500\,Oe$ is erroneous, due to pinning and surface barrier effects. Data points at fields $H = 250\,Oe$ and $H = 500\,Oe$ were omitted from the figure for this reason.

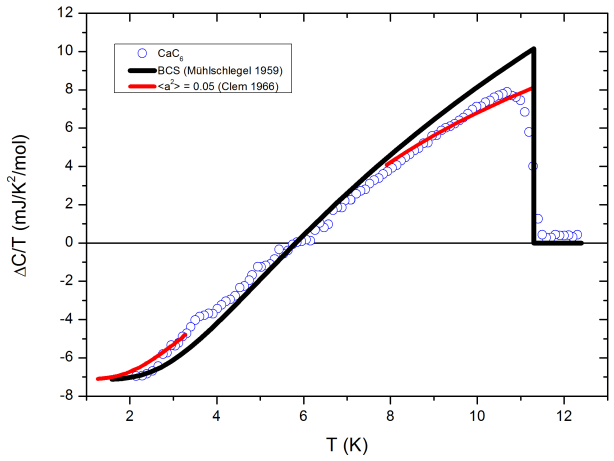

Figure 3.36: $\frac{\Delta C}{T}$ as a function of temperature for CaC_6 (blue points). The black line represents the BCS curve calculated from the tabulated values of Mühlschlegel [28]. The red line shows the high and low temperature behaviour of the anisotropic gap BCS model with $< a^2 >= 0.05$ [29]. This model is not applicable to the regime $0.3 < \frac{T}{T_C} < 0.7$ although a smooth interpolation between the low and high temperature ranges is expected.

leading to a reduced heat capacity jump $\frac{\Delta C}{\gamma T_C}$. Measurements of $\gamma(H)$ shown above have suggested an isotropic gap although mild anisotropy would cause little deviation from the observed linear behaviour.

In order to investigate this possibility a BCS model with an anisotropic gap has been employed to compare both the heat capacity jump and the overall temperature dependence of the anisotropic case with the data measured here. The model [29] has been used to predict the effect of mild anisotropy ($< a^2 >= 0.05$, where $< a^2 >$ is the mean-square anisotropy proportional to the angular average of the square of the deviation of the gap parameter from its average value) on the heat capacity at low temperatures ($\frac{T}{T_C} < 0.3$) and close to T_C ($\frac{T}{T_C} > 0.7$) - the employed model is not valid in the range $0.3 \leq \frac{T}{T_C} \leq 0.7$. Figure 3.36 shows the results of calculations using $T_C = 11.3\,K$ and $\gamma = 7.12\,mJ/K^2/mol$ in comparison with the BCS model and data.

The anisotropic model with $< a^2 >= 0.05$ clearly shows an improved description of the heat capacity jump $\frac{\Delta C}{T_C}$ compared to the BCS model. However, the temperature dependence at low temperatures and close to T_C does not show detailed agreement with the data, with the model displaying greater curvature in both regimes. More complex DFT modelled heat capacity predictions based on calculations of the vibrational and

electronic structures of CaC_6 [21] confirm these observations.

Given that both the calculations of Sanna and those of Boeri are based on CaC_6 phonon dispersions which have been shown by experiment to be accurate [9] it is perplexing that the disagreement with the heat capacity observations remains.

At this point it is interesting to consider once again the recent observation of the CDW at $78\,K$. As the work of Gabovich [101, 102, 16] has predicted, the coexistence of superconducting and CDW states reduces the magnitude of both the superconducting and CDW gaps when they share a Fermi surface. Assuming the CDW state coexists with superconductivity below $11.5\,K$ in CaC_6 it could well alter the nature of the superconducting state by reducing the available Fermi surface and thereby decreasing Δ_{SC}. Because T_C is dependent on Δ_{SC} the ratio $\frac{2\Delta_{SC}}{k_B T_C}$ would remain unchanged in this scenario. However, predictions of the magnitude of the superconducting heat capacity jump should overestimate because the calculations are based on the assumption of a complete Fermi surface, rather than the reduced version left by the CDW gapping. In this light, therefore, a simple explanation for the reduced value of $\frac{\Delta C}{\gamma T_C}$ is that ΔC corresponds to only the superconducting states whereas γ includes both the superconducting states and those which contribute to the CDW, meaning that ΔC is smaller than expected for the value of γ.

Another possibility must also be put forward, namely that the complex Fermi surfaces of CaC_6 allow 'peaceful' coexistence of the CDW and superconducting states. It was noted in [25] that the measured CDW state is strongly metallic, with $< 5\,\%$ change in the electrical conductivity within compared with outside the gap. This means that while the gap is large in terms of energy (at $2\Delta_{CDW} \approx 475\,meV$) the number of states at the Fermi level which are affected by the opening of the gap, and the total area of the Fermi surface gapped by the CDW are relatively small. It is therefore possible that below T_C the CDW and superconducting states gap different areas of the CaC_6 Fermi surface and therefore coexist with little competition. One way in which this could occur is if the CDW state is supported wholly by the doped graphene sheets as suggested in [25] and the superconducting state is hosted predominantly by the Ca intercalant atoms, as suggested by Calandra [10]. If this were the case the measured value of $\frac{\Delta C}{\gamma T_C}$ would identify CaC_6 as having an anisotropic gap in line with the calculations shown above.

The interplay between the superconducting and CDW states in CaC_6 requires further investigation to clarify the magnitude and nature of the effects. Theoretical predictions of superconducting behaviour which take the CDW state into account should be compared to the results herein and those of previous studies. In addition experimental attempts

should be made to suppress the CDW state as a method of perhaps increasing the T_C of CaC_6 above $11.5\,K$.

3.7 Summary

The heat capacities of the MC_6 graphite intercalation compounds CaC_6, SrC_6 and BaC_6 have been measured here over a wide range of temperatures. Portions of the heat capacities of CaC_6 [17] and SrC_6 [22] have been previously published, while the measurements of BaC_6 are the first to be presented.

The superconducting phase of CaC_6 has been previously characterised [17] and this work supports the previous primary findings of BCS-like, intermediate-coupling superconductivity. Comparison with an anisotropic BCS model suggests mild gap anisotropy as a partial explanation of the observed reduced heat capacity jump. In the temperature range not previously explored the onset anomaly of a CDW phase present at $78\,K$ [25] has not been detected up to a maximum temperature of $300\,K$ signifying that $T_{CDW} > 300\,K$, in line with other systems with similarly large CDW gaps. It is suggested that the reduction of available Fermi surface caused by the presence of the CDW phase at low temperatures may account for the inaccuracies of theoretical models in describing the measured superconducting heat capacity anomoly in CaC_6 [19].

The low temperature heat capacities measured here are well fitted by the Debye model with the additional dispersionless optical phonon modes originally described by Suganuma [127]. The resulting values of the electronic coefficient, Debye temperature and characteristic phonon temperatures fit well within the pattern described by other alkali-metal GICs. The electron-phonon coupling constant as estimated from the electronic coefficient is in agreement with theoretical predictions for CaC_6 and SrC_6 but is found to be substantially smaller in BaC_6 [18] suggesting that previous predictions of T_C [11] are overestimated in this compound. Novel Schottky-like anomalies have been observed at very low temperatures in SrC_6 and BaC_6, an effect not previously observed in the sole prior SrC_6 measurement in this temperature range [22].

Chapter 4

Ballistic Transport and Pseudogap State in FIB-Milled Kish Graphite Micro-Structures

4.1 Abstract

Graphite is an interesting system in which to study electrical phenomena because of the marked anisotropy of its properties and their dependence on the morphology of individual graphite types. It has been seen to display strong system size-effects at micro- and macroscopic scales at high temperatures only observed in other metallic conductors in the nanometre, liquid helium range.

Focused ion beam milling can be used to create electronic devices with complex shapes for studying electrical phenomena in reduced dimensions and particular geometries. Current-voltage characteristics of these devices can yield conductance as a function of voltage giving a spectroscopic insight into the behaviour of excitations and Fermi surface effects.

Here, focused ion beam milling has been used to create two micron-sized, c-axis stack devices electrically contacted by ab-plane graphite, from kish graphite precursors. Measurements of resistance as a function of temperature have observed large resistance offsets in both devices caused by ballistic transport through the devices due to mean

free paths of several microns. In device A this behaviour persists up to at least $250\,K$, while increased disorder and the reduction of the mean free path below the device dimensions causes device B to change behaviour at $\sim 130\,K$.

Current-voltage measurements have found the emergence of a Coulomb-like gap below $40\,K$ in device A, in agreement with previous observations in similar devices, thought due to localisation of carriers in the graphitic planes of the device region. Device B showed no such behaviour due to its increased disorder coupling the planes together more strongly. The pseudogap was seen to have a maximum size at $2\,K$ of $50 \pm 5\,mV$, noted as large for a Coulomb-type gap. Further complex features in the conductance of device A were observed and are discussed but remain of unknown cause.

The resistance-temperature measurements of devices A and B, as well as those of previous similar microscopic devices, have been analysed in the context of attempts to characterise the c-axis conduction of 'ideal' graphite. It is found that the results for devices A and B do not constitute such a measurement due to the mean free path being considerably greater than the device size. Previous measurements are also found not to exemplify ideal behaviour due to similar ballistic behaviour or included stacking faults. A test geometry which could allow such a measurement is suggested.

4.2 Theory and Phenomena

4.2.1 Drude Model of Electrical Conduction

The Drude model is a purely classical conduction theory in that it uses kinetic theory to describe the motion of a non-interacting gas of electrons in a metal [146]. In the model the only interactions of the electrons with the metallic lattice are instantaneous, momentum altering collisions. In the absence of an electric field $\overrightarrow{E}$ the electrons exhibit random walk motion with an average velocity v_{av}. The direction of $\overrightarrow{v}$ after each collision is random, so $v_{av} = 0$. In an electric field $\overrightarrow{E} > 0$ the electrons are accelerated between collisions, in the direction opposite to $\overrightarrow{E}$. If the applied field in constant then Newton's second law gives a velocity:

$$\overrightarrow{v} = \overrightarrow{v_0} - \frac{e\overrightarrow{E}\tau}{m} \tag{4.1}$$

where v_0 is the electron velocity; e is the electron charge; m is the electron mass. Taking the average velocity of all the electrons eliminates v_0, while the second term is

just a constant multiplied by the average time between collisions τ. This time is related to the average distance travelled between collisions - the mean free path λ_{MFP} - as:

$$\tau = \frac{\lambda_{MFP}}{v}$$

If the conduction electron density is n_e and the charge of each electron e then the current density within the metal can be written as:

$$j = -n_e e v \tag{4.2}$$

Substituting equation 4.1 into equation 4.2 gives:

$$j = \left(\frac{n_e e^2 \tau}{m}\right) E = \sigma E \tag{4.3}$$

where σ is the Drude conductivity. Equation 4.3 is a form of Ohm's law and conductors which obey it are considered 'Ohmic'.

The Drude model is successful in using the average electron velocity to find the electrical current but does not describe how electrons actually move through a conductor. This detail is contained within λ_{MFP}.

The purely classical approach predicts that λ_{MFP} is on the order of the unit cell size as electrons scatter from the metal ions. This is not the case and a quantum approach describes the propagation of electron waves through the oscillating ionic potential and their scattering from lattice imperfections and distortions. These different types of scattering contribute different elements of λ_{MFP}. The inelastic mean free path l_i gives the average distance between inelastic scatterings, such as by phonons, while the elastic mean free path l_e gives the average distance between elastic scatterings, such as by lattice imperfections or other carriers. These elements contribute to λ_{MFP} as:

$$\lambda_{MFP} = \left(\frac{1}{l_i} + \frac{1}{l_e}\right)^{-1}$$

The electrical resistivity $\rho = \sigma^{-1}$ and is therefore proportional to λ_{MFP}^{-1}. In a metal free from lattice imperfections $\rho(T)$ is governed mainly by the scattering of electrons by phonons. This scattering is an inelastic process in that it involves the absorption or emission of a phonon by an electron, which changes the electron's energy and wave

vector. As such it is reflected in l_i. At high temperatures, above the Debye temperature Θ_D (see section 3.2.1) the number of phonons is proportional to T, so that:

$$\rho \propto T \qquad\qquad T \gg \Theta_D \tag{4.4}$$

Below Θ_D only a reduced number of phonons with energy $\lesssim k_B T$ can be absorbed or emitted by electrons. These phonons have small wave vectors meaning that each electron can only be scattered through a small angle. This reduces the resistivity greatly both because the effect of individual small angle scattering events is not large and because the number of phonons which can take part in the scattering is greatly reduced. The resistivity then approximately follows the law:

$$\rho \propto T^5 \qquad\qquad T \ll \Theta_D \tag{4.5}$$

In any real conductor this behaviour is modified at low temperatures by scattering from crystal imperfections. These scattering events are elastic and are therefore reflected in l_e. Electrons are scattered with an approximately constant cross-section giving a contribution to the resistivity that is independent of temperature:

$$\rho_0 = constant \tag{4.6}$$

The above behaviours are combined together to describe the temperature dependence of the total resistivity as:

$$\rho_{total}(T) = \rho_0 + \rho(T) \tag{4.7}$$

For an individual sample its resistance R is related to the resistivity ρ by its length l and cross-sectional area A as:

$$R = \rho \frac{l}{A} \tag{4.8}$$

4.2.2 Ballistic Transport

The Drude description of Ohmic conduction implicitly assumes that λ_{MFP} is much smaller than the characteristic system size L. As described above, when $\lambda_{MFP} \ll L$

electrons undergo numerous scattering events as they travel through the system and as a result the resistivity is dominated by electrons scattering from phonons and crystal imperfections. However, as the dimensions of the system are reduced a regime is approached in which $\lambda_{MFP} \gtrsim L$. In this regime electrons travel through the system without collisions i.e. ballistically, τ becomes infinite and the Ohmic description breaks down.

One such geometry in which this transition from Ohmic to ballistic transport must be considered is that of a small circular constricting orifice of diameter W between two bulk conductors of resistivity $\rho(T)$. At high temperatures $\frac{\lambda_{MFP}}{W} \ll 1$, and an Ohmic contribution to the resistance found by Maxwell [147] is seen as:

$$R_M = \frac{\rho(T)}{W} \tag{4.9}$$

As the temperature is reduced the ratio $\frac{\lambda_{MFP}}{W}$ increases and the Ohmic value is corrected by a factor $\Gamma(k)$ of the order of unity, where $k = \frac{W}{\lambda_{MFP}}$. $\Gamma(k \to \infty) = 1$ and varies smoothly to $\Gamma(k \to 0) = 0.67$ [148]. Once λ_{MFP} increases such that the ratio $\frac{\lambda_{MFP}}{W} \gtrsim 1$ a dominant, ballistic resistance term appears [149, 150] as:

$$R_B = \frac{4\rho(T)\lambda_{MFP}(T)}{3A} \tag{4.10}$$

where $A = \frac{\pi W^2}{4}$ is the area of the constriction. Equations 4.9 and 4.10 are combined to give an expression known as the Knudsen-Sharvin equation which describes the total resistance arising from the constriction as:

$$R_{KS} = \frac{4\rho(T)\lambda_{MFP}(T)}{3A} + \Gamma(k)\frac{\rho(T)}{W} \tag{4.11}$$

4.2.3 Coulomb Interactions

As noted above, one of the assumptions of the Drude model of conduction is that the electrons do not interact with each other - that they are independent. In systems with low carrier concentrations, on the metal-insulator border, Coulomb interactions are not fully screened and must be accounted for.

One such system was described by Efros and Shklovskii [151] (ES). In the ES system electron states close to the Fermi level are localised and conduction occurs by hopping between sites.

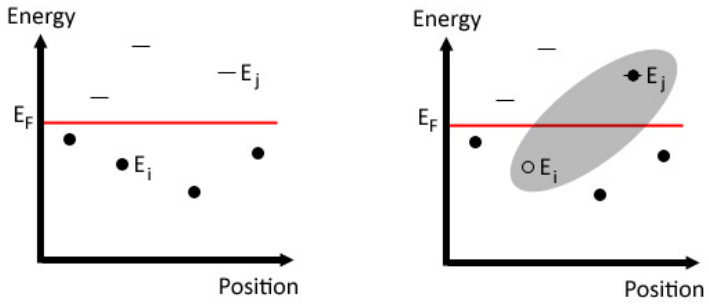

Figure 4.1: Schematic representation of electron energy states localised in space in the ES system. Left: A set of localised states at $T = 0$. All states below the Fermi level are occupied while all states above the Fermi level are unoccupied. Right: An electron from below the Fermi level is moved to a state above the Fermi level, leaving a hole behind. The shaded region represents the resulting Coulomb interaction between the electron and hole.

At $T = 0$ all energy states below the Fermi level are occupied and all states above are vacant - this situation is shown schematically in the left panel of figure 4.1. The transfer of an electron from state i to state j (right panel of figure 4.1) increases the energy of the system by an amount $\Delta E = E_j - E_i - e_{ij} > 0$ where $e_{ij} = \frac{e^2}{\kappa r_{ij}}$ is the energy of the Coulomb interaction between the electron now in state j and the hole in state i (e is the electronic charge, κ is the dielectric constant and r_{ij} is the distance between the states). If the distance between the states is large then $e_{ij} < E_j - E_i$ and the energy of the system is increased, but if the distance is small e_{ij} will be large and will overcompensate $E_j - E_i$. Hence, for the original inequality to hold the states must be far apart and, therefore, the density of states is small. This means a reduction in the DOS at the Fermi energy with a width E_C defined when the Coulomb energy is equal to the difference in energy of the states. In 3D this 'pseudogap' is quadratic in E as:

$$g(E) = \alpha_{3D} E^2$$

where $\alpha_{3D} = \frac{3}{\pi} \frac{\kappa^3}{e^6}$.

At $E \gg E_C$ the DOS approaches the constant value g_0, while in the limit of small E the DOS approaches the above parabolic dependence. As an approximation of the entire range of E the following equation is used [152]:

$$g(E) = \alpha_{3D} \frac{E_C^2 E^2}{E_C + E^2} \tag{4.12}$$

The gap described by equation 4.12 is described as a 'soft' gap in that $g(E) \propto E^2$ at E_F, rather than a 'hard' gap in which $g(E)$ not only equals zero at E_F but also in the vicinity.

4.3 Introduction and Experimental Motivation

4.3.1 Electrical Resistance in Graphites

The resistivity of graphite is strongly anisotropic between the in-plane direction and along the c-axis [48]. In-plane conduction is metallic at all temperatures i.e. $\frac{d\rho}{dT}$ is positive. At low temperatures (below $\sim 10\,K$) the dominant contribution to the in-plane electrical resistivity $\rho_{ab}(T)$ is the elastic scattering of carriers by structural defects and impurities. The degree of 'faultedness' of a graphite sample has historically been estimated from the value of the residual resistivity ratio (RRR), the ratio of the in-plane resistivity at high temperatures to that at low temperatures (equation 4.13). Higher values of RRR indicate less faulted graphites and vice versa.

$$RRR = \frac{\rho_{ab}(300\,K)}{\rho_{ab}(4.2\,K)} \tag{4.13}$$

Above $\sim 10\,K$ scattering by phonons becomes dominant, giving $\rho_{ab}(T)$ a steep increase as $\sim T^3$ then tending towards a high temperature linear-T behaviour of a metal above its Debye temperature, $\Theta_D \sim 420\,K$ in-plane [129, 128, 130].

Representative measurements from a number of studies of $\rho_{ab}(T)$ of kish, natural and HOPG graphites are shown in figures 4.2, 4.3 and 4.4, respectively. From these figures it is clear that the general temperature dependence of ρ_{ab} is metallic and is common across graphite types and samples. However, the low temperature behaviour and the residual resistance are strongly dependent on the microstructure of each individual sample. For kish graphite samples RRR is independent of in-plane crystallite size and low temperature λ_{MFP} is calculated to be considerably smaller than the crystallites [3], showing that λ_{MFP} is limited by the crystal defects and impurities. Table 4.1 gives representative values of RRR, λ_{MFP} at $4.2\,K$ and average in-plane crystallite size. This is also the case for natural graphites, which generally display greater values of RRR due

Graphite type	RRR	$\lambda_{MFP}(4.2\,K)$ (μm)	Average in-plane crystallite size (μm)
Kish [a]	4.65	3.2	~ 1000
Kish [a]	11.9	7.3	$-$
Kish [a]	34.3	12.2	~ 1000
HOPG [a]	5.50	5.4	~ 60
HOPG [b]	6.8	$-$	55.5
HOPG [b]	8.1	$-$	58.7

Table 4.1: Values of RRR, λ_{MFP} at $4.2\,K$ and average in-plane crystallite size for kish and HOPG samples. Data taken from [a][3] and [b][46].

to their lower defect concentrations. In samples of HOPG with a metallic $\rho_{ab}(T)$ it is unclear as to whether λ_{MFP} is limited by crystallite size or defect prevalence. Typical crystallites are observed by ECCI [3] to have diameter $\sim 60\,\mu m$ and calculations show $\lambda_{MFP}(4.2\,K) \sim 6\,\mu m$ which suggests defect limiting, however as ECCI cannot detect crystallite boundaries aligned better than 4^o the true crystallite size may actually be $\sim 6\,\mu m$ [46]. HOPG samples with non-metallic $\rho_{ab}(T)$ such as that shown in figure 4.4 (black squares) are discussed below.

c-axis resistivity ρ_c (figures 4.5, 4.6, 4.7, 4.8 and 4.9) is seen to be between 10^2 and 10^4 times higher than ρ_{ab}. Its temperature dependence is metallic, semiconducting-like (negative $\frac{d\rho}{dT}$) or a combination of the two depending on both the type and microstructure of the graphite tested. For kish and natural graphite samples with RRR $\lesssim 15$ $\rho_c(T)$ tends to show a metallic temperature dependence at low temperatures becoming semiconducting-like at higher temperatures - figures 4.5, 4.6 and 4.8. For RRR $\gtrsim 15$ the temperature dependence is mainly metallic with the semiconducting-like behaviour at higher temperatures still. Some kish graphite samples have been seen to display only a metallic dependence as shown in figure 4.7, while several natural graphite samples reported as single crystal behave similarly, although the moniker 'single crystal' must be questioned given that $\rho_c(T)$ differs markedly between these samples - figure 4.8. The temperature dependence of ρ_c for HOPG differs from those of kish and natural graphites, as is seen in figure 4.9; RRR no longer predicts c-axis behaviour, with samples with RRR$= 60$ displaying the same temperature dependence as those with RRR~ 10.

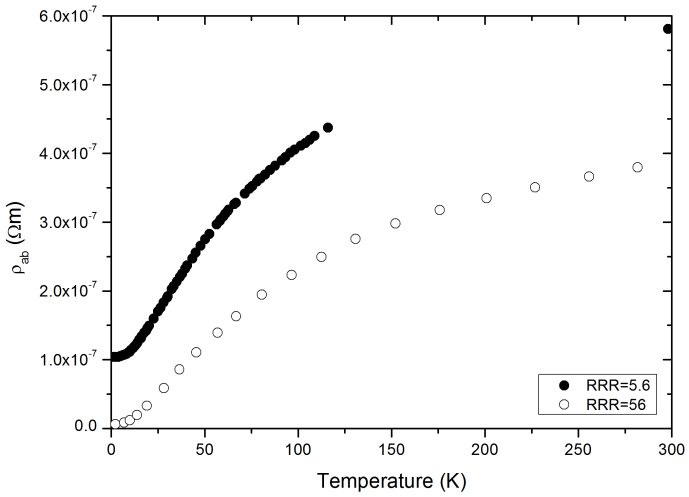

Figure 4.2: Resistivity as a function of temperature in-plane of two kish graphite samples showing typical behaviour. Key designations are according to RRR. Data taken from [30, 31].

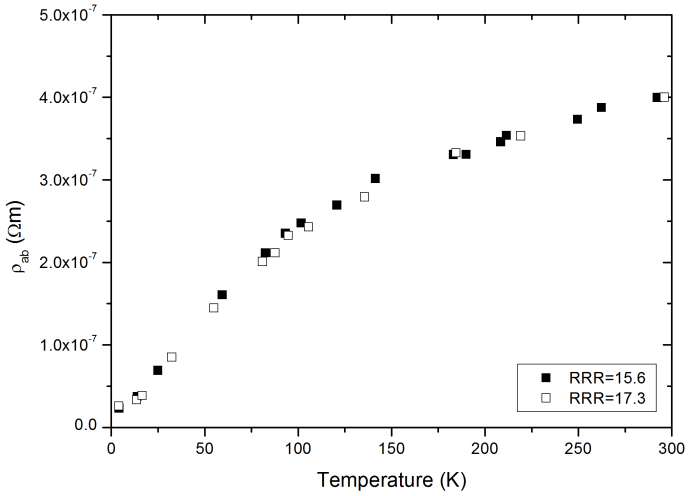

Figure 4.3: Resistivity as a function of temperature in-plane of two natural graphite samples showing typical behaviour. Published relative resistance values have here been scaled by absolute values of resistivity in similar samples measured by Primak of $\rho_{ab}(300\,K) = 4.0\text{x}10^{-7}\,\Omega m$. Key designations are according to RRR. Data taken from [32].

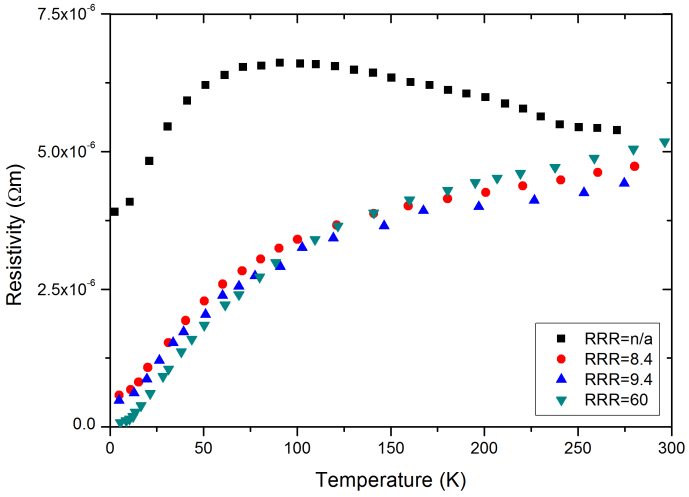

Figure 4.4: Resistivity as a function of temperature in-plane of four HOPG graphite samples showing typical behaviour. Key designations are according to RRR for purely metallic samples only. Data taken from [33, 34].

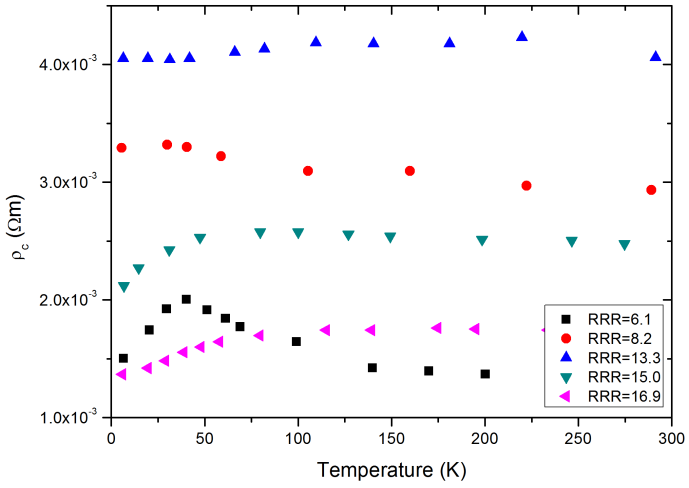

Figure 4.5: Resistivity as a function of temperature along the c-axis of five kish graphite samples showing typical behaviour. This data is presented normalised in figure 4.6. Key designations are according to RRR. Data taken from [35].

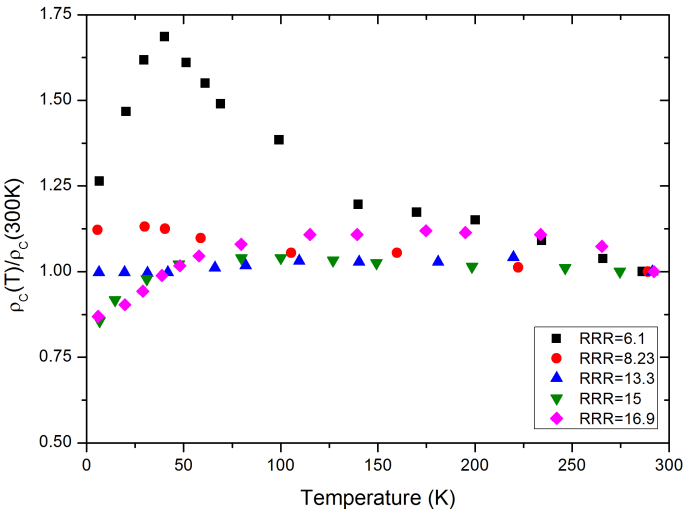

Figure 4.6: $\rho_C(T)/\rho_C(300\,K)$ of the five kish graphite samples shown in figure 4.5. Key designations are according to RRR. Data taken from [35].

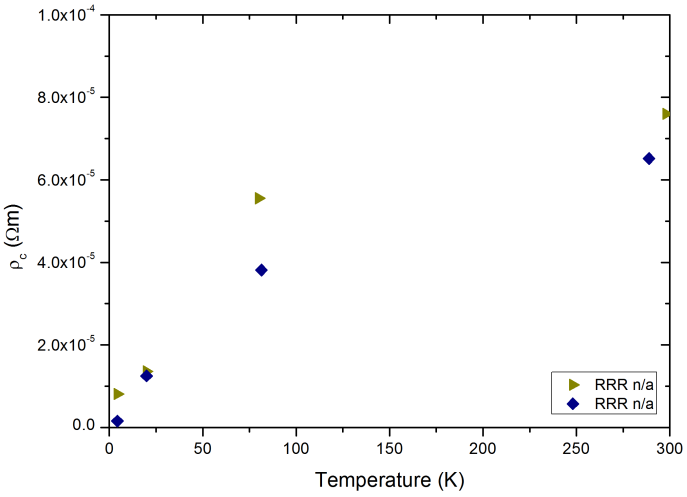

Figure 4.7: Resistivity as a function of temperature along the c-axis of two kish graphite samples showing typical behaviour. RRR values are not available for these measurements. Data taken from [36].

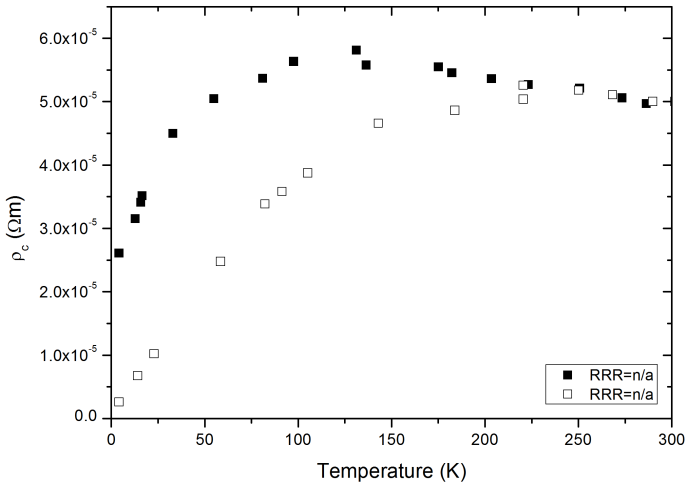

Figure 4.8: Resistivity as a function of temperature along the c-axis of two natural graphite samples showing typical behaviour. Published relative resistance values have here been scaled by absolute values of resistivity in similar samples measured by Primak of $\rho_c(300\,K) = 5\text{x}10^{-5}\,\Omega m$. RRR values are not available for these measurements. Data taken from [32].

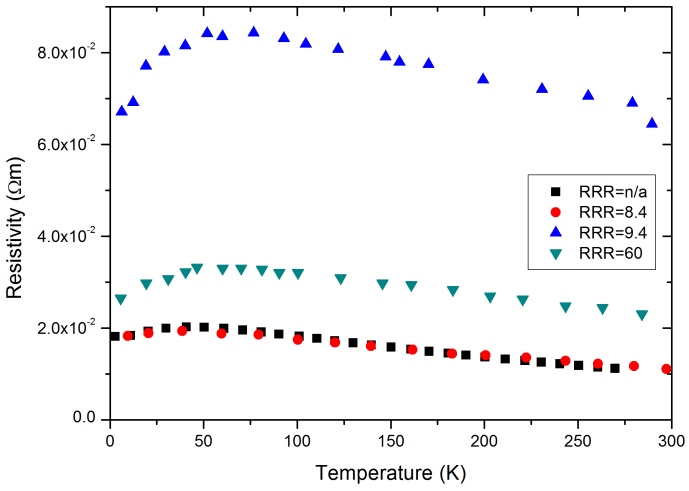

Figure 4.9: Resistivity as a function of temperature c-axis of four HOPG graphite samples showing typical behaviour. Samples are the same as those presented in figure 4.4. Key designations are according to RRR for purely metallic samples only. Data taken from [33, 34].

Several theories have been put forward to explain the variation in the behaviour of $\rho_c(T)$ in HOPG. The magnitude of c-axis resistivity is predicted, in a theory by Ono [40], by postulating regularly spaced stacking faults at which carriers are either reflected or tunnel through. The semiconducting-like behaviour is then given by the thermal excitation of carriers across the low potential barrier formed at each stacking fault. The work of Matsubara [34] explains the metallic-like downturn at lower temperatures by a crystal defect-assisted interlayer hopping conduction, in conjunction with phonon-carrier scattering. Together these theories suggest that $\rho_c(T)$ of 'ideal' i.e. unfaulted graphite has a metallic behaviour.

For each of HOPG, kish and natural graphites the above theories describe the following:

- The high $\rho_c \sim 10^{-2}\,\Omega m$ of HOPG samples (figure 4.9) indicates large potential barriers along the c-axis arising from a combination of a high frequency of stacking faults and a large mismatch at those faults (through a lack of layer registration across the fault). The extent of the metallic-like behaviour at low temperatures is governed by increased coupling between layers at crystal defect sites. The behaviour displayed by the sample represented by the black points [33] in figures 4.4 and 4.9 is qualitatively different to the other displayed samples. At first sight it would appear that stacking faults along the c-axis are contributing to $\rho_{ab}(T)$ as would be expected in a sample with crystallites not aligned parallel in-plane, i.e. with a very large mosaic spread. However, the spread of this sample is 0.4^o so this cannot be the case. Instead it is suggested that the in-plane boundaries between crystallites are so badly matched that sizable potential barriers are formed, which then act in a similar way with temperature as stacking faults along the c-axis. This suggests that mosaic spread is not a good guide to microscopic perfection from the point of view of electrical conduction and that HOPG is not a good approximation for 'ideal' graphite.

- In kish graphites with $\rho_c \sim 10^{-3}\,\Omega m$ (figure 4.5) samples with more crystal defects (lower RRR) display a similar behaviour to HOPG but with a lower resistivity and a sharper transition between low temperature metallic-like and high temperature semcionducting-like behaviours. This is suggested as being due to a smaller number of stacking faults and good registration of planes across faults (i.e. uniform potential barrier size).

- In kish and natural graphites with $\rho_c \sim 10^{-5}\,\Omega m$ (figures 4.7 and 4.8) there are very few stacking faults, giving the lower resistivity and predominantly metallic

temperature dependence. Low levels of crystal defects act to enhance interlayer coupling and as scattering centres.

To reiterate, the above theories of Ono [40] and Matsubara [34] make the prediction that unfaulted, defect-free 'ideal' graphite should have a purely metallic behaviour in both $\rho_{ab}(T)$ and $\rho_c(T)$, with $\rho_{ab} \ll \rho_c$. In this light the kish and natural graphite samples with $\rho_c \sim 10^{-5}\,\Omega m$ are the closest to a validation of these theories. However, recent work by Kempa [33] studying the magnetic field driven metal-insulator transition (MIT) in kish and HOPG graphites has found strong similarity between $\rho_{ab}(T, B)$ and $\rho_c(T, B)$ indicating that the metallic behaviour of $\rho_c(T)$ is correlated with that of $\rho_{ab}(T)$ through enhanced interlayer coupling by crystal defects. If this is the case then $\rho_c(T)$ for 'ideal' graphite would not be expected to be metallic.

It is clear from the above descriptions of macroscopic measurements that it is not possible to verify either of these predictions for $\rho_c(T)$ by testing macroscopic samples because even the most perfect samples contain both stacking-faults and defects. Another way to approach this problem is to test a sample with dimensions smaller than the average fault spacing, a sample which would be unfaulted by definition. The processing undertaken in this thesis aims to create such a test device from a kish graphite precursor and the electrical measurements made on these devices are later analysed and presented in the context of the above theories.

4.3.2 Micron-Sized Stack Devices

In 1998 a technique for making intrinsic Josephson junctions in layered high temperature superconductors was developed [37]. Focused ion beam (FIB) milling of $Bi_2Sr_2CaCu_2O_{8+\delta}$ crystals was used to create micron-sized devices in which an electrical test current was forced across the alternate conducting and insulating crystal layers along the c-axis creating a series of tunnel junctions (a 'stack'), while allowing the remaining ab portions of the crystal to be used for electrical contact to the stack. Figure 4.10 shows a schematic of the stack device created.

Subsequently this technique was used with other layered conductors to measure the energy gaps of the CDW states of $NbSe_3$, TaS_3 and KMo_6O_{17} as a function of temperature [153, 38, 154]. Figure 4.11 shows one of the stack devices created.

Although not stated in the literature, in essence the method employs a tunneling mechanism where electrical transport occurs between elementary conducting layers separated

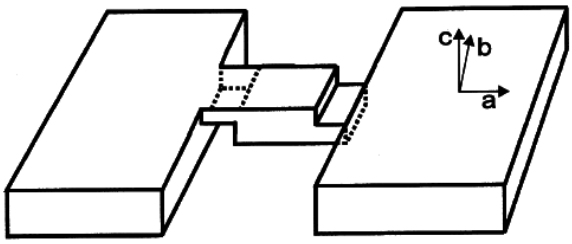

Figure 4.10: Schematic of the FIB-milled structure used to study superconductivity in high temperature superconductors. The ab direction is in-plane; c is the cross-plane direction. Figure adapted from [37].

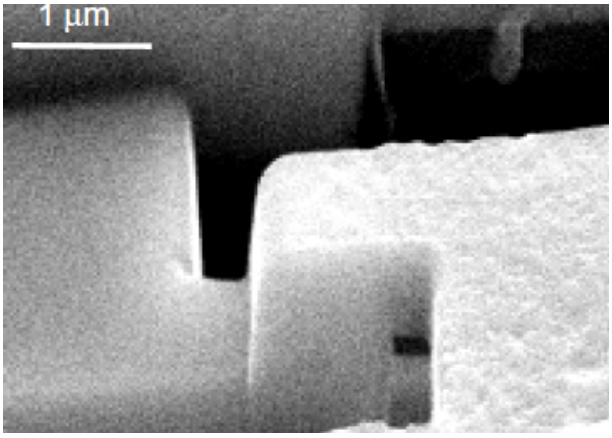

Figure 4.11: Scanning electron microscope (SEM) image of a 1 μm x 1 μm stack device. Figure taken from [38].

by elementary insulating layers. In such a conductor-insulator-conductor situation the conductance $\frac{dI}{dV}$ is proportional to the electronic DOS of the conductors as [12]:

$$I = A\left|T\right|^2 \int_{-\infty}^{\infty} g_1(E)g(E+eV)[f(E)-f(E+eV)]dE \tag{4.14}$$

$$\frac{dI}{dV} = A\left|T\right|^2 g_1(E_F)g(eV) \tag{4.15}$$

where A is a constant of proportionality; T is a constant tunneling matrix element; $g(E_F)$ is the DOS of the conductor at the Fermi level; V is the applied voltage; $f(E)$ is the Fermi function.

In 2008 the technique was used with a natural graphite precursor to create a graphitic stack device [39] of the same form as those shown in figures 4.10 and 4.11. The device consisted of a constricted region of dimensions $1\,\mu m$ x $1\,\mu m$ in-plane and $300\,nm$ in height within which electrical current was forced along the c-axis. The temperature dependence of the device resistance was found to display behaviour unlike either c-axis or in-plane graphitic conduction as shown in the left panel of figure 4.12: With decreasing temperature the device resistance increased gradually for $100\,K \lesssim T \lesssim 300\,K$, becoming temperature independent for $30\,K \lesssim T \lesssim 100\,K$ and showing a pronounced rise for $T \lesssim 30\,K$. In-plane resistance-temperature measurements of a bulk/unmilled sample 'from the same batch' showed a very low value of RRR~ 5 and behaviour uncharacteristic of natural graphite. The most similar literature sample is the HOPG sample previously shown by the black points in figure 4.4, the behaviour of which is likely due to highly misaligned crystallites in-plane.

Conductance calculated as $\frac{dI}{dV}$ from current-voltage (IV) characteristics was metallic at high temperatures but below $\sim 30\,K$ developed a gap-like shape centred around zero bias (right panel of figure 4.12). This behaviour was suggested to be the opening of a pseudogap due to the presence of interlayer correlations possibly mediated by the Coulomb interaction, or the precursor to a more ordered gap state such as superconductivity or CDW. By analogy with a similar pseudogap observed in a carbon nanotube stack device the graphitic pseudogap was stated as intrinsic to the graphite.

Very recently measurements of the electrical properties of similar graphite structures were performed [41]. Two stack devices with in-plane dimensions $1\,\mu m$ x $1\,\mu m$ and c-axis heights $100\,nm$ and $200\,nm$ were fabricated from an HOPG precursor. The measured resistance-temperature behaviour and IV characteristics are shown in figure 4.13.

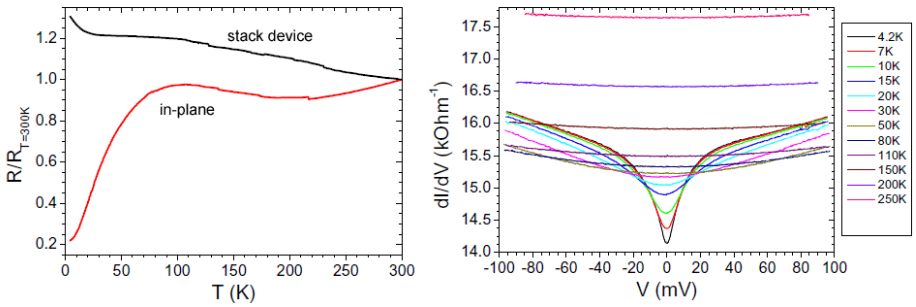

Figure 4.12: Left: Temperature dependence of the scaled resistance of the device and an in-plane measurement of a graphite sample from the same batch. Right: Temperature dependence of $\frac{dI}{dV}$ as a function of voltage for the natural graphite device. Figures adapted from [39].

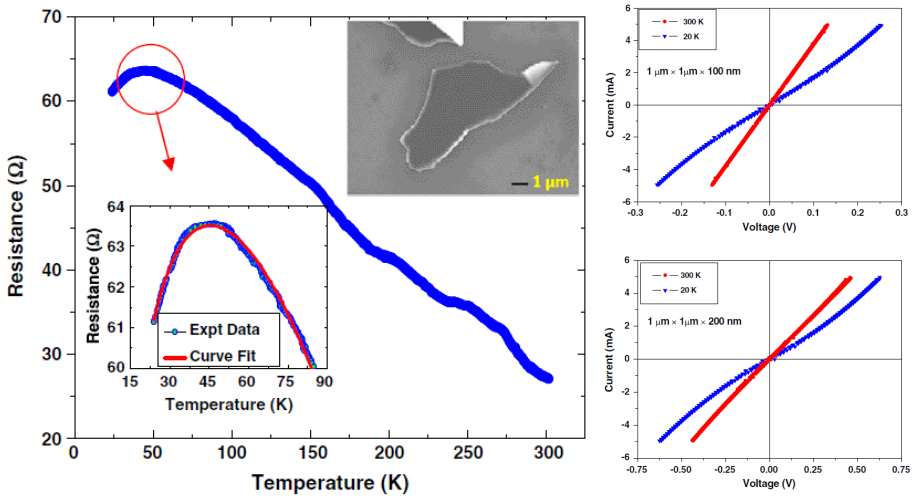

Figure 4.13: Left: Resistance as a function of temperature for the HOPG $1\,\mu m$ x $1\,\mu m$ x $100\,nm$ stack device showing semiconducting-like dependence (curve fit is a c-axis conduction fit based on [40, 34]) Inset: precursor HOPG flake. Right: IV characteristics at $300\,K$ and $20\,K$ for $1\,\mu m$ x $1\,\mu m$ x $100\,nm$ and $1\,\mu m$ x $1\,\mu m$ x $200\,nm$ devices showing linear behaviour at 300 K and smooth nonlinear behaviour at $20\,K$. Figures adapted from [41].

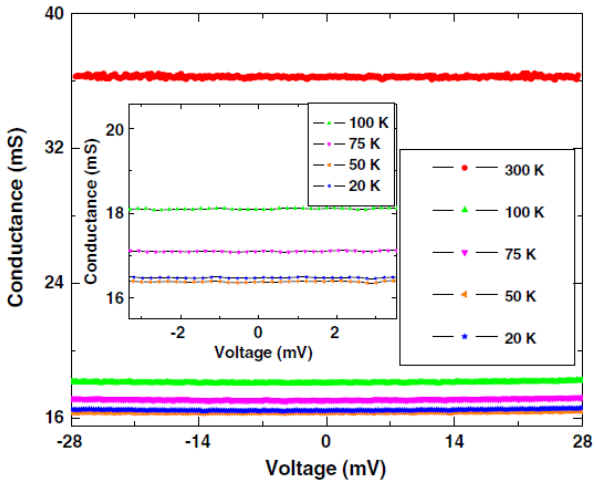

Figure 4.14: Conductance as a function of voltage for the $1\,\mu m$ x $1\,\mu m$ x $100\,nm$ stack device. Note the absence of the pseudogap feature observed in [39]. Figure adapted from [41].

For both devices measurements of the resistance as a function of temperature showed a semiconducting-type behaviour typical of c-axis macroscopic HOPG (as shown in figure 4.9), while IV characteristics were linear at $300\,K$ and smoothly nonlinear at $20\,K$ (the lowest measured temperature). Conductance as a function of voltage between $300\,K$ and $20\,K$ was metallic in the $V \lesssim 30\,mV$ range (figure 4.14) and did not show the pseudogap feature described above [39].

Several factors can be suggested as being responsible for the variation in the conductance findings between [39] and [41]. Firstly, the precursor graphite of which the stack devices are composed; natural graphite was used in [39] while [41] used HOPG. Natural graphite is composed of larger crystallites in the c-direction than HOPG [59, 4] and crystallites in HOPG are not well registered in the ab-plane. HOPG, therefore, contains more potential barriers to conduction along the c-axis. In combination with the differences in c-axis height of the stack devices ($300\,nm$ in [39], $100\,nm$ and $200\,nm$ in [41]) different behaviour should be expected.

In order to clarify the findings to date it is desirable to perform further measurements on similar stack devices with the aim of examining both the observed pseudogap and resistance-temperature behaviour. Kish graphite has crystallite sizes comparable to natural graphite and significantly greater than HOPG, while also having a greater crystal

defect concentration than both. As such it serves as a good precursor material from which to make comparative stack devices, as detailed and tested in this thesis. Further, the devices created here have c-axis stack height between the $200\,nm$ of [41] and the $300\,nm$ of [39] allowing study of the dependence of the conductance behaviour on device dimensions.

4.4 Experimental Details

In order to create the graphite stack devices described in this thesis a number of macroscopic and microscopic steps were performed. The main stages of the processing were: creating thin, narrow graphite pieces, forming electrical contacts and FIB milling. These main stages are outlined schematically in figure 4.15.

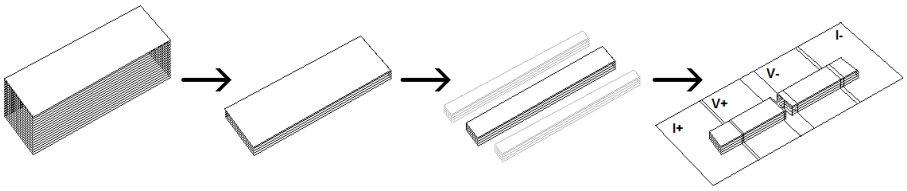

Figure 4.15: Main stages involved in macro- and microscopic processing of graphite flakes to form stack devices. From left to right: Bulk flake is cleaved to thin and then trimmed to narrow; current (I) and voltage (V) contacts are deposited and the stack device fabricated by FIB milling between the voltage contacts.

4.4.1 Graphite Precursor

Kish graphite pieces (supplied by Corus Steel, via Andrew Walters - ESRF) were used as the basis for the stack devices. Those chosen for this experiment were the largest and were up to $\sim 8\,mm$ x $\sim 8\,mm$ with a thickness of $\sim 80 \pm 20\,\mu m$ as measured using a Dektak surface profiler. X-ray diffraction of the graphite [002] peak (figure 4.16) showed the 'jagged' pattern characteristic of kish graphite, being constituted of grains ordered in both in-plane and c directions.

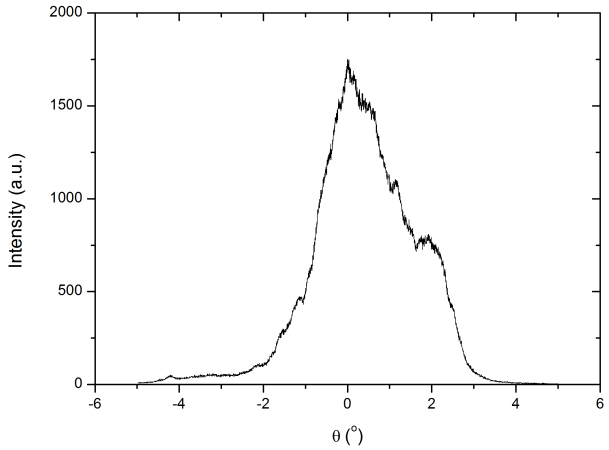

Figure 4.16: Rocking curve of [002] x-ray diffraction peak (theta-theta scan).

4.4.2 Macroscopic Preparation

Very thin samples of kish graphite were needed for the microscopic/FIB stage of the preparation, as FIB milling is a slow process and macroscopic thinning reduces the subsequently required milling time. The kish graphite pieces were thinned through repeated cleaving by securing each to a thick glass slide using a minute amount of superglue and taking multiple cleaves using 3M 'Magic Tape' [36]. The first cleave in each case was discarded as the top surface of each sample was invariably very rough and pitted, whereas further cleaves were smoother. This difference can be seen in SEM images of the surfaces shown in figure 4.17.

The thin cleaves were then floated off the tape in isopropanol and deposited onto individual SiO_2 substrates before being dried in a vacuum oven. Each sample was assessed under 400X microscopy and those with the fewest visible structural flaws chosen for further processing - figure 4.18 shows a representative sample at this stage.

Chosen samples were then narrowed to $\sim 300\,\mu m$ width by careful sawing using razor blades. Slight crush damage was inevitably caused at the cut edges of each sample but the central regions where the devices were to be created remained undisturbed. Processing to this point for the two samples further discussed herein resulted in the dimensions shown in table 4.2.

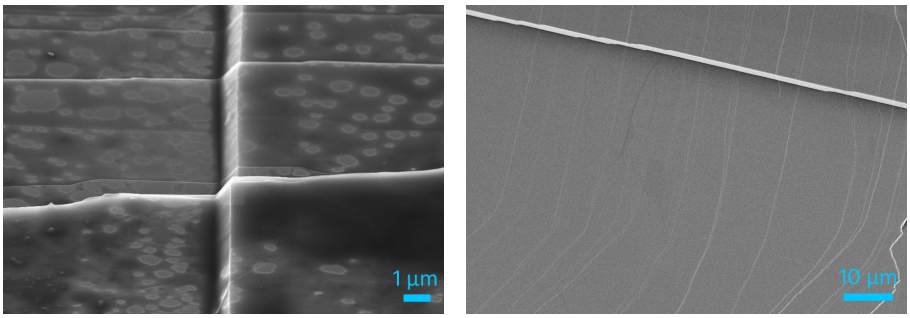

Figure 4.17: Left: SEM image of initial kish top surface. Right: SEM image of kish top surface after several cleaves.

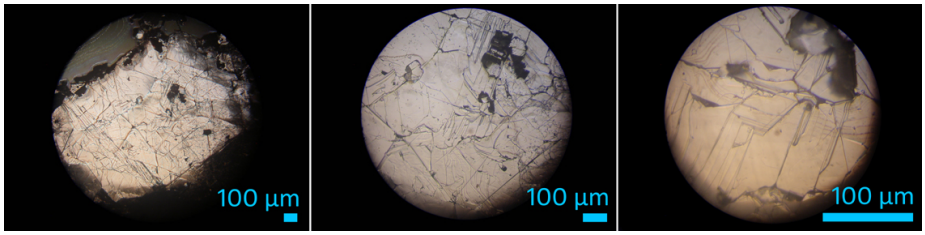

Figure 4.18: Optical microscopy of a kish graphite cleave showing large areas of flat, undisturbed graphite. Images share a common centre.

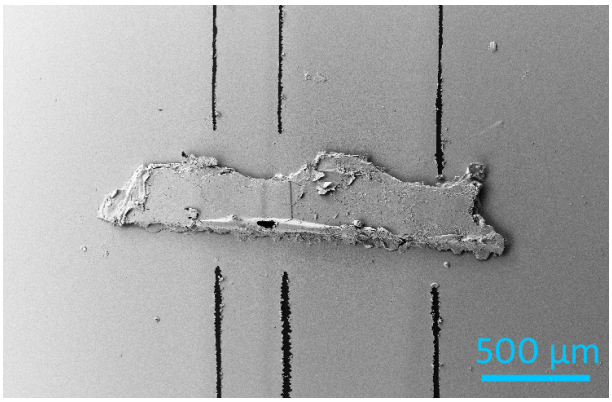

Figure 4.19: SEM image of macroscopic graphite sample mounted on a SiO_2 substrate after gold deposition. Light areas are gold, dark lines are regions from which deposited gold has been mechanically removed to electrically separate contacts.

Stack Device	Length $(mm)^*$	Width $(\mu m)^*$	Thickness $(\mu m)^*$
A	2.0 ± 0.1	290 ± 20	18 ± 5
B	2.3 ± 0.1	240 ± 20	25 ± 5

Table 4.2: Dimensions of the graphite samples after macroscopic preparation. $^*\pm$ represents variation in dimension across sample as seen under SEM imaging, not uncertainty.

Evaporated gold was used to make electrical contact to each graphite piece. An Edwards A306 bell jar evaporator was used to deposit $\sim 600\,nm$ thickness of gold onto each sample and SiO_2 substrate. After deposition, separate contacts were formed by removing the deposited gold from inter-contact regions. This was achieved using a glass rod pulled to a sharp point and attached to the hydraulic arm of a micro-manipulator being dragged across the surface in strong contact - this accounts for the jagged edges visible in SEM images of the deposited gold (figure 4.19). The separation of contacts was later completed by FIB milling of the inter-contact gold on the graphite surface, to form four distinct contacts. (Initially, masked deposition was attempted but it was found that the masking did not ensure complete contact separation).

After completion using FIB milling the electrical contacts were assessed simply, using a two-point digital multimeter to measure resistance. Between multimeter probes the resistance was $0.3\,\Omega$. Between different areas of a single contact pad the resistance was $0.5\,\Omega$. Between adjacent, separated contact pads (with current running through the

bulk graphite sample) resistance was $1.0\,\Omega$.

4.4.3 Focused Ion Beam Milling

Each microscopic stack device was formed by FIB milling of the macroscopically prepared samples. FIB produces and directs a stream of high-energy ionised gallium atoms (Ga^{+}), focuses them using electric fields and directs them onto the sample for both milling and imaging. In this work a Carl Zeiss 1540 Crossbeam system was used (figure 4.20). The system comprises a Gemini SEM column from Carl Zeiss with an add-on Orsay Physics Canion 31 FIB column. These beams have a common vacuum space and hence high-resolution SEM imaging can be used to position the sample for FIB milling, reducing the sample surface damage caused by prolonged FIB imaging [155].

The ultimate resolution of the SEM is $1.1\,nm$ at $20\,kV$; $7\,nm$ at $30\,kV$ for the FIB. When imaging/milling micron-scale features the accuracy with which features can be resolved/defined is limited by the magnification and focus. In practice, for this work this means a best accuracy of $\sim \pm 1\,\%$.

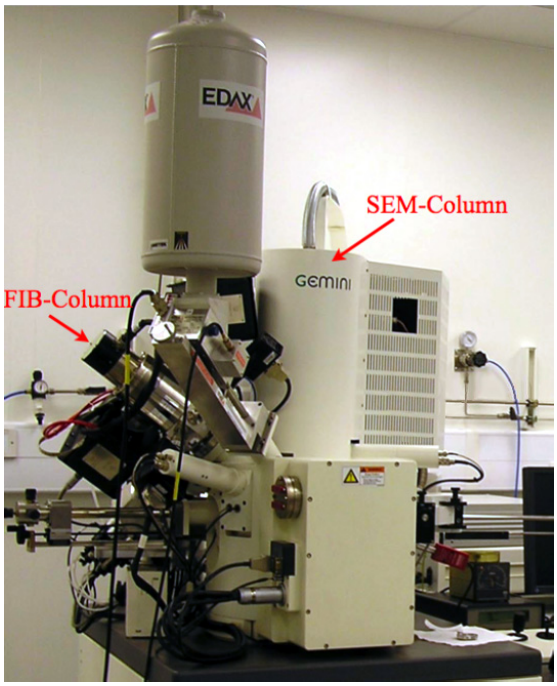

Figure 4.20: The Carl Zeiss XB1540 Cross-Beam SEMFIB.

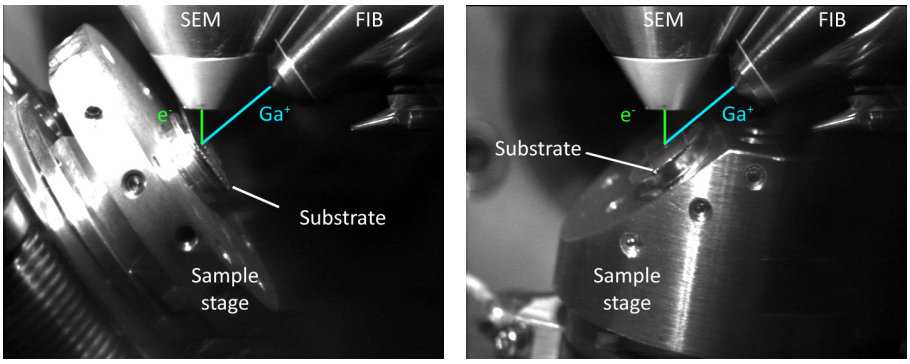

Figure 4.21: View inside the vacuum chamber of samples mounted on flat stage for top-down (left) and angled stage for lateral milling (right) showing SEM and FIB gun positions.

The sample to be milled was secured on a metal SEM pin and one gold contact grounded to the pin with silver paint (Agar Scientific G3648). This increases the accuracy of the SEM and FIB beams by reducing electrostatic sample charging which can otherwise cause the beams to deflect. For top-down milling the pin was mounted on a standard flat stage (left panel of figure 4.21) and loaded into the vacuum chamber. An angled stage (right panel of figure 4.21) was used for lateral cuts.

The following details the specific FIB milling process used to create the stack devices, shown in overview in figure 4.22. Unless otherwise stated milling was performed at a current of $50\,pA$ and a voltage of $30\,kV$.

- Figure 4.22, step (a): The sample and substrate were angled such that they were perpendicular to the FIB beam. Two long, offset trenches each $15\,\mu m$ wide were milled through the sample to the substrate parallel to the short axis of the sample, leaving a $\sim\ 20\,\mu m$ section of undisturbed graphite between them (left panel of figure 4.23). A third $15\,\mu m$ wide trench was milled parallel to the long axis between these, giving two potential device sites. Further trenches were milled to define $50\,\mu m$ long current paths in which to form the device. Initially (stack device A) a total of three $15\,\mu m$ wide trenches were cut to allow two distinct current channels for the two potential device sites. Later (stack device B) trench positions were reconfigured such that only two trenches were cut leaving one current path but still two options.

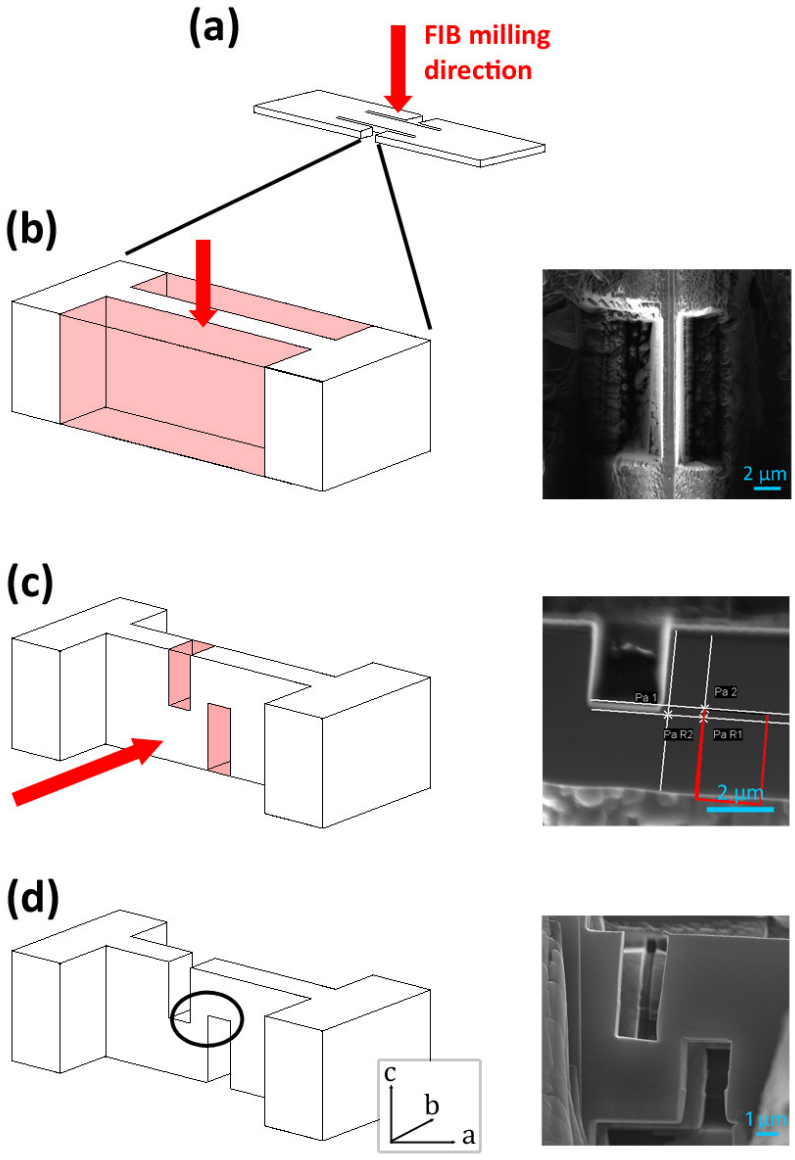

Figure 4.22: Schematic representation of FIB milling process to form stack devices. (a) Initial top down milling narrows the $\sim 300\,\mu m$ wide sample to several microns and defines a target device region; (b) the target region is further narrowed to a width of $1\,\mu m$; (c) the sample is repositioned such that the FIB beam is parallel to the substrate and two lateral cuts are made, leaving an undisturbed region of $1\,\mu m$ x $1\,\mu m$ in between; (d) the lateral cuts overlap by a height of $230\,nm$ (device A) and $290\,nm$ (device B) creating the stack device in the circled area.

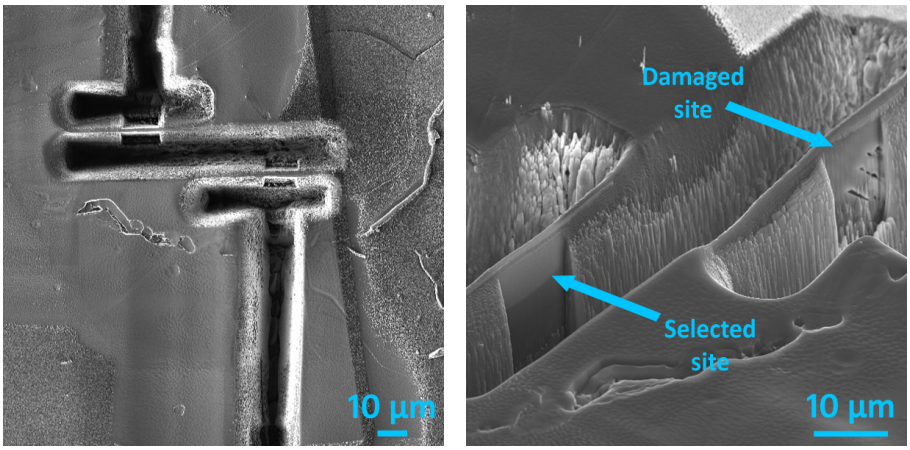

Figure 4.23: Overview (left) and close-up (right) of stack device A after major cuts, at the point of site selection.

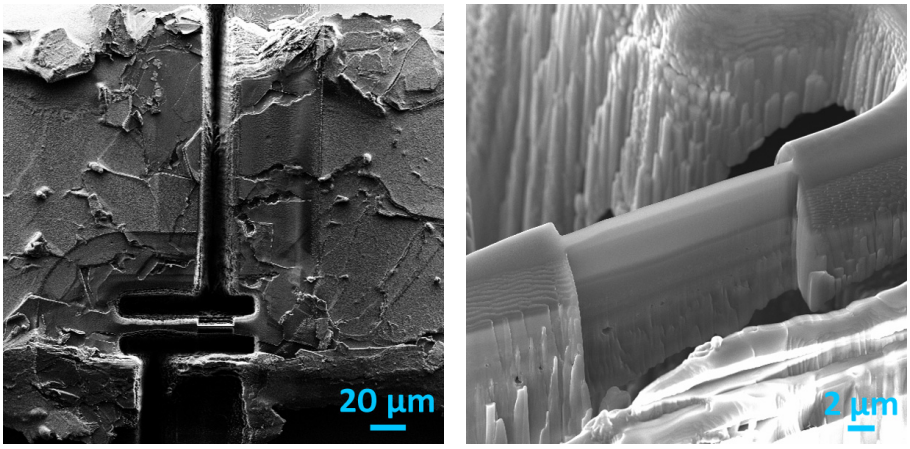

Figure 4.24: Overview (left) and close-up (right) of stack device B after major cuts.

- Figure 4.22, step (b): Both SEM and FIB imaging were used to choose the better potential device site for each sample. Selection was made based on the uniformity and undisturbed nature of the graphite at each site. For stack device A, with two independent current paths, both available sites could be milled further without detrimental effects and the site decision delayed. Chosen device sites were thinned on both sides by FIB milling to a width of $1\,\mu m$. This milling was begun at $500\,pA$ with the current then reduced in stages to $20\,pA$ to allow more precision approaching the desired width of $1\,\mu m$. At this point for stack device A it became apparent that one site was damaged (right panel of figure 4.23) so it was milled through to leave only one current path. For stack device B the selected site is shown in figure 4.24.

- Figure 4.22, step (c): The sample and substrate were then remounted on the angled stage and rotated such that the FIB beam was parallel to the substrate and pointing along the short axis trench directly at the device site (figure 4.25). The bottom of the device site was milled away to create a 'bridge' over the substrate as the only conducting path. Two vertically overlapping cuts ($20\,pA$, $30\,kV$) were made through the bridge leaving a section between them $1\,\mu m$ x $1\,\mu m$ in-plane and $230\,nm$ (device A) and $290\,nm$ (device B) in height.

- Finally, any sections of graphite or gold between the macroscopic contacts were removed to ensure that the four electrical contacts were independent.

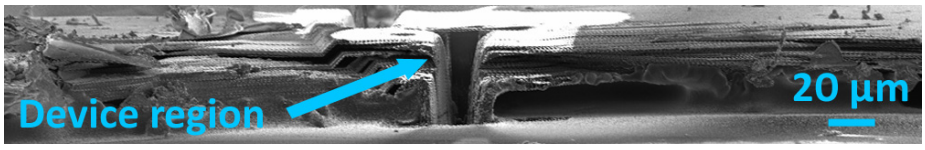

Figure 4.25: FIB view of stack device A during lateral milling.

4.4.4 Device Details

The above processing resulted in several functional devices. Stack devices A and B are detailed immediately below and are the subject of this thesis. Several other devices in graphite, CaC_6 and $NbSe_2$ failed in testing and these are described briefly in 'Other Devices'.

4.4.4.1 Stack Device A

Figure 4.26 shows the finalised stack device A. The dimensions of the c-axis transport region are $1.08 \pm 0.01\,\mu m$ x $1.09 \pm 0.01\,\mu m$ in-plane and $230 \pm 10\,nm$ in height, as measured by the SEM.

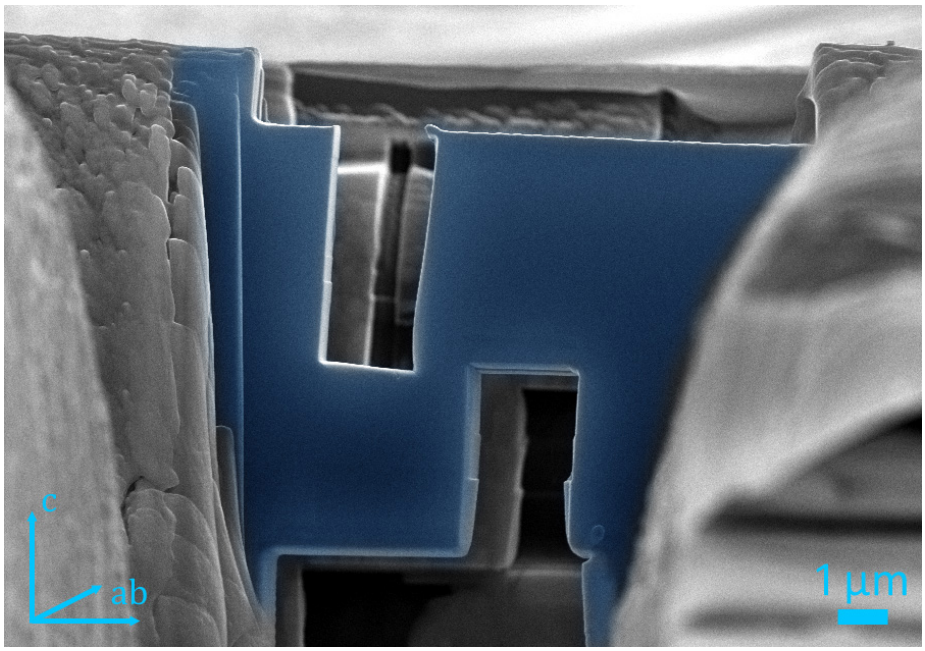

Figure 4.26: False-colour SEM image of stack device A viewed along the lateral cut.

4.4.4.2 Stack Device B

Figure 4.27 shows the finished stack device B. The final dimensions of the c-axis transport region were $1.07 \pm 0.01\,\mu m$ x $1.03 \pm 0.01\,\mu m$ in-plane and $290 \pm 10\,nm$ in height.

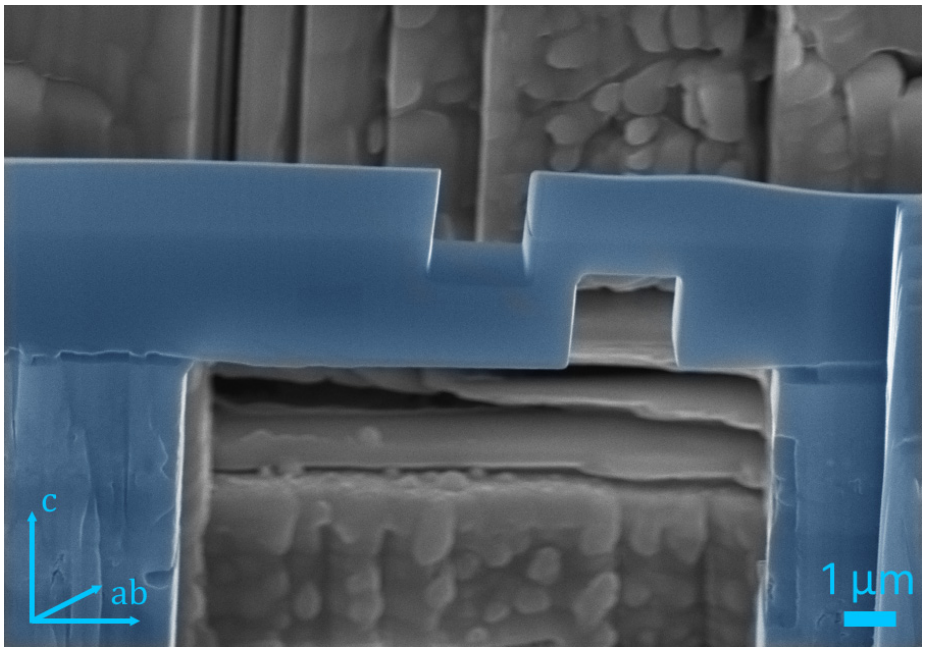

Figure 4.27: False-colour SEM image of stack device B.

4.4.4.3 Other Devices

Several other devices were fabricated from graphite, CaC_6 and $NbSe_2$, but for various reasons they yielded no usable data. These devices are detailed here for the reference of those attempting similar processing.

One further graphite device was fabricated using the same processes as detailed above and is shown in figure 4.28. However, it suffered a shear fracture in the final stage of preparation.

Two devices were created from CaC_6 with the aim of studying the superconducting [52] and CDW states (see chapter 3). In both cases the macroscopic preparation, gold deposition and milling processes were completed successfully and the samples loaded into the cryostat. Due to the reactivity of CaC_6 with moisture and oxygen in the air each step was performed under argon to prevent destructive reactions. The device shown in the left panel of figure 4.29 had a resistivity consistent with CaC_6 in the normal state and showed the CaC_6 superconducting transition at $11.5\,K$ [52]. However, reaction between the CaC_6 and the silver epoxy used to make electrical contact caused its degradation and failure after only preliminary tests had been performed. The second

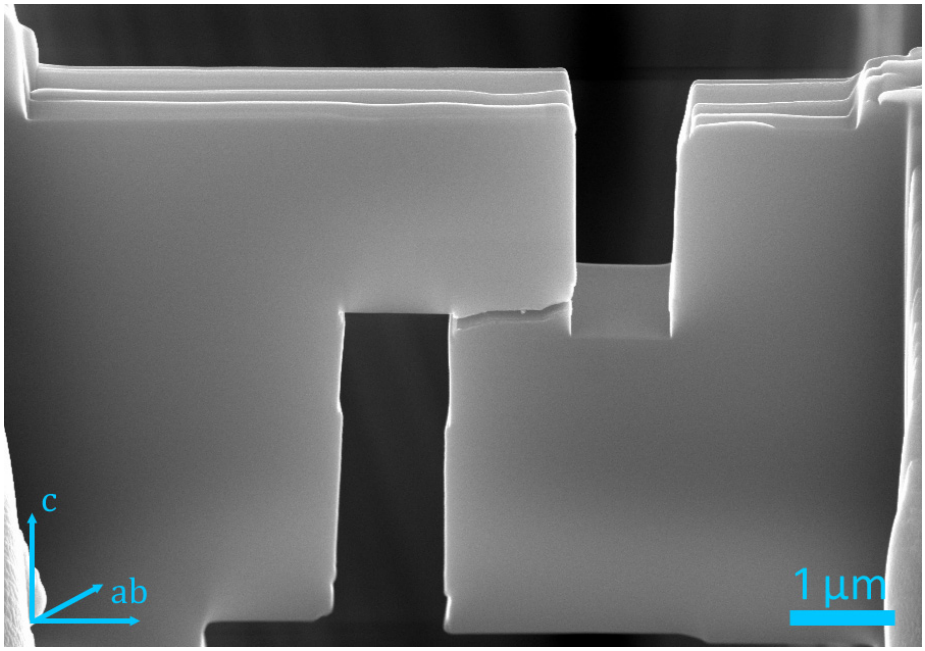

Figure 4.28: Additional graphite-based stack device showing a shear fracture at the stack site.

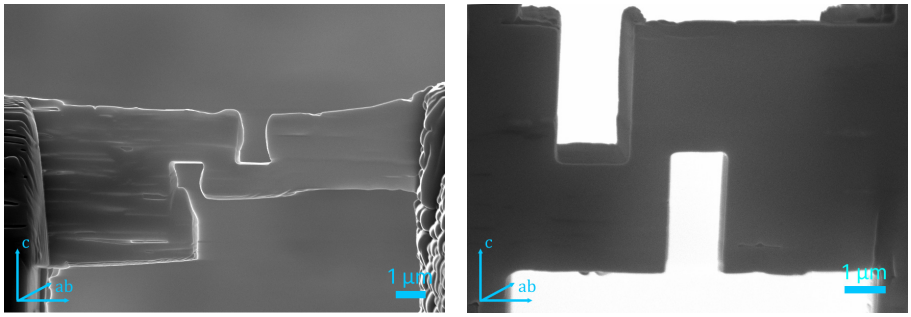

Figure 4.29: Two devices fabricated from CaC_6 precursors.

device (right panel of figure 4.29) had a high temperature resistivity consistent with unintercalated graphite, indicating that the device had been created too deeply within an only superficially intercalated CaC_6 precursor.

A final device was created from an $NbSe_2$ crystal, again with the aim of studying the superconducting [133] and CDW states [156]. Preliminary low current testing in the cryostat was performed and the $7\,K$ superconducting transition was observed. On increasing current to levels comparable with those used for graphite devices the $NbSe_2$ device burnt out due to Joule heating in the narrow stack region.

4.4.5 Electrical Measurement Setup

The completed FIB samples were mounted on a chip carrier using GE varnish and electrically connected to the chip pins using copper wire in a four-point configuration secured by silver epoxy (Epotek E4110) cured at $\sim\ 100\,^oC$. The chip carrier was inserted into the socket on the probe of the Oxford Instruments MagLab measurement system. For variable temperature measurements the probe was mounted in the central vacuum space of an Oxford Instruments ^{4}He cryostat, capable of temperature control between $250\,K$ and $2\,K$.

To measure the IV characteristics of the devices current was supplied by a Keithley 6221 AC/DC current source operating in DC mode and voltage measured using a Keithley 2182A nanovoltmeter, both under the control of LabView software written for this work. The current source was used exclusively in the $100\,mA$ range in which it has an accuracy of $0.1\,\%$ (e.g. $\pm 50\,\mu A$ at $50\,mA$).

For each measurement the temperature was stabilised to within $\leq\ 0.1\,K$ before the current was stepped from $-100\,mA$ to $+100\,mA$ in $2\,mA$ increments. Each current value was held for $500\,ms$ before a voltage measurement was made to ensure good temperature control in case of localised Joule heating. Each voltage reading was averaged over five power line cycles, resulting in very good repeatability in the voltage readings at all currents (e.g. $0.02\,\%$ variation in V at $50\,mA$ at $2\,K$).

Two methods were used to study the behaviour of the resistance as a function of temperature of the devices: DC measurement derived from IV characteristics and AC measurement at a single current.

DC values of resistance as a function of temperature were derived from the above described IV measurements as the gradient of a linear fit to a plot of $V(I)$. This fitting procedure typically resulted in an error of $< 0.01\,\%$ in the fitted resistance value.

Detailed measurement of the resistance of device A was performed using the AC resistance measuring function and automated temperature control of the Oxford Instruments MagLab system (details of which can be found in the relevant manuals, available from Oxford Instruments). The device temperature was swept at a rate of $1.8\,K/min$ and an AC current of $50\,mA$ at a frequency of $10\,Hz$ was used, resulting in variation of $\sim 1.5\,\%$ in resistance readings at all temperatures

Measurements were performed on each device in turn to the point of physical failure.

4.5 Results

4.5.1 Stack Device A

Figure 4.30 shows the IV characteristics of stack device A between $246\,K$ and $2\,K$. IVs at all temperatures appear linear demonstrating the good overall quality of the electrical contacts. Gradients steepen with decreasing temperature showing that resistance decreases with decreasing temperature showing the presence of predominantly metallic conduction.

Conductance, numerically calculated as $\frac{dI}{dV}$ from IV characteristics, is shown in figure 4.31. Low temperature curves show the presence of gap-like structures around zero bias. In all curves minor background curvature is seen likely resulting from slight contact imperfections, while at the highest temperatures some asymmetric variation is seen. This high temperature variation is consistent with the temperature control response of the system and is not seen in curves below $134\,K$.

Figure 4.32 shows the detailed resistance-temperature behaviour of this device between $250\,K$ and $2\,K$, confirming overall metallic conduction.

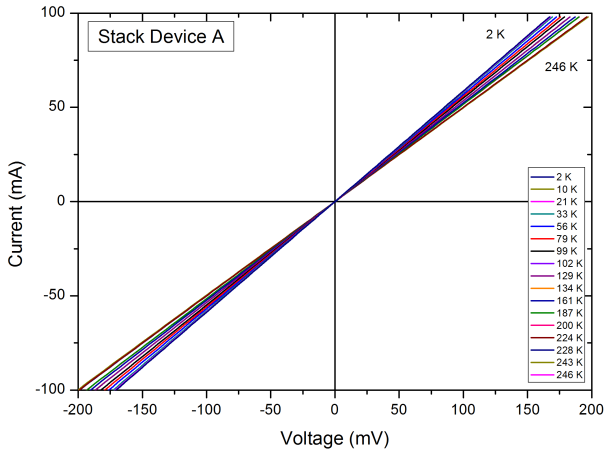

Figure 4.30: IV characteristics for stack device A between $246\,K$ and $2\,K$.

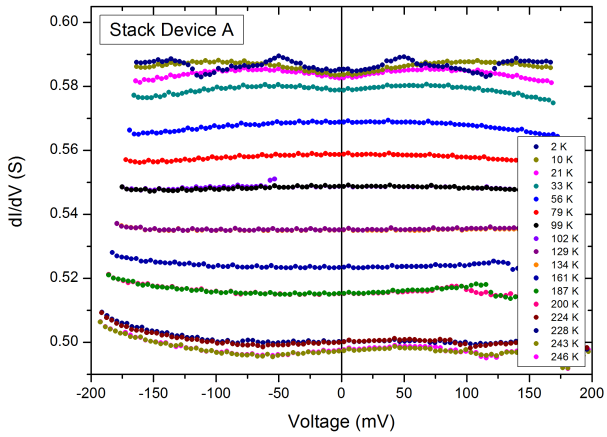

Figure 4.31: Numerical $\frac{dI}{dV}$ for stack device A between $246\,K$ and $2\,K$. Values calculated from IV characteristics shown in figure 4.30.

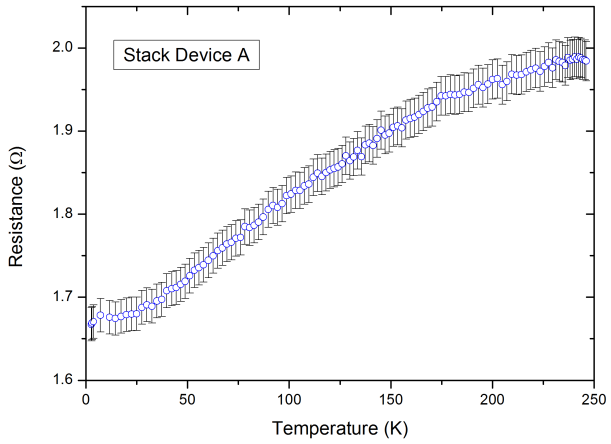

Figure 4.32: Resistance as a function of temperature for stack device A between $250\,K$ and $2\,K$.

4.5.2 Stack Device B

Figure 4.33 shows the IV characteristics of stack device B between $200\,K$ and $4\,K$. IVs at all temperatures are again linear demonstrating the good overall quality of the electrical contacts.

Numerically calculated conductance $\frac{dI}{dV}$ is shown in figure 4.34, as derived from IV characteristics shown in figure 4.33. A slight curvature of all curves is again present, while the low temperature features exhibited by stack device A are not observed.

Figure 4.35 shows the resistance-temperature behaviour of this device between $200\,K$ and $4\,K$ as extracted from the gradient of the IV characteristics. With decreasing temperature device resistance shows a rise to a broad peak at $\sim 130\,K$ followed by a metallic decrease to low temperatures.

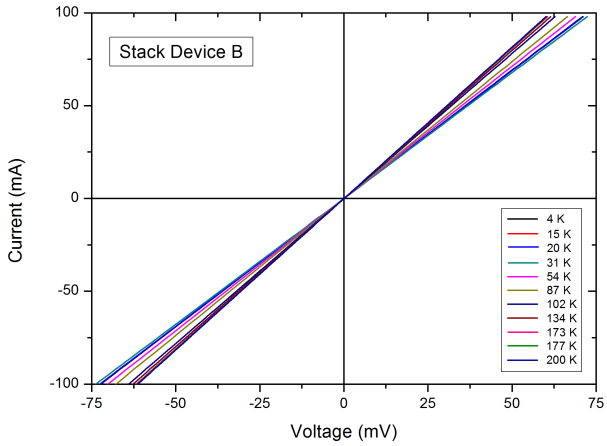

Figure 4.33: IV characteristics for stack device B between $200\,K$ and $4\,K$.

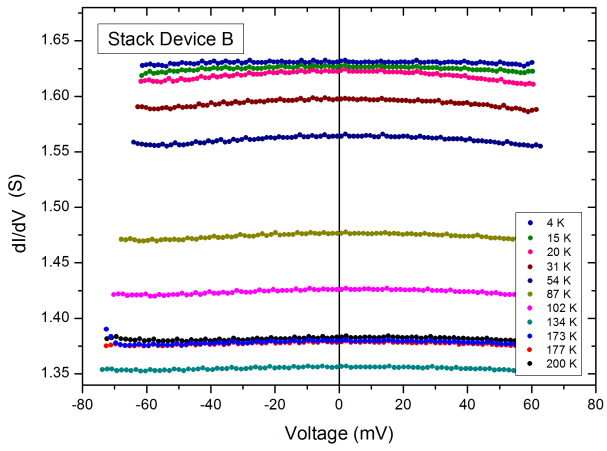

Figure 4.34: Numerical $\frac{dI}{dV}$ for stack device B between $200\,K$ and $4\,K$. Values calculated from IV characteristics shown in figure 4.33.

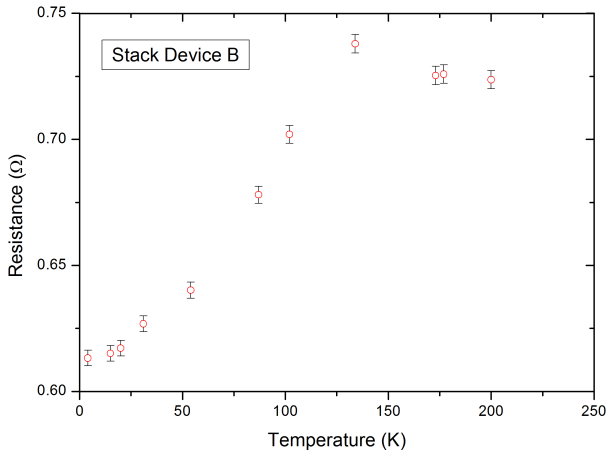

Figure 4.35: Resistance as a function of temperature for stack device B between $200\,K$ and $4\,K$. Resistance values are calculated as the inverse gradient of the IV characteristics shown in figure 4.33.

4.6 Discussion

4.6.1 Size Effects in Graphitic Stack Devices

Figures 4.26 and 4.27 show SEM images of the device regions of devices A and B, respectively. From the figures it appears clear that no continuous ab-plane current path exists through the device region. The electrical test current must, therefore, travel along the graphitic c-axis at the device and as such both devices should exhibit an interlayer-type $R(T)$ behaviour. However, this is not evident in the $R(T)$ graphs shown in figures 4.32 and 4.35. The reasons for this are discussed below.

Two important features are evident in the plots of $R(T)$ for devices A and B (figures 4.32 and 4.35, respectively) relating to the overall magnitude of the resistance and to its temperature dependence. On the first point, in device A the low temperature resistance $R(2K) = 1.66\,\Omega$ and the high temperature resistance is $R(250\,K) = 1.98\,\Omega$, while in device B $R(2\,K) = 0.61\,\Omega$ and $R(250\,K) \sim 0.71\,\Omega$ (estimated from a linear fit to $R(T > 130\,K)$). Given that the difference in the dimensions between the devices is very small these differences in R cannot be explained by sample size as per equation 4.8, which relates R and ρ. On the second point, device A shows a purely metallic temperature dependence reminiscent of conduction in the ab-plane, although SEM images

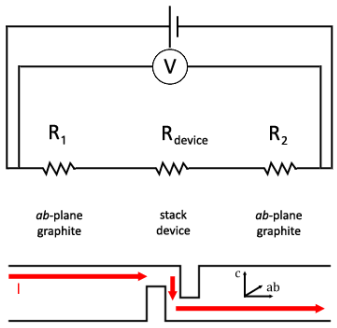

Figure 4.36: Schematic representation of the series combination of the resistance due to the device (R_{device}) with that of the ab-plane leads where $R_{leads}(T) = R_1(T) + R_2(T)$.

of the device (figure 4.26) clearly shows that the electrical test current must cross planes along the c-axis in the device region. In addition, the RRR for such purely ab-plane conduction at $\frac{R(250\,K)}{R(2\,K)} = 1.2$ implies an unrealistically high defect concentration. Device B shows a similar metallic dependence to device A up to $\sim 130K$, however above this temperature $\frac{dR}{dT}$ becomes negative. This shows that similar mechanisms to those of device A are likely to predominate at lower temperatures while at higher temperatures behaviours differ.

To this point it has been assumed that the difference in magnitude between ρ_{ab} and ρ_c (as found by macroscopic measurements) would mean that the total resistance R_{total} would be dominated by the contribution of the c-axis device region, while any resistance from the ab-plane 'lead' sections would be negligible. Given the presence of a clear ab/metallic contribution in $R(T)$ of both devices this assumption should be questioned.

To assess the likely magnitude of any contribution from the ab/metallic leads to $R_{total}(T)$ the system is modelled as a series combination of the leads and the device itself (figure 4.36), the total resistance then being described by:

$$R_{total}(T) = R_{leads}(T) + R_{device}(T) \tag{4.16}$$

where

$$R_{leads}(T) = R_1(T) + R_2(T)$$

For device A, taking the temperature dependent part of the measured R_{total} (i.e. $\Delta R = R_{total} - R(2\,K)$) and scaling by the dimensions of the leads using equation 4.8 yields

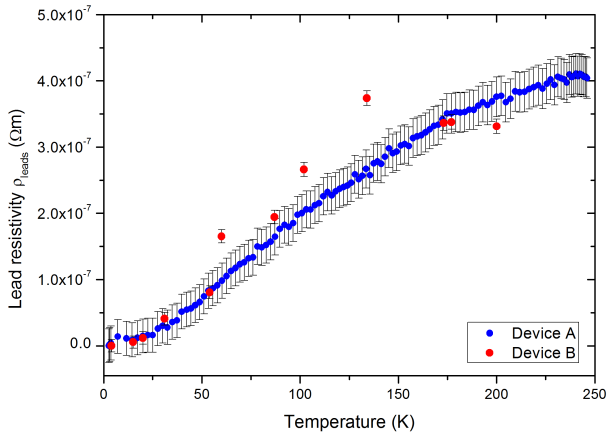

Figure 4.37: Estimated resistivity of lead sections of devices A and B. Device A shows a metallic behaviour at all temperatures ($\frac{d\rho}{dT} < 0$) while device B has $\frac{d\rho}{dT} < 0$ at low temperatures but for $T \gtrsim 140\,K$ $\frac{d\rho}{dT} > 0$ showing an additional contribution. Resistivity is calculated as $\rho_{leads} = [R(T) - R(2\,K)]\left[\frac{A_{lead}}{l_{lead}}\right]$.

the blue points shown in figure 4.37. Comparison to figure 4.2 shows that both the overall magnitude, at $\sim 10^{-7}\,\Omega m$, and temperature dependence match very closely those of ab-plane graphite. This in turn implies via equation 4.16 that $R_{device} \sim constant = R(2\,K) = 1.66\,\Omega$ over the measured temperature range. Taking the same line of reasoning for device B results in the red points in figure 4.37. The approximate agreement of the magnitude and behaviour for $T \lesssim 130\,K$ demonstrates that both devices feature a resistance contribution from the ab-plane leads, with the device B leads being more resistive. Above $\sim 130\,K$, therefore, the drop off in the resistance of device B must signify a decrease in R_{device}.

The absence of a temperature dependence to R_{device} for device A at all temperatures and for device B for $T \lesssim 130\,K$ suggests a different conduction mechanism is operating in the devices compared to the Ohmic conduction in the leads. The Knudsen-Sharvin equation (equation 4.11) describes the resistance arising from a short conducting constriction between two Ohmic conductors as:

$$R_{KS} = \frac{4\rho(T)\lambda_{MFP}(T)}{3A} + \Gamma(k)\frac{\rho(T)}{W}$$

where $\rho(T)$ is the resistivity of the conductor; $\lambda_{MFP}(T)$ is the mean free path; A is the cross-sectional area of the constriction; $\Gamma(k)$ is a smoothly varying geometrical factor;

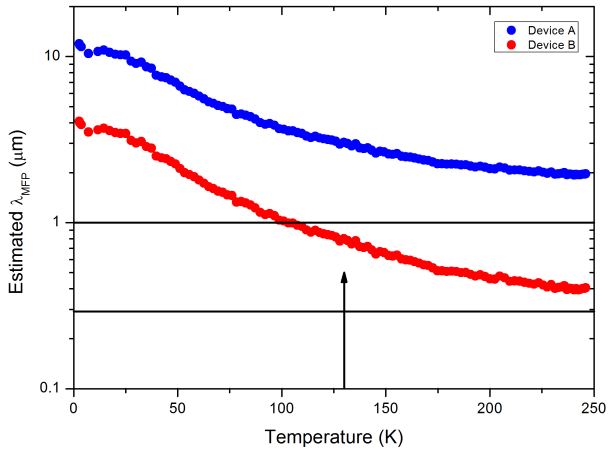

Figure 4.38: Estimated mean free path for devices A and B. Black horizontal lines are positioned at the device width of $W = 1\,\mu m$ and average device c-axis height of $h_c = 290\,nm$. Black arrow is positioned at $130\,K$, the temperature at which R_{device} for device B begins to decrease.

W is the width of the constriction.

Considering each device region as a constriction between bulk conductors with resistivity as calculated in figure 4.37, the following calculation can be performed to estimate the mean free path. Taking the resistivity of the lead sections of device A (figure 4.37) with an additional estimated residual resistivity of $1 \times 10^{-7}\,\Omega m$ (i.e. $\rho(T) = \rho_{leads}(T) + 1 \times 10^{-7}\,\Omega m$), with the device parameters $A = 1\,\mu m^2$, $W = 1\,\mu m$ and $\Gamma(k) = 0.67$ and device resistances $R_{KS} = R_{device\,A} = 1.66\,\Omega$ and $R_{KS} = R_{device\,B} = 0.61\,\Omega$ yields estimates for the mean free path $\lambda_{MFP}(T)$ as shown in figure 4.38.

Figure 4.38 shows that for device A λ_{MFP} remains greater than both W and h_c at all temperatures, meaning that transport through the device is always ballistic. However, for device B λ_{MFP} is smaller at all temperatures and falls below W at $T \sim 100\,K$. In this sense the divergence observed in the $R(T)$ behaviour of the two devices at $\sim 130\,K$ is explained as a transition from ballistic to more Ohmic behaviour in device B as λ_{MFP} becomes comparable to W and h_c.

These findings of ballistic transport contributions are in agreement with recent work by Dusari [55] which observed ballistic transport through micron-sized constrictions in ab-plane HOPG at room temperature i.e. $\lambda_{MFP}(300\,K) > 1\,\mu m$. In agreement with the above description the $R(T)$ behaviour observed was heavily modified by the presence of the constriction from a typical ab-plane dependence to one which showed a negative

$\frac{\partial R}{\partial T}$ for $100\,K \lesssim T \lesssim 300\,K$ and $R \sim constant$ for $T \lesssim 100\,K$. Similarities between the $R(T)$ behaviour observed by Dusari and that seen in the stack device of Latyshev [39] are discussed below in section 4.6.3.

4.6.2 Pseudogaps in Graphitic Stack Devices

Figures 4.31 and 4.34 show the behaviour of the conductance as a function of temperature for devices A and B, respectively. For device B conductance $\frac{dI}{dV}(V)$ is constant at each temperature showing a purely metallic behaviour. Device A shows a similar metallic dependence at higher temperature but for $T \lesssim 56\,K$ a gap-like feature emerges. This feature becomes more prominent with decreasing temperature and further features develop at the lowest temperatures. Figure 4.39 shows the temperature dependence of $\frac{dI}{dV}(V)$ for device A with $T \leqslant 56\,K$.

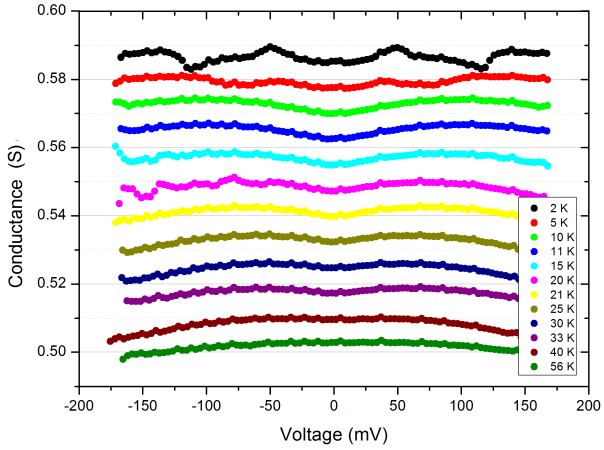

Figure 4.39: Conductance of device A as a function of voltage for $T \leq 56\,K$ showing the development of the pseudogap centred at zero bias. Curves have been vertically offset for ease of viewing but share a common scale.

As shown in figure 4.39 several features are evident in $\frac{dI}{dV}(V)$: a broad overall curvature at all temperatures, a growing central pseudogap and complex low temperature features. These are treated in turn below.

The continuous, broad curvature seen at all temperatures is likely due to a degree of non-Ohmic behaviour in the macroscopic electrical contacts. The curvature evolves smoothly with temperature, becoming flatter with decreasing temperature in the range

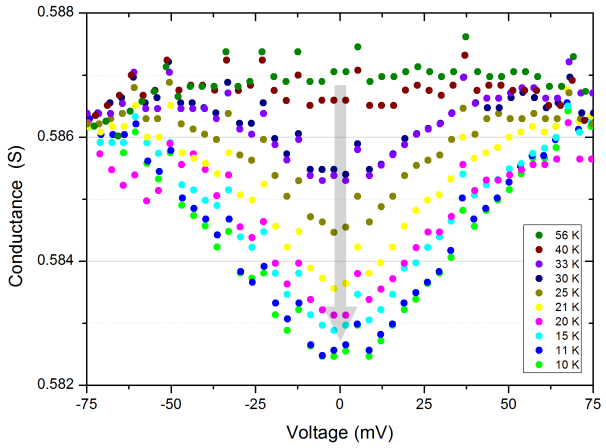

Figure 4.40: Low voltage region of the conductance of device A as a function of voltage for $10\,K \leq T \leq 56\,K$ showing the development of the pseudogap centred at zero bias. Grey arrow indicates decreasing temperature. Curves have been vertically offset for ease of viewing but share a common scale.

$-200\,mV \leq V \leq 200\,mV$. At low voltages ($-75\,mV \leq V \leq 75\,mV$) this background is approximately flat at all temperatures. This behaviour is also seen in device B (figure 4.34).

The second feature of $\frac{dI}{dV}(V)$, and the most prominent, is the pseudogap centred at zero-bias. Figure 4.40 shows the evolution of this pseudogap with temperature in the central voltage independent background region at low voltages ($-75\,mV \leq V \leq 75\,mV$). At $40\,K$ the gap becomes evident as a slight dip in the wider background curve, becoming more prominent with decreasing temperature down to $10K$. Figure 4.41 shows the conductance curve at $10\,K$. The voltage dependence of the conductance is clearly parabolic, flattening towards a constant value at higher voltages. As such a fit to a Coulomb gap is appropriate, as described below.

Equation 4.15 showed that the conductance of a metal is proportional to its DOS and equation 4.12 described the DOS of a system with a Coulomb gap. Given the hybrid and additive nature of the device as described above, this direct relationship between conductance and DOS must be treated qualitatively with a fitting equation used which accounts for these complexities. With these caveats in mind equation 4.17 is fitted to the data for $T \leq 56\,K$.

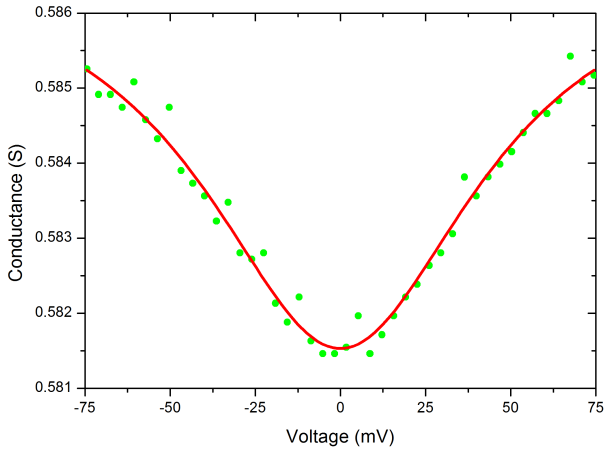

Figure 4.41: Low voltage conductance of device A at 10K. Red line is a fit to equation 4.17 with parameters $G_0 = 0.58153 \pm 0.00007\,S$, $m = 2.2 \pm 0.2$ and $E_C = 49 \pm 3\,mV$.

$$\frac{dI}{dV}(V) = G_0 + m\left(\frac{E_C^2 V^2}{E_C^2 + V^2}\right) \tag{4.17}$$

Here, G_0 describes the overall temperature dependence of the conductance in line with the arguments laid out above. m is a parameter composed of many factors including the graphitic DOS at the Fermi level and any tunneling probability elements. It is not possible to decompose G_0 and m into their constituents because of the hybrid nature of the device. E_C describes the pseudogap size.

As demonstrated by figure 4.41 using the $10\,K$ data as an example equation 4.17 describes data very well, here with parameters $G_0 = 0.58153 \pm 0.00007\,S$, $m = 2.2 \pm 0.2$ and $E_C = 49 \pm 3\,mV$. Parameters of fits to this equation for $\frac{dI}{dV}(V)$ at $10\,K \leq T \leq 56\,K$ are given in table 4.3.

As shown in table 4.3 values of the zero voltage conductance G_0 increase with decreasing temperature, in agreement with the behaviour of $R(T)$ shown in figure 4.32. The constant of proportionality m is approximately equal at all temperatures. The pseudogap size E_C grows with decreasing temperature as can be seen in the plot of $E_C(T)$ shown in figure 4.42. It first becomes evident in the fit with a size $E_C = 23 \pm 4\,mV$ at $33\,K$ and approximately doubles in size to $E_C = 49 \pm 3\,mV$ at $10\,K$.

To this point the behaviour of the conductance with $T \geq 10\,K$ has been discussed. Below $10\,K$ the conductance becomes more complex - figure 4.43 shows the conduc-

$T(K)$	$G_0(S)$	m	$E_C(mV)$
56	0.56873 ± 0.00005	0	–
40	0.57175 ± 0.00004	0	–
33	0.5788 ± 0.0001	3 ± 1	23 ± 4
30	0.5769 ± 0.0001	3 ± 1	21 ± 4
25	0.5790 ± 0.0001	4 ± 1	23 ± 3
21	0.58268 ± 0.00009	3.7 ± 0.6	29 ± 2
20	0.5807 ± 0.0001	3.8 ± 0.8	28 ± 3
15	0.58150 ± 0.00008	2.9 ± 0.3	37 ± 3
11	0.58360 ± 0.00007	2.3 ± 0.2	49 ± 3
10	0.58153 ± 0.00007	2.2 ± 0.2	49 ± 3

Table 4.3: Fit parameters of equation 4.17 to $\frac{dI}{dV}(V)$ of device A for $10\,K \leq T \leq 56\,K$.

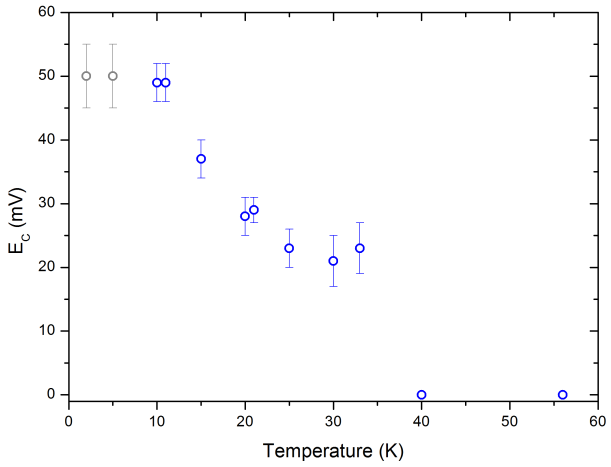

Figure 4.42: Fitted pseudogap size E_C (blue points) as a function of temperature - individual values given in table 4.3. Grey points are estimated values as described in the text.

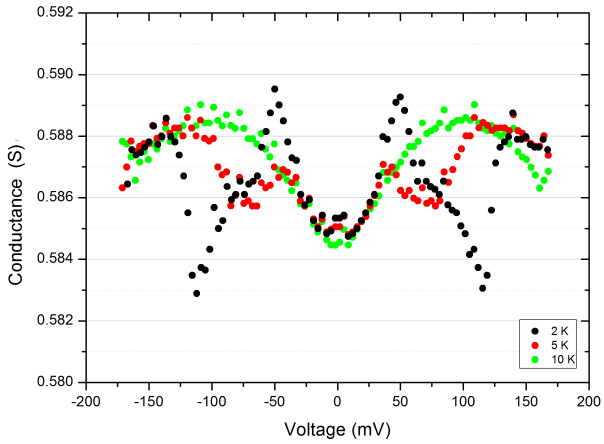

Figure 4.43: Conductance of device A as a function of voltage for $2\,K \leq T \leq 10\,K$ showing the complex gapping at low temperatures. Curves have been vertically offset for ease of viewing but share a common scale.

tance curves at $5\,K$ and $2\,K$ in comparison to the $10\,K$ curve shown above. The figure shows that additional symmetrical features arise in the $5\,K$ and $2\,K$ curves in the range $30\,mV \leq V \leq 130\,mV$. At voltages $V \leq \pm 30\,mV$ and $V \geq \pm 130\,mV$ all three curves coincide suggesting that behaviour in these regions is unchanged from the $10\,K$ case. As such the pseudogap observed at higher temperatures is seen to persist to the lowest temperatures. The sheer complexity of the features at $5\,K$ and $2\,K$ renders accurate fitting of the pseudogap using equation 4.17 impossible, however the equivalence of the curvature around zero bias suggests that the pseudogap size has saturated at the $10\,K$ value of $E_C \sim 50\,mV$ (grey points in figure 4.42).

In the above the observed pseudogap has been well fitted by a Coulomb-like gap. This is in line with the findings of Latyshev [39] in which a pseudogap observed for $T \lesssim 30\,K$ was suggested as being mediated by Coulomb interactions. The Coulomb gap arises from the incomplete screening of Coulomb interactions between localised energy states of electrons and holes. In many systems exhibiting a Coulomb gap these states are localised by high levels of disorder, however given the low values of resistivity found above it is clear that this cannot be the case here. Instead, the electrons in the device region likely become partially localised in the graphene layers constituting the device as the temperature falls. In isolation this localisation of carriers would lead to a significant increase in resistance, however here it appears that ballistic electrons from the lead sections of the device continue to pass through the device, seeing perhaps only a low

potential barrier in the region.

The above explanation of the appearance of the Coulomb-like gap by localisation of electrons onto the graphene planes of the device region in device A suggests that the absence of such an effect in device B is due to a difference in microscopic physical structure. This suggestion is in agreement with the above finding that the ab-plane mean free path in device B is approximately half that of device A. Structural differences which could account for these behaviours include stacking faults, grain boundaries and crystal disorder (e.g. dislocations, impurities). Stacking faults would be unlikely to affect ab-plane resistivity to the observed degree, and would also result in the peak in $R(T)$ at $\sim 50\,K$ characteristic of faulted c-axis transport (figures 4.5, 4.6 and 4.9), which is not observed here. However, low level disorder could be sufficient to both decrease the ab-plane mean free path and also increase coupling between graphene layers in the device region disrupting localisation.

Outside of the pseudogap region in figure 4.43 futher complex behaviour has been observed in the form of a reduction of conductance in both positive and negative bias. These conductance 'dips' are apparent below $10\,K$, in the measurements made at $5\,K$ and $2\,K$. Comparing these two lowest temperature measurements it is clear that the dips evolve with temperature, both deepening and moving to higher voltages at lower temperatures. At present the cause of these conductance dips is unknown, although possible explanations have been examined and discounted. For completeness, these are discussed below: phonon assisted and resonant tunneling.

The geometry of the devices created and tested here is very similar to that used by point contact spectroscopy experiments [157], in that the mean free path is on the order of the contact size between two bulk conductors. In such experiments the transmission of electrons through the contact region is strongly affected by their coupling with phonons, with $\frac{d^2I}{dV^2}$ being proportional to the Eliashberg function. However, the characteristic feature of this interaction is that the voltage position of the conductance peaks does not evolve with temperature as each peak corresponds to a particular phonon mode. The dips in the conductance here are observed to shift with temperature, ruling out this phenomenon.

Resonant tunneling can occur in systems where a conductor with dimensions on the order of the electron de Broglie wavelength λ_{dB} is separated by tunnel barriers from conducting leads either side of it [158]. Work by González [54] has calculated $\lambda_{dB} \sim 1\,\mu m$ in graphite, the same size as the in-plane dimensions of devices A and B. A variant of this effect is the double bend quantum channel (DBQC) [159] which consists

of a conducting channel with two partial, non-conducting blocks across it - the geometry of devices A and B. The narrow conducting paths left by these blocks create potential barriers and define a region between them similar to a quantum dot. Electrons passing through must 'tunnel' in and then out which requires a characteristic energy, producing a peak in the conductance. However, again, the characteristic energy is a constant value, dependent on the 'dot' size and as such does not shift with temperature.

Given the wealth of conductance features observed here and their coexistence it is clear that further experiments must be performed before the causes of each can be explained. Size effects and device geometry are likely to be highly important given the dimensions of the devices with respect to the mean free path and experiments which vary these parameters will go a long way to separating and elaborating upon these fascinating effects.

4.6.3 Measuring c-axis Conduction

A secondary aim of this work is to investigate the behaviour of the c-axis conduction of kish graphite as a function of temperature and compare it to the predicted 'ideal' graphite cases of Ono-Matsubara [40, 34] and Kempa [33]. The advantage of using micron-sized graphite devices to study conduction along the c-axis is that the devices can be fabricated with dimensions smaller than the average crystallite size, meaning that the graphite under test contains no grain boundaries or stacking faults and thus represents the ideal case. However, the interplay between λ_{MFP} and the sample size and geometry strongly affects the measurement and results.

From the measurements made on devices A and B it is clear that the conduction mechanism of the c-axis section of the device has not been found in a way which is consistent with studying macroscopic graphite. This was shown above as being due to λ_{MFP} being large in comparison with the device dimensions at all temperatures, resulting in predominantly ballistic rather than Ohmic transport.

With the above finding in mind the results of previously tested devices can be studied to see whether conduction in those devices constitutes ideal c-axis transport. In the work of Gunasekaran [41] two devices with similar dimensions to those tested here were fabricated from an HOPG precursor. Both devices showed resistance increasing with decreasing temperature to $\sim 50\,K$, with then a metallic behaviour down to the lowest measured temperature of $20\,K$ (figure 4.13). Comparison with the resistance-temperature behaviour of macroscopic samples of HOPG as shown in figure 4.9 demonstrates that the micron-sized devices show macroscopic behaviour and therefore are

likely to contain stacking faults. This is easily motivated by figure 2.5 which shows a TEM image of a representative HOPG sample. The image shows that the c-axis crystallite size is $60 \pm 20\,nm$, significantly smaller than the $100\,nm$ and $200\,nm$ c-axis stack heights of the devices. The IV characteristics of the devices (figure 4.13) also suggest the presence of stacking faults resulting in large potential barriers which cause the tunneling-type curvature seen at higher voltages.

In the work of Latyshev [39] the device presented had dimensions $1\,\mu m$ x $1\,\mu m$ in-plane and $300\,nm$ in height and was formed from a natural graphite precursor. The resistance of the device as a function of temperature (figure 4.12) showed a gradual rise with decreasing temperature, becoming temperature independent below $\sim\ 100\,K$ before a further rise below $30\,K$ concurrent with the opening of a pseudogap. It is possible that the device height was less than the c-axis crystallite size meaning that the measurement could represent ideal c-axis conduction. If so the negative $\frac{\partial R}{\partial T}$ suggests a that the metallic conduction predicted by Ono-Matsubara [40, 34] is incorrect. However, the interpretation of the results for this device is complicated by the findings of Dusari [55] which find a very similar resistance-temperature behaviour for in-plane ballistic transport through a constriction in an HOPG sample. Given the large mean free paths characteristic of natural graphite samples ballistic behaviour of this kind is a distinct possibility and undermines the idea of the Latyshev device as a c-axis measurement.

As discussed above it is unlikely that either of the devices tested here or those of previous studies represent a c-axis measurement of ideal graphite. Whether such a measurement is actually achievable is an open question. It is clear that it cannot be achieved using macroscopic samples but it now also seems unlikely that microscopic samples can yield such a result. If a true characterisation of the c-axis conduction mechanism is to be performed it seems that a sample geometry is required in which the c-axis section under test is longer than the mean free path at all temperatures while being short enough that it contains no faulting; a difficult proposition.

4.7 Summary

FIB micro-machining has been used to create two micron-sized, c-axis stack devices with stack heights $230\,nm$ and $290\,nm$ (devices A and B) from a kish graphite precursor, following previously published work [37, 39]. IV and $R(T)$ measurements between $250\,K$ and $2\,K$ have shown the devices to have a hybrid behaviour with an Ohmic contribution from ab-plane graphitic leads and a ballistic contribution from the device itself.

Ballistic behaviour persists up to at least $250\,K$ in device A while the behaviour of device B changes at $\sim 130\,K$, becoming more Ohmic due to reduction of the mean free path.

A pseudogap observed in device A below $40\,K$ has been well described by a modified Coulomb gap equation. This soft gap was observed to grow with decreasing temperature to a maximum size $E_C(2\,K) = 50 \pm 5\,meV$. Coulomb interactions between carriers localised within the graphene planes constituting the stack device are suggested to be the cause. Further conductance dips have been observed in the same device with unknown cause. It is noted that the gap size is large for a Coulomb gap but that further investigation is greatly complicated by the wealth of conductance features exhibited. Device B is seen to exhibit no gap features due to increased disorder which also contributes to its reduced mean free path.

$R(T)$ results of stack devices A and B and of the similar structures of Latyshev [39] and Gunasekaran [41] have been analysed in the context of Ohmic c-axis conduction in ideal graphite and the models of Ono-Matsubara [40, 34] and Kempa [33]. As noted above, devices A and B were found to exhibit ballistic behaviour, while the devices of Gunasekaran were observed to contain stacking faults, with $R(T)$ behaviour mimicking faulted macroscopic samples. The device of Latyshev was not observed to contain significant faulting and as such the measured $R(T)$ profile showing negative $\frac{dR}{dT}$ for $T \gtrsim 100\,K$ and $R(T) \sim constant$ for $T \lesssim 100\,K$ could represent an ideal measurement. However, it is noted that recent measurements by Dusari [55] of ab-plane transport through micron-sized constrictions in HOPG showed a very similar $R(T)$. As such, it is concluded that ideal c-axis conduction in graphite is yet to be observed.

Given the variation in the results of electrical transport measurements on such similar devices as those here and in [39] and [41] and the inability to present complete explanations it is clear that complex mechanisms are at work. Despite efforts to simplify these devices as much as possible the combination of the geometry, the size with respect to important transport lengths and the inherent structure and defective nature of graphite produces a wealth of features which, while interesting, are difficult to study in combination. It will be a worthwhile challenge to design experiments which can separate and elucidate the many phenomena which intersect in these devices.

Chapter 5

Summary and Next steps

The main, modified objectives of this thesis were to perform electrical transport and heat capacity measurements on $\mathrm{CaC_6}$, graphite and other $\mathrm{MC_6}$ GICs in order to: (i) characterise the superconducting and CDW gaps in $\mathrm{CaC_6}$ and make comparison to similar systems; (ii) provide experimental verification of predicted superconductivity in $\mathrm{BaC_6}$; (iii) provide experimental verification of observed superconductivity in $\mathrm{SrC_6}$, and ; (iv) verify the findings of a pseudogap in graphitic microstructures.

Against the first of these objectives: The superconducting gap in $\mathrm{CaC_6}$ was observed and characterised in heat capacity measurements, with comparison measurements made for $\mathrm{SrC_6}$ and $\mathrm{BaC_6}$. In $\mathrm{CaC_6}$ higher temperature measurements up to $300\,K$ did not observe the CDW transition, indicating T_{CDW} is to be found at still higher temperatures. While superconducting micro-devices were created and superconductivity observed in transport measurements, these devices failed before they could be directed towards any study of the CDW state. Future heat capacity measurements should be performed above $300\,K$ to find T_{CDW}, with electrical transport measurements on micro-samples then used to fully characterise the CDW gap evolution. Higher temperature heat capacity measurements should not present a serious technical challenge, whereas careful experimental design and work will be required to produce electrical transport results.

Measurements of the heat capacity of $\mathrm{BaC_6}$ have observed no superconducting transition down to $\sim 390\,mK$, consistent with previous experimental evidence. In addition, the electron-phonon coupling has been observed to be significantly weaker than predicted by theory at $\lambda_{el-ph} = 0.1$ (vs $\lambda_{el-ph} = 0.38$ in [11]). Coupled with inelastic

x-ray measurements showing the theoretically calculated phonon energies at $\sim 20\,\%$ lower than experimentally observed [9], the next steps here must be to reevaluate the theoretical modelling of $\mathrm{BaC_6}$ such that predictions are consistent with experimental observations.

Measurements of the heat capacity of $\mathrm{SrC_6}$ found $\lambda_{el-ph} = 0.4$ in agreement with theoretical predictions of $\lambda_{el-ph} = 0.54$ [11] but did not observe a previously discovered superconducting transition at $1.65\,K$ [22]. Given the quality and unambiguous nature of previous measurements the negative result seen here should likely not be considered as contradictory to the published results. Instead, the experiment should be repeated with special attention paid to sample preparation and experimental process in order to provide a reliable comparison.

Characterisation of graphitic micro-structures using electrical transport measurements has verified the findings of a pseudogap state in graphite of Latyshev et al [39] in one device. A pseudogap was not observed in another, very similar device. The variation in observations between devices tested here demonstrates their complexity and the need for future focus on the design of experiments which can separate the many phenomena which intersect in these devices.

Bibliography

[1] R.W.G Wyckoff. *Crystal Structures vol. 1*. Interscience Publishers, New York, 1964.

[2] M.S. Dresselhaus and G. Dresselhaus. Intercalation compounds of graphite. *Adv. Phys*, pages 1–186, 2002.

[3] Y. Kaburagi, A. Yoshida, and Y. Hishiyama. Microtexture of highly crystallized graphite as studied by galvanomagnetic properties and electron channeling contrast effect. *Journal of Materials Research*, 11(3):769–778, 1995.

[4] J. Barzola-Quiquia, J.-L. Yao, P. Rödiger, K. Schindler, and P. Esquinazi. Sample size effects on the transport characteristics of mesoscopic graphite samples. *physica status solidi (a)*, 205(12):2924–2933, 2008.

[5] H. Zabel. Phonons in layered compounds. *Journal of Physics: Condensed Matter*, 13(34):7679, 2001.

[6] M. Mohr, J. Maultzsch, E. Dobardžić, S. Reich, I. Milošević, M. Damnjanović, A. Bosak, M. Krisch, and C. Thomsen. Phonon dispersion of graphite by inelastic x-ray scattering. *Phys. Rev. B*, 76(3):035439, 2007.

[7] A. Hagen. *Ladungsträgerdynamik in Kohlenstoff-Nanoröhren*. PhD thesis, Freie Unversität Berlin, 2005.

[8] A.G. Marinopoulos, L. Reining, A. Rubio, and V. Olevano. Ab initio study of the optical absorption and wave-vector-dependent dielectric response of graphite. *Phys. Rev. B*, 69(24):245419, 2004.

[9] A.C. Walters, C.A. Howard, M.H. Upton, M.P.M. Dean, A. Alatas, B.M. Leu, M. Ellerby, D.F. McMorrow, J.P. Hill, M. Calandra, and F. Mauri. Comparative

study of the phonons in non-superconducting BaC_6 and superconducting CaC_6 using inelastic x-ray scattering. *ArXiv e-prints*, 2011.

[10] M. Calandra and F. Mauri. Theoretical Explanation of Superconductivity in C_6Ca. *Phys. Rev. Lett.*, 95(23):237002, 2005.

[11] M. Calandra and F. Mauri. Possibility of superconductivity in graphite intercalated with alkaline earths investigated with density functional theory. *Phys. Rev. B*, 74(9):094507, 2006.

[12] M. Tinkham. *Introduction to Superconductivity, Second Edition*. McGraw-Hill, New York, 1996.

[13] G. Grüner. The dynamics of charge-density waves. *Rev. Mod. Phys.*, 60(4):1129–1181, 1988.

[14] J.M.E. Harper, T.H. Geballe, and F.J. DiSalvo. Thermal properties of layered transition-metal dichalcogenides at charge-density-wave transitions. *Phys. Rev. B*, 15(6):2943–2951, 1977.

[15] R.S. Kwok, G. Gruner, and S.E. Brown. Fluctuations and thermodynamics of the charge-density-wave phase transition. *Phys. Rev. Lett.*, 65(3):365–368, 1990.

[16] A.M. Gabovich, A.I. Voitenko, T. Ekino, M. Suan Li, H. Szymczak, and M. Pekala. Competition of superconductivity and charge density waves in cuprates: Recent evidence and interpretation. *Advances in Condensed Matter Physics*, page 681070, 2010.

[17] J.S. Kim, R.K. Kremer, L. Boeri, and F.S. Razavi. Specific Heat of the Ca-Intercalated Graphite Superconductor CaC_6. *Phys. Rev. Lett.*, 96(21):217002, 2006.

[18] L. Boeri, G.B. Bachelet, M. Giantomassi, and O.K. Andersen. Electron-phonon interaction in graphite intercalation compounds. *Phys. Rev. B*, 76(6):064510, 2007.

[19] I.I. Mazin, L. Boeri, O.V. Dolgov, A.A. Golubov, G.B. Bachelet, M. Giantomassi, and O.K. Andersen. Unresolved problems in superconductivity of CaC_6. *Physica C: Superconductivity*, 460-462(Part 1):116 – 120, 2007.

[20] N. Bergeal, V. Dubost, Y. Noat, W. Sacks, D. Roditchev, N. Emery, C. Hérold, J-F. Marêché, P. Lagrange, and G. Loupias. Scanning Tunneling Spectroscopy on the Novel Superconductor CaC_6. *Phys. Rev. Lett.*, 97(7):077003, 2006.

[21] A. Sanna, G. Profeta, A. Floris, A. Marini, E.K.U. Gross, and S. Massidda. Anisotropic gap of superconducting CaC_6 : A first-principles density functional calculation. *Phys. Rev. B*, 75(2):020511, 2007.

[22] J.S. Kim, L. Boeri, J.R. O'Brien, F.S. Razavi, and R.K. Kremer. Superconductivity in heavy alkaline-earth intercalated graphites. *Phys. Rev. Lett.*, 99(2):027001, 2007.

[23] S. Heguri and M. Kobayashi. Synthesis and physical properties of alkaline earth metal graphite compounds. *Journal of Physics and Chemistry of Solids*, 71(4):572 – 574, 2010.

[24] S. Nakamae, A. Gauzzi, F. Ladieu, D. L'Hôte, N. Eméry, C. Hérold, J.F. Marêché, P. Lagrange, and G. Loupias. Absence of superconductivity down to 80 mK in graphite intercalated BaC_6. *Solid State Communications*, 145(9-10):493 – 496, 2008.

[25] K.C. Rahnejat, C.A. Howard, N.E. Shuttleworth, S.R. Schofield, K. Iwaya, C.F Hirijibehedin, Ch. Renner, G. Aeppli, and M. Ellerby. Charge density waves on the graphene sheets of the superconductor CaC_6.

[26] S. Mrozowski. Specific heat anomalies and spin-spin interactions in carbons: A review. *Journal of Low Temperature Physics*, 35:231–298, 1979.

[27] W. Schnelle, J. Engelhardt, and E. Gmelin. Specific heat capacity of apiezon n high vacuum grease and of duran borosilicate glass. *Cryogenics*, 39(3):271 – 275, 1999.

[28] B. Mühlschlegel. Die thermodynamischen funktionen des supraleiters. *Zeitschrift für Physik A Hadrons and Nuclei*, 155:313–327, 1959.

[29] J.R. Clem. Effects of energy gap anisotropy in pure superconductors. *Annals of Physics*, 40(2):268 – 295, 1966.

[30] Y. Hishiyama and Y. Kaburagi. Electrical resistivity of highly crystallized kish graphite. *Carbon*, 30(3):483 – 486, 1992.

[31] Y. Kaburagi and Y. Hishiyama. Electronic properties of kish graphite crystals with low values of residual resistivity ratio. *Carbon*, 36(11):1671 – 1676, 1998.

[32] W. Primak and L.H. Fuchs. Electrical conductivities of natural graphite crystals. *Phys. Rev.*, 95(1):22–30, 1954.

[33] H. Kempa, P. Esquinazi, and Y. Kopelevich. Field-induced metal-insulator transition in the c-axis resistivity of graphite. *Phys. Rev. B*, 65(24):241101, 2002.

[34] K. Matsubara, K. Sugihara, and T. Tsuzuku. Electrical resistance in the c direction of graphite. *Phys. Rev. B*, 41(2):969–974, 1990.

[35] T. Tsuzuku. Anisotropic electrical conduction in relation to the stacking disorder in graphite. *Carbon*, 17(3):293 – 299, 1979.

[36] D.Z Tsang and M.S Dresselhaus. The c-axis electrical conductivity of kish graphite. *Carbon*, 14(1):43 – 46, 1976.

[37] S.-J. Kim, Yu. I. Latyshev, and T. Yamashita. Submicron stacked-junction fabrication from $Bi_2Sr_2CaCu_2O_{8+\delta}$ whiskers by focused-ion-beam etching. *Applied Physics Letters*, 74(8):1156–1158, 1999.

[38] Yu.I. Latyshev, P. Monceau, S.A. Brazovski, A.P. Orlov, A.A. Sinchenko, Th. Fournier, and E. Mossang. Interlayer tunneling spectroscopy of layered CDW materials. *J. Phys. IV France*, 131:197–202, 2005.

[39] Yu.I. Latyshev, Z.Y.A. Kosakovskaya, A.P. Orlov, A.Yu. Latyshev, V.V. Kolesov, P. Monceau, and D. Vignolles. Nonlinear interlayer transport in the aligned carbon nanotube films and graphite. *Journal of Physics: Conference Series*, 129(1):012032, 2008.

[40] S. Ono. C-Axis Resistivity of Graphite in Connection with Stacking Faults. *Journal of the Physical Society of Japan*, 40(2):498–504, 1976.

[41] V. Gunasekaran and S.J. Kim. Investigation of electrical transport characteristics of nanoscale stacks fabricated on thin graphite layer. *Thin Solid Films*, In Press, Corrected Proof, 2011.

[42] P. Esquinazi, A. Setzer, R. Höhne, C. Semmelhack, Y. Kopelevich, D. Spemann, T. Butz, B. Kohlstrunk, and M. Lösche. Ferromagnetism in oriented graphite samples. , 66(2):024429–+, July 2002.

[43] S. Doyen-Lang, A. Charlier, L. Lang, M.F. Charlier, and E. McRae. Theoretical study of charge transfer in graphite intercalation compounds. *Synthetic Metals*, 58(1):95 – 107, 1993.

[44] N. Emery, C. Hérold, M. d'Astuto, V. Garcia, Ch. Bellin, J. F. Marêché, P. Lagrange, and G. Loupias. Superconductivity of Bulk CaC_6. *Phys. Rev. Lett.*, 95(8):087003, 2005.

[45] C. Wang, B. Giambattista, C.G. Slough, R.V. Coleman, and M.A. Subramanian. Energy gaps measured by scanning tunneling microscopy. *Phys. Rev. B*, 42(14):8890–8906, 1990.

[46] A. Yoshida and Y. Hishiyama. Electron channeling effect on highly oriented graphites–Size evaluation and oriented mapping of crystals. *Journal of Materials Research*, 7:1400–1405, 1992.

[47] K.S. Krishnan and N. Ganguli. Large Anisotropy of the Electrical Conductivity of Graphite. , 144:667–+, 1939.

[48] T. Enoki, M. Endo, and M. Suzuki. *Graphite Intercalation Compounds and Applications*. Oxford Univ. Press, USA, 2003.

[49] N. García, P. Esquinazi, J. Barzola-Quiquia, B. Ming, and D. Spoddig. Transition from Ohmic to ballistic transport in oriented graphite: Measurements and numerical simulations. , 78(3):035413–+, 2008.

[50] P. Schaffäutl. *J. prakt. Chem.*, 21:155, 1841.

[51] N.B. Hannay, T.H. Geballe, B.T. Matthias, K. Andres, P. Schmidt, and D. MacNair. Superconductivity in graphitic compounds. *Phys. Rev. Lett.*, 14(7):225–226, 1965.

[52] T.E. Weller, M. Ellerby, S.S. Saxena, R.P. Smith, and N.T. Skipper. Superconductivity in the Intercalated Graphite Compounds C_6Yb and C_6Ca. *Nature Physics*, 1(1):39–41, 2005.

[53] G. Csanyi, P.R. Littlewood, A.H. Nevidomskyy, C.J. Pickard, and B.D. Simons. Superconductivity in the Intercalated Graphite Compounds C_6Yb and C_6Ca. *Nature Physics*, 1(1):42–45, 2005.

[54] J.C. González, M. Muñoz, N. García, J. Barzola-Quiquia, D. Spoddig, K. Schindler, and P. Esquinazi. Sample-size effects in the magnetoresistance of graphite. *Phys. Rev. Lett.*, 99(21):216601, 2007.

[55] S. Dusari, J. Barzola-Quiquia, P. Esquinazi, and N. García. Ballistic transport at room temperature in micrometer-size graphite flakes. *Phys. Rev. B*, 83(12):125402, 2011.

[56] J.-C. Charlier, X. Gonze, and J.-P. Michenaud. Graphite Interplanar Bonding: Electronic Delocalization and van der Waals Interaction. *Europhysics Letters*, 28(6):403, 1994.

[57] C.S.G. Cousins and M.I. Heggie. Elasticity of carbon allotropes. III. Hexagonal graphite: Review of data, previous calculations, and a fit to a modified anharmonic Keating model. *Phys. Rev. B*, 67(2):024109, 2003.

[58] S. Liu and C.R. Loper Jr. The formation of kish graphite. *Carbon*, 29(4-5):547 – 555, 1991.

[59] A.R. Ubbelhode and F.A. Lewis. *Graphite and its Compounds*. Oxford Univ. Press, 1960.

[60] S. Liu and C.R. Loper Jr. Kish, a source of crystalline graphite. *Carbon*, 29(8):1119 – 1124, 1991.

[61] Y. Kaburagi and Y. Hishiyama. A scaling approach to the transverse magnetoresistance of kish graphite at 77 k. *Carbon*, 35(8):1151 – 1156, 1997.

[62] J.C. Slonczewski and P.R. Weiss. Band structure of graphite. *Phys. Rev.*, 109(2):272–279, 1958.

[63] J.W. McClure. Band Structure of Graphite and de Haas-van Alphen Effect. *Phys. Rev.*, 108(3):612–618, 1957.

[64] L. Pietronero and S. Strässler. Bond-length change as a tool to determine charge transfer and electron-phonon coupling in graphite intercalation compounds. *Phys. Rev. Lett.*, 47(8):593–596, 1981.

[65] M.P.M. Dean, A.C. Walters, C.A. Howard, T.E. Weller, M. Calandra, F. Mauri, M. Ellerby, S.S. Saxena, A. Ivanov, and D.F. McMorrow. Neutron scattering study of the high-energy graphitic phonons in superconducting CaC_6. $Phys. Rev. B, 82(1) : 014533, 2010.$

[66] M.H. Upton, A.C. Walters, C.A. Howard, K.C. Rahnejat, M. Ellerby, J.P. Hill, D.F. McMorrow, A. Alatas, B.M. Leu, and W. Ku. Phonons in superconducting CaC_6 studied via inelastic x-ray scattering. *Phys. Rev. B*, 76(22):220501, 2007.

[67] M. d´Astuto and M. Krisch. High resolution inelastic x-ray scattering from thermal collective excitations. *JDN*, 10:487–503, 2010.

[68] M.P.M. Dean, C.A. Howard, S.S. Saxena, and M. Ellerby. Nonadiabatic phonons within the doped graphene layers of XC_6 compounds. *Phys. Rev. B*, 81(4):045405, 2010.

[69] J. Hlinka, I. Gregora, J. Pokorny, C. Hérold, N. Emery, J.F. Marêché, and P. Lagrange. Lattice dynamics of CaC_6 by Raman spectroscopy. *Phys. Rev. B*, 76(14):144512, 2007.

[70] A. Mialitsin, J.S. Kim, R.K. Kremer, and G. Blumberg. Raman scattering from the CaC_6 superconductor in the presence of disorder. *Phys. Rev. B*, 79(6):064503, 2009.

[71] N.A.W. Holzwarth, S. Rabii, and L.A. Girifalco. Theoretical study of lithium graphite. I. Band structure, density of states, and Fermi-surface properties. *Phys. Rev. B*, 18(10):5190–5205, 1978.

[72] M. Posternak, A. Baldereschi, A. J. Freeman, E. Wimmer, and M. Weinert. Prediction of electronic interlayer states in graphite and reinterpretation of alkali bands in graphite intercalation compounds. *Phys. Rev. Lett.*, 50(10):761–764, 1983.

[73] E.S.R. Gopal. *Specific Heats at Low Temperatures*. Heywood Books, 1966.

[74] P. Debye. Zur Theorie der spezifischen Wärmen. *Annalen der Physik*, 344:789–839, 1912.

[75] A. Sommerfeld. Zur Elektronentheorie der Metalle auf Grund der Fermischen Statistik. *Zeitschrift fur Physik*, 47:43–60, 1928.

[76] A.T. Petit and P.L. Dulong. Recherches sur quelques points importans de la theorie de la chaleur. *Ann. Chim. Phys*, 10:395, 1819.

[77] H. Kamerlingh-Onnes. The superconductivity of mercury. *Commun. Phys. Lab. Univ. Leiden*, 12:120, 1911.

[78] W. Meissner and R. Ochsenfeld. Ein neuer effekt bei eintritt der supraleitfähigkeit. *Naturwissenschaften*, 21:787–788, 1933.

[79] F. London and H. London. The electromagnetic equations of the supraconductor. *Proc. Roy. Soc. A*, 149(866):71–88, 1935.

[80] A.A. Abrikosov. Magnetic properties of superconductors of the second group. *Sov. Phys. - JETP*, 5(6):1174–1182, 1957.

[81] N.R. Werthamer, E. Helfand, and P.C. Hohenberg. Temperature and Purity Dependence of the Superconducting Critical Field, H_{c2}. III. Electron Spin and Spin-Orbit Effects. *Phys. Rev.*, 147(1):295–302, 1966.

[82] J.A. Woollam, R.B. Somoano, and P. O'Connor. Positive Curvature of the H_{c2}-versus-Tc Boundaries in Layered Superconductors. *Phys. Rev. Lett.*, 32(13):712–714, 1974.

[83] J. Bardeen, L.N. Cooper, and J.R. Schrieffer. Microscopic theory of superconductivity. *Phys. Rev.*, 106(1):162–164, 1957.

[84] J.G. Bednorz and K.A. Müller. Possible high Tc superconductivity in the Ba-La-Cu-O system. *Zeitschrift für Physik B Condensed Matter*, 64:189–193, 1986.

[85] G. Grüner. *Density Waves in Solids*. Addison-Wesley, Reading, 1994.

[86] H. Frolich. On the theory of superconductivity: The one-dimensional case. *Proc. Roy. Soc. A*, 223:296–305, 1954.

[87] R.R. Peierls. *Quantum Theory of Solids*. Oxford Univ. Press, 1955.

[88] A.W. Overhauser. Spin density waves in an electron gas. *Phys. Rev.*, 128(3):1437–1452, 1962.

[89] J.A. Wilson, F.J. di Salvo, and S. Mahajan. Charge-density waves and superlattices in the metallic layered transition metal dichalcogenides. *Advances in Physics*, 24:117–201, 1975.

[90] W. Fogle and J.H. Perlstein. Semiconductor-to-metal transition in the blue potassium molybdenum bronze, $k_{0.30}$ moo_3; example of a possible excitonic insulator. *Phys. Rev. B*, 6(4):1402–1412, Aug 1972.

[91] R.L. Withers and J.A. Wilson. An examination of the formation and characteristics of charge-density waves in inorganic materials with special reference to the two- and one-dimensional transition-metal chalcogenides. *Journal of Physics C: Solid State Physics*, 19(25):4809, 1986.

[92] D.E. Moncton, J.D. Axe, and F.J. DiSalvo. Study of Superlattice Formation in 2H-$NbSe_2$ and 2H-$TaSe_2$ by Neutron Scattering. *Phys. Rev. Lett.*, 34(12):734–737, 1975.

[93] C.G. Kuper. On the Thermal Properties of Frohlich's One-Dimensional Superconductor. *Proc. Roy. Soc. A*, 227:214–228, 1955.

[94] J. Solyom. The fermi gas model of one-dimensional conductors. *Advances in Physics*, 28:201–303, 1979.

[95] P.A. Lee, T.M. Rice, and P.W. Anderson. Fluctuation effects at a peierls transition. *Phys. Rev. Lett.*, 31(7):462–465, 1973.

[96] J. Laverock, S.B. Dugdale, Zs. Major, M.A. Alam, N. Ru, I.R. Fisher, G. Santi, and E. Bruno. Fermi surface nesting and charge-density wave formation in rare-earth tritellurides. *Phys. Rev. B*, 71(8):085114, 2005.

[97] W. Dieterich and P. Fulde. Magnetic field dependence of the Peierls instability in one-dimensional conductors. *Zeitschrift fur Physik*, 265:239–243, 1973.

[98] D. Graf, J.S. Brooks, E.S. Choi, S. Uji, J.C. Dias, M. Almeida, and M. Matos. Suppression of a charge-density-wave ground state in high magnetic fields: Spin and orbital mechanisms. *Phys. Rev. B*, 69(12):125113, 2004.

[99] V. Gama, R.T. Henriques, G. Bonfait, M. Almeida, S. Ravy, J.P. Pouget, and L. Alcácer. The Interplay Between Conduction Electrons and Chains of Localised Spins in The Molecular Metals $(Per)_2M(mnt)_2$, M=Au, Pt, Pd, Ni, Cu, Co and Fe. *Molecular Crystals and Liquid Crystals Science and Technology. Section A. Molecular Crystals and Liquid Crystals*, 234(1):171–178, 1993.

[100] G. Grüner and A. Zettl. Charge density wave conduction: A novel collective transport phenomenon in solids. *Physics Reports*, 119:117–232, 1985.

[101] A.M. Gabovich, A.I. Voitenko, and M. Ausloos. Charge- and spin-density waves in existing superconductors: competition between cooper pairing and peierls or excitonic instabilities. *Physics Reports*, 367(6):583 – 709, 2002.

[102] A.M. Gabovich, M.S. Li, H. Szymczak, and A.I. Voitenko. Thermodynamics of superconductors with charge-density waves. *Journal of Physics: Condensed Matter*, 15(17):2745, 2003.

[103] S.V. Borisenko, A.A. Kordyuk, V.B. Zabolotnyy, D.S. Inosov, D. Evtushinsky, B. Büchner, A.N. Yaresko, A. Varykhalov, R. Follath, W. Eberhardt, L. Patthey, and H. Berger. Two Energy Gaps and Fermi-Surface "Arcs" in $NbSe_2$. *Phys. Rev. Lett.*, 102(16):166402, 2009.

[104] K. Tanaka, W.S. Lee, D.H. Lu, A. Fujimori, T. Fujii, Risdiana, I. Terasaki, D.J. Scalapino, T.P. Devereaux, Z. Hussain, and Z.-X. Shen. Distinct Fermi-Momentum-Dependent Energy Gaps in Deeply Underdoped Bi2212. *Science*, 314(5807):1910–1913, 2006.

[105] A.A. Kordyuk, S.V. Borisenko, V.B. Zabolotnyy, R. Schuster, D.S. Inosov, D.V. Evtushinsky, A.I. Plyushchay, R. Follath, A. Varykhalov, L. Patthey, and H. Berger. Nonmonotonic pseudogap in high-Tc cuprates. *Phys. Rev. B*, 79(2):020504, 2009.

[106] E. Morosan, H.W. Zandbergen, B.S. Dennis, J.W.G. Bos, Y. Onose, T. Klimczuk, A.P. Ramirez, N.P. Ong, and R.J. Cava. Superconductivity in Cu_xTiSe_2. *Nature Physics*, 2:544–550, 2006.

[107] D. Graf, J.S. Brooks, M. Almeida, J.C. Dias, S. Uji, T. Terashima, and M. Kimata. Evolution of superconductivity from a charge-density-wave ground state in pressurized $(Per)_2[Au(mnt)_2]$. *Europhysics Letters*, 85:27009, 2009.

[108] M. Kobayashi, T. Enoki, H. Inokuchi, M. Sano, A. Sumiyama, Y. Oda, and H. Nagano. Superconductivity in the first stage rubidium graphite intercalation compound C_8Rb. *Synthetic Metals*, 12(1-2):341 – 346, 1985.

[109] Y. Koike, S. Tanuma, H. Suematsu, and K. Higuchi. Superconductivity in the graphite-potassium intercalation compound C_8K. *Journal of Physics and Chemistry of Solids*, 41(10):1111 – 1118, 1980.

[110] V.V. Avdeev, O.V. Zharikov, V.A. Nalimova, A.V. Pal'Nichenko, and K.N. Semenenko. Superconductivity of layered compounds C_6K and C_4K. *Sov. Phys. - JETP*, 43:484, 1986.

[111] I.T. Belash, A.D. Bronnikov, O.V. Zharikov, and A.V. Pal'nichenko. Superconductivity of graphite intercalation compound with lithium C_2Li. *Solid State Communications*, 69(9):921 – 923, 1989.

[112] I.T. Belash, A.D. Bronnikov, O.V. Zharikov, and A.V. Palnichenko. On the superconductivity of graphite intercalation compounds with sodium. *Solid State Communications*, 64(12):1445 – 1447, 1987.

[113] V.V. Avdeev, V.A. Nalimova, and K.N. Semenenko. The alkali metals in graphite matrixes-new aspects of metallic state chemistry. *High Pressure Research*, 6:11–25, 1990.

[114] I.I. Mazin. Intercalant-Driven Superconductivity in YbC_6 and CaC_6. *Phys. Rev. Lett.*, 95(22):227001, 2005.

[115] J.S. Kim, L. Boeri, R.K. Kremer, and F.S. Razavi. Effect of pressure on superconducting Ca-intercalated graphite CaC_6 . *Phys. Rev. B*, 74(21):214513, 2006.

[116] D.G. Hinks, D. Rosenmann, H. Claus, M.S. Bailey, and J.D. Jorgensen. Large Ca isotope effect in the CaC_6 superconductor. *Phys. Rev. B*, 75(1):014509, 2007.

[117] V.Z. Kresin. *Pair Correlations in Many-Fermion Systems*. Springer, New York, 1998.

[118] C. Kurter, L. Ozyuzer, D. Mazur, J.F. Zasadzinski, D. Rosenmann, H. Claus, D.G. Hinks, and K.E. Gray. Large energy gaps in CaC_6 from tunneling spectroscopy: Possible evidence of strong-coupling superconductivity. *Phys. Rev. B*, 76(22):220502, 2007.

[119] Sobota J.A. Howard C.A. Pickard C.J. Hashimoto M. Lu D.H. Mo S.K. Kirchmann P.S. Yang, S.L. and Shen Z.H. Superconducting graphene sheets in cac6 enabled by phonon-mediated interband interactions. *Nature Comms*, 5, 2014.

[120] T. Valla, J. Camacho, Z.-H. Pan, A.V. Fedorov, A.C. Walters, C.A. Howard, and M. Ellerby. Anisotropic Electron-Phonon Coupling and Dynamical Nesting on the Graphene Sheets in Superconducting CaC_6 using Angle-Resolved Photoemission Spectroscopy. *Phys. Rev. Lett.*, 102(10):107007, 2009.

[121] R.P. Smith, T.E. Weller, A.F. Kusmartseva, N.T. Skipper, M. Ellerby, and S.S. Saxena. Positive pressure dependence of the superconducting transition temperature in C_6Yb. *Physica B: Condensed Matter*, 378-380:892 – 893, 2006.

[122] A.H. Castro-Neto. Charge Density Wave, Superconductivity, and Anomalous Metallic Behavior in 2D Transition Metal Dichalcogenides. *Phys. Rev. Lett.*, 86(19):4382–4385, 2001.

[123] B. Sipos, A.F. Kusmartseva, A. Akrap, H. Berger, L. Forro, and E. Tutis. From Mott State to Superconductivity in 1T-TaS_2. *Nature Materials*, 7:960–965, 2008.

[124] J. Singleton. Quasi-two-dimensional organic superconductors: A review. *Comtemporary Physics*, 43(2):63–96, 2002.

[125] C. Howald, H. Eisaki, N. Kaneko, M. Greven, and A. Kapitulnik. Periodic density-of-states modulations in superconducting $Bi_2Sr_2CaCu_2O_{8+\delta}$. *Phys. Rev. B*, 67(1):014533, 2003.

[126] J.S. Hwang, K.J. Lin, and C. Tien. Measurement of heat capacity by fitting the whole temperature response of a heat-pulse calorimeter. *Review of Scientific Instruments*, 68(1):94–101, 1997.

[127] M. Suganuma, T. Kondow, and U. Mizutani. Low-temperature specific heats of rubidium-graphite intercalation compounds. *Phys. Rev. B*, 23(2):706–711, 1981.

[128] U. Mizutani, T. Kondow, and T.B. Massalski. Low-temperature specific heats of graphite intercalation compounds with potassium and cesium. *Phys. Rev. B*, 17(8):3165–3173, 1978.

[129] B.J.C. van der Hoeven and P.H. Keesom. Specific Heat of Various Graphites between 0.4 and 2.0K. *Phys. Rev.*, 130(4):1318–1321, 1963.

[130] M. Grayson-Alexander, D.P. Goshorn, and D.G. Onn. Low-temperature specific heat of the graphite intercalation compounds KC_8, CsC_8, RbC_8, and their parent highly oriented pyrolytic graphite. *Phys. Rev. B*, 22(10):4535–4542, 1980.

[131] P. Delhaes, J.C. Rouillon, J.P. Manceau, D. Guerard, and A. Herold. Paramagnetism and specific heat of the graphite lamellar compound C_6Li. *J. Physique Lett.*, 37(5):127–129, 1976.

[132] C. Ayache, E. Bonjour, R. Lagnier, and J.E. Fischer. Specific heat of LiC_6 from 4-300 K. *Physica B+C*, 99(1-4):547 – 550, 1980.

[133] E. Revolinsky, G.A. Spiering, and D.J. Beerntsen. Superconductivity in the niobium-selenium system. *Journal of Physics and Chemistry of Solids*, 26(6):1029 – 1034, 1965.

[134] P. Trey, S. Gygax, and J.-P. Jan. Anisotropy of the Ginzburg-Landau parameter in $NbSe_2$. *Journal of Low Temperature Physics*, 11:421–434, 1973. 10.1007/BF00656561.

[135] B.P. Clayman and R.F. Frindt. The superconducting energy gap of $NbSe_2$. *Solid State Communications*, 9(22):1881–1884, 1971.

[136] H.F. Hess, R.B. Robinson, R.C. Dynes, J.M. Valles, and J.V. Waszczak. Scanning-Tunneling-Microscope Observation of the Abrikosov Flux Lattice and the Density of States near and inside a Fluxoid. *Phys. Rev. Lett.*, 62(2):214–216, 1989.

[137] Y. Moriya, H. Kawaji, T. Atake, M. Fukuhara, H. Kimura, and A. Inoue. Heat capacity measurements on a thin ribbon sample of $Zr_{0.55}Al_{0.10}Ni_{0.05}Cu_{0.30}$ glassy alloy and Apiezon N high vacuum grease using a Quantum Design Physical Property Measurement System. *Cryogenics*, 49(5):185 – 191, 2009.

[138] J.G. Bunting, T. Ashworth, and H. Steeple. The Specific Heat of Apiezon N Grease. *Cryogenics*, 9(5):385–386, 1969.

[139] N. Ru, C.L. Condron, G.Y. Margulis, K.Y. Shin, J. Laverock, S.B. Dugdale, M.F. Toney, and I.R. Fisher. Effect of chemical pressure on the charge density wave transition in rare-earth tritellurides RTe_3 . *Phys. Rev. B*, 77(3):035114, 2008.

[140] Y. Wang, M. Chung, T.N. O'Neal, and J.W. Brill. Differential scanning calorimetry at charge-density-wave transitions. *Synthetic Metals*, 46(3):307 – 316, 1992.

[141] A. Gauzzi, S. Takashima, N. Takeshita, C. Terakura, H. Takagi, N. Emery, C. Hérold, P. Lagrange, and G. Loupias. Enhancement of Superconductivity and Evidence of Structural Instability in Intercalated Graphite CaC_6 under High Pressure. *Phys. Rev. Lett.*, 98(6):067002, 2007.

[142] S. Foner and E.J. McNiff Jr. Upper critical fields of layered superconducting $NbSe_2$ at low temperature. *Physics Letters A*, 45(6):429 – 430, 1973.

[143] K.-H. Müller and G. Fuchs and A. Handstein and K. Nenkov and V.N. Narozhnyi and D. Eckert. The upper critical field in superconducting MgB_2. *Journal of Alloys and Compounds*, 322(1-2):L10 – L13, 2001.

[144] G.F. Chen, Z. Li, G. Li, J. Zhou, D. Wu, J. Dong, W.Z. Hu, P. Zheng, Z.J. Chen, H.Q. Yuan, J. Singleton, J.L. Luo, and N.L. Wang. Superconducting Properties of the Fe-Based Layered Superconductor $LaFeAsO_{0.9}F_{0.1-\delta}$. *Phys. Rev. Lett.*, 101(5):057007, 2008.

[145] N. Nakai, P. Miranović, M. Ichioka, and K. Machida. Field dependence of the zero-energy density of states around vortices in an anisotropic-gap superconductor. *Phys. Rev. B*, 70(10):100503, 2004.

[146] N.W. Ashcroft and Mermin D.N. *Solid State Physics*. Saunders College, Philadelphia, 1976.

[147] J.C. Maxwell. *A treatise on electricity and magnetism*. Dover Press, New York, 1891.

[148] G. Wexler. The size effect and the non-local boltzmann transport equation in orifice and disk geometry. *Proceedings of the Physical Society*, 89(4):927, 1966.

[149] W.A. Little. The transport of heat between dissimilar solids at low temperatures. *Canadian Journal of Physics*, 37:334–+, 1959.

[150] Y.V. Sharvin. *Sov. Phys. - JETP*, 48:984, 1965.

[151] A.L. Efros and B.I. Shklovskii. Coulomb gap and low temperature conductivity of disordered systems. *Journal of Physics C: Solid State Physics*, 8(4):L49, 1975.

[152] R. Rosenbaum, N.V. Lien, M.R. Graham, and M. Witcomb. A useful Mott - Efros - Shklovskii resistivity crossover formulation for three-dimensional films. *Journal of Physics: Condensed Matter*, 9(29):6247, 1997.

[153] Yu.I. Latyshev, P. Monceau, A.A. Sinchenko, L.N. Bulaevskii, S.A. Brazovskii, T. Kawae, and T. Yamashita. Interlayer tunnelling spectroscopy of the charge density wave state in $NbSe_3$. *Journal of Physics A*, 36(35):9323, 2003.

[154] Yu.I. Latyshev, P. Monceau, S.A. Brazovskii, A.P. Orlov, T. Yamashita, and L.N. Bulaevskii. Method of interlayer tunneling for studies of layered high temperature superconductors and charge density wave materials. *physica status solidi (c)*, 3(9):3110–3113, 2006.

[155] S. Rubanov and P.R. Munroe. Fib-induced damage in silicon. *Journal of Microscopy*, 214(3):213–221, 2004.

[156] J.A. Wilson, F.J. Di Salvo, and S. Mahajan. Charge-density waves in metallic, layered, transition-metal dichalcogenides. *Phys. Rev. Lett.*, 32(16):882–885, 1974.

[157] I.K. Yanson, I.O. Kulik, and A.G. Batrak. Point-contact spectroscopy of electron-phonon interaction in normal-metal single crystals. *Journal of Low Temperature Physics*, 42:527–556, 1981.

[158] C.W.J. Beenakker. Theory of coulomb-blockade oscillations in the conductance of a quantum dot. *Phys. Rev. B*, 44(4):1646–1656, 1991.

[159] H. Xu. Ballistic transport in quantum channels modulated with double-bend structures. , 47:9537–9544, 1993.